Ph.D. Thesis

New detector system for the precise neutron lifetime measurement using pulsed cold neutron beams

Hidetoshi Otono

Department of Physics, Graduate School of Science,

The University of Tokyo

December 2011

Abstract

The values of the neutron lifetime τ_n and the baryon density of the universe η are key parameters for Big Bang nucleosynthesis. Recently, the measurement of the cosmic microwave background radiation at the Wilkinson Microwave Anisotropy Probe has become increasingly sensitive to η, which motivates a neutron lifetime measurement with improved accuracy.

Since the first observation of the neutron decay in 1948, various methods for the measurement of the neutron lifetime using nuclear reactors have been developed, resulting in the world average 881.5 ± 1.5 s given by the Particle Data Group. The proposed method in this thesis employs an accelerator for the first time in all neutron lifetime measurements, making use of the world's most intensive pulsed neutron source at the J-PARC accelerator complex in Tokai, Ibaraki, Japan. In this method, pulsed monochromatic bunch passes through a time projection chamber (TPC), which detects the electron from the neutron decay. The neutron flux can also be measured via the $^3\mathrm{He}(\mathrm{n},\mathrm{p})^3\mathrm{H}$ reaction by mixing a small amount of $^3\mathrm{He}$ in the same detector.

A measurement accuracy of a level 0.1% is needed to be competitive with the world average. To achieve this, backgrounds to the neutron decay and the $^3\mathrm{He}(\mathrm{n},\mathrm{p})^3\mathrm{H}$ reaction have to be physically reduced and statistically subtracted. In this work, a low background TPC has been developed, making use of polyether ether ketone (PEEK) as its main component, which contains no radioactive sources; $^6\mathrm{Li}$ plates are installed in the inner wall of the TPC to capture scattered neutrons; the TPC is surrounded by $4\,\pi$ shielding to reduce environmental radiation. Consequently, the achievable signal-to-background ratio is estimated to be 1, corresponding to a statistical uncertainty of 0.8% for 150 days of beam time, assuming the current beam power of 220 kW. In parallel, an analysis algorithm has been developed, which subtracts the remaining backgrounds using a data-driven approach while retaining more than 99.9% detection efficiency for the neutron decay and the $^3\mathrm{He}(\mathrm{n},\mathrm{p})^3\mathrm{H}$ reaction. As a result, all the systematic uncertainties arising from the particle detection are reduced to a level of 0.1%.

Contents

Chapter 1

Introduction

The neutron was discovered by Chadwick in 1932 [1, 2]. It decays into a proton, an electron and an antineutrino with a lifetime of about 15 minutes. The neutron lifetime plays a key role in Big Bang nucleosynthesis (BBN) as described in the Alpher-Bethe-Gamow paper in 1948 [3, 4], since the neutron lifetime has a direct effect on the abundance of the light elements. After the measurement of the baryon density of the universe by the Wilkinson Microwave Anisotropy Probe (WMAP), the abundance of the light elements is uniquely determined, assuming the BBN as described in Section 2.2. However, the measured abundance does not agree with the prediction, which has become a controversy among particle physics, observational astronomy and cosmological theory. Thus the improvement of the accuracy in the neutron lifetime measurement is desired more strongly than ever.

The experiment described in this thesis differs in many important aspects as compared to any other experiment included in the world average of neutron lifetime given by the Particle Data Group [5]. In particular,

- a pulsed neutron beam generated by an accelerator, J-PARC,

- a new scheme of shaping the neutron beam by using a spin flip chopper,

- an innovative time projection chamber,

are employed. This thesis focuses on the development of the TPC and the analysis algorithm.

The first observation of the neutron decay was done by Snell and Miller by the use of a reactor in 1948 [6]. Since then, more than 20 major experiments have been done, using a variety of methods [7]. The currently-conducted experiments can be classified into three types: the "penning trap method", "gravitational trap method" and the "magnetic trap method" as described in Section 2.3 and Table

1.1. The drawback of each method is the difficulty in evaluating a neutron flux, a wall loss, and a depolarization of the neutrons, respectively.

Method	penning trap [8]	gravitational trap [9]	magnetic trap [10]
Source	reactor	reactor	reactor
Neutron energy	cold neutron	ultra cold neutron	ultra cold neutron
Measured target	proton	neutron	neutron
Advantage	low background	small correction	no wall loss
τ_n result [sec]	$886.6 \pm 1.2 \pm 3.2$	$878.5 \pm 0.7 \pm 0.3$	878.2 ± 1.9

Table 1.1: Properties of methods for the various neutron lifetime measurement experiments.

The "beam method" as described in Section 2.4 and Table 1.2 was developed by Kossakowski and his colleagues in 1989 [11], which is the preceding study of the experiment in this thesis. Kossakowski *et al.* used a continuous cold neutrons at a reactor in Institut Laue-Langevin (ILL), with an energy range of about 1 meV $\sim$ 20 meV. A chopper shapes the beam into short bunches, which pass though a time projection chamber (TPC). In the TPC, the electron from the neutron decay is detected, while the neutron flux can be measured simultaneously in the same detector due to a small amount of mixed ^{3}He which causes ^{3}He(n, p)^{3}H reaction. The length of the bunch is adjusted to be shorter than that of the TPC, so that the fiducial volume of the measurement can be defined accurately when the entire bunch is inside the TPC. Since a detection coverage of 4π srad solid angle for both reactions is guaranteed, it is possible to avoid systematic uncertainties caused by the drawbacks of the currently-conducted experiments.

Method	beam method [11]
Source	reactor
Neutron energy	cold neutron
Measured target	electron
Advantage	flux monitoring, no wall loss, no depolarization
τ_n result [sec]	$878 \pm 27 \pm 14$

Table 1.2: Properties of the beam method for the neutron lifetime measurement experiments.

However the beam method have the following challenges:

1. How to obtain high statistics of pulsed monochromatic neutron,

2. How to reduce and shield the background to the neutron decay,

3. How to extract the neutron decay from the data,

4. How to subtract the background to the neutron decay.

In order to overcome these challenges, new approaches are proposed in this thesis. The comparisons from the experiment by Kossakowski *et al.* are listed.

- Previous work

  1. continuous neutron source + rotating drum + single crystal

  2. radiation shield

  3. use of the track pattern

  4. use of the sideband region outside the fiducial region

- The experiment in this thesis

  1. pulsed neutron source (MLF/J-PARC) + spin flip chopper

  2. TPC made of no radioactive contamination with 4π radiation shields

  3. use of calorimetric information

  4. use of the data-driven approach

The detailed explanation is described in Section 3.1.

The contribution on this work

The author has developed the TPC and invented its analysis algorithm for the measurement of the neutron lifetime. For this purpose, the simulation framework is also established in parallel. The beam line (BL05) at MLF in J-PARC, the spin flip chopper, and the 4π radiation shields are developed mainly by K. Mishima, K. Taketani and H. Oide, respectively.

The organization of the thesis

The first chapter of this thesis is serves as an introduction. In Chapter 2, a theoretical explanation for the neutron decay and the role of the neutron lifetime in the Big Bang nucleosynthesis are described. Methods of past and current experiments are also summarized. Chapter 3 is devoted to an overview of the experimental setup developed in this thesis. Chapter 4 explains simulation framework developed for this experiment. In Chapter 5, the analysis algorithm for the neutron

lifetime is presented. In Chapter 6, features and performances of the TPC are summarized. The discussions on the basis of the results are given in Chapter 7. Finally the thesis is concluded in Chapter 8.

Chapter 2

Neutron decay

2.1 Low energy effective theory of the weak interaction

The neutron lifetime τ_n is expressed as

$$\frac{1}{\tau_n} = \int P(E_e)dE_e, \tag{2.1}$$

where $P(E_e)$ is a rate of emitting the electron with an energy of E_e. According to Fermi's golden rule, $P(E_e)dE_e$ can be expressed by using the transition matrix H_β and the density of available final states dn/dE_0 where E_0 is a total energy of the electron and the antineutrino:

$$P(E_e)dE_e = \frac{2\pi}{\hbar}|H_\beta|^2\frac{dn}{dE_0}. \tag{2.2}$$

Let p_e and p_ν be the momentum of the electron and antineutrino, respectively. Then, the number of the states is described as

$$\frac{dn}{dE_0} = \frac{4\pi p_e^2 dp_e \cdot 4\pi p_\nu^2 dp_\nu}{(2\pi\hbar)^6 dE_0}. \tag{2.3}$$

By using the relativistic relationship between the energy and momentum, p_e and p_ν can be transformed, which gives

$$p_e^2 dp_e = \frac{1}{c^2}p_e E_e dE_e = \frac{1}{c^3}E_e\sqrt{E_e^2 - m_e^2 c^4}dE_e,$$

$$p_\nu^2 dp_\nu = \frac{1}{c^3}E_\nu^2 dE_\nu = \frac{1}{c^3}(E_0 - E_e)^2 dE_e,$$

where the neutrino mass was neglected. Inserting them into Eq. (2.3), the equation is rewritten as

$$\frac{dn}{dE_0} = (4\pi)^2\frac{E_e\sqrt{E_e^2 - m_e^2 c^4}(E_0 - E_e)^2}{(2\pi\hbar c)^6}dE_e. \tag{2.4}$$

The transition matrix of weak interaction $|H_\beta|^2$ has two components: Fermi transition which carries zero angular momentum $|H_F|^2$ and Gamow-Teller transition which carries one unit of angular momentum $|H_{GT}|^2$. In the case of free neutron decay, each transition matrix is calculated [12] as

$$
\begin{aligned}
|H_F|^2 &= 1, \\
|H_{GT}|^2 &= 3.
\end{aligned}
$$

By using strengths of each transition, C_V and C_A, $|H_\beta|^2 = C_V + 3C_A$ can be obtained, which introduces

$$
\frac{1}{\tau_n} = \int (C_V + 3C_A) \frac{E_e \sqrt{E_e^2 - m_e^2 c^4}(E_0 - E_e)^2}{2\pi^3 \hbar^7 c^6} dE_e. \tag{2.5}
$$

2.2 Big Bang nucleosynthesis

Big Bang nucleosynthesis (BBN) applies the results from nuclear physics to the early universe under high temperature and pressure, with the free parameters being only the baryon-to-photon ratio of the universe η. The predicted abundance of light elements is in good agreement with the observation of primordial population [3, 4], which is one of the evidence for the Big Bang theory.

Immediately after the Big Bang ($t \sim 10^{-4}$ s) the quark-gluon plasma was cooled down to give rise to neutrons and protons. The temperature was high enough for the weak, strong and electromagnetic interactions to remain in equilibrium: $n + e^+ \leftrightarrow p + \bar{\nu}$ and $p + e^- \leftrightarrow n + \nu$. At that time, the ratio of neutrons to protons was given by the Boltzmann factor

$$
n/p = \exp\left(-\Delta/T\right), \tag{2.6}
$$

where T is the temperature of the universe and Δ is the difference between the proton and the neutron mass. At $t \sim 1$ s after the Big Bang, the temperature reached $T \sim 1$ MeV, at which point, the weak interaction fell out of the equilibriums. This is called nucleon freeze-out, during which the neutron lifetime plays a significant role since the strength of the charged weak interaction is proportional to the combination of the coupling constants C_V and C_A that appear in Eq. (2.5).

Subsequently, the neutron lifetime governs the change in the neutron to proton ratio until the universe was cool enough to form stable deuterium. Then all neutrons in the universe were bound into light nuclei by $t = 3$ min.

Since nucleon freeze-out depends also on η, BBN can constrain η by using the primordial element abundances as a function of the neutron lifetime. Recently,

the data on cosmic microwave background (CMB) anisotropies by the WMAP observatory have become increasingly sensitive to η [13]. Thus the comparison of these two independent measurements allow for a more stringent test of BBN.

Figure 2.1 shows the primordial element abundances versus the baryon density [14] which are based upon the world average of neutron. The thickness of the bands represents 1σ uncertainties in the calculated abundance. The ratio of ^{4}He to H is described as Y in the top figure and is expected from BBN to be $Y = 0.2486 \pm 0.0002$. On the other hand, the latest measurement of Y by [15] finds $Y = 0.2565 \pm 0.0010 \pm 0.0050$. This value is more than 1σ away from the value given by BBN, which is determined by the neutron lifetime.

If this deviation is real, then it may provide insight into new physics beyond the minimal BBN model [16], for example, inhomogeneous big bang nucleosynthesis, which motivates a neutron lifetime measurement with improved accuracy.
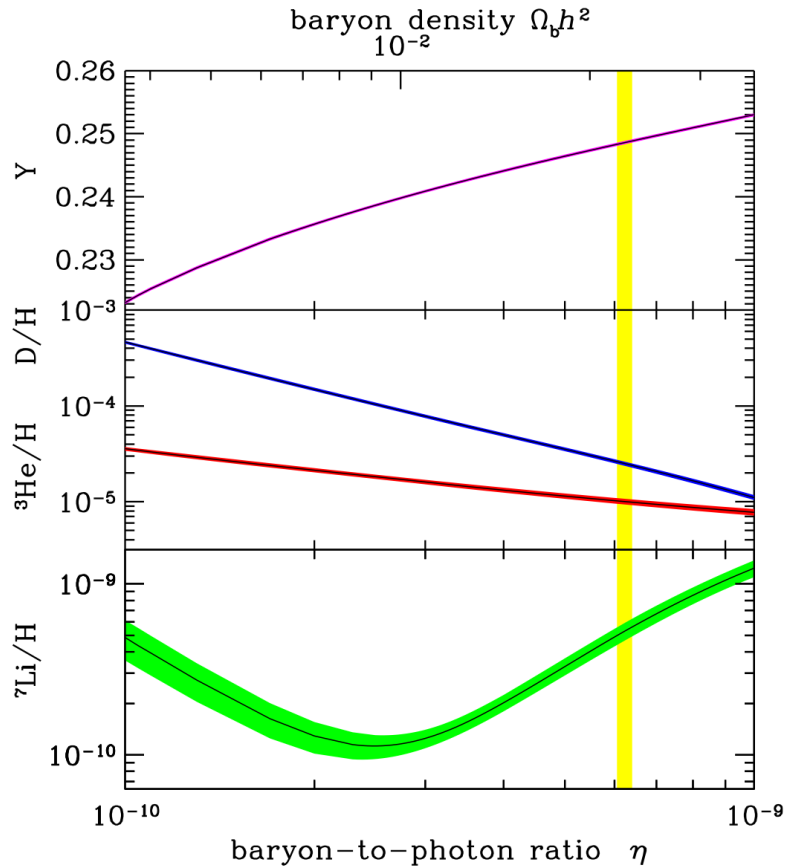
Figure 2.1: The primordial element abundances versus the baryon density based on Big Bang nucleosynthesis [14].

2.3 Experiments of the neutron lifetime

After the discovery of the neutron in 1932 [1, 2], Chadwick and Goldhaber began measuring the mass of the neutron and confirmed that it exceeds the mass of the proton in 1935 [17, 18]. Thus they predicted a possible decay of the neutron into a proton, an electron and an antineutrino. However, it took more than 10 years to detect the decay since the neutron flux from radioisotopes was not sufficiently high. The development of the nuclear reactor provided the prospect of significantly higher neutron flux.

2.3.1 Methods for the measurement of the neutron lifetime

Neutrons are classified according to its energy and the featured categories in this thesis are the following:

- fast neutron
  Fission neutrons from a reactor and spallation neutrons by an accelerator belong to fast neutrons, whose energy is around 1 MeV.

- cold neutron
  The neutrons decelerated by a moderator to a temperature of a several tens of degrees Kelvin belong to cold neutrons, whose energy is around 1 meV. The wave nature of the neutron becomes apparent at this energy scale, which allows for a use of optical devices, such as a spin flip chopper as described in Section 3.3.

- ultra cold neutron
  The neutrons decelerated by a moderator such as superfluid helium by means of phonon scattering belong to ultra cold neutron (UCN), whose energy is less than 220 neV. Since the kinetic energy of UCNs is lower than the Fermi effective potential of the matter, UCNs are reflected off the surface of matter.

The relationship among energy, velocity and wavelength of the neutron is summarized in Figure 2.2. Figure 2.3 and 2.4 show the energy spectra of electrons and protons from the neutron decay. The end points of the energy are 0.754 keV and 782 keV, respectively.

By using the various energy of the neutron and the characteristic spectra of the proton and the electron, various measurements for the neutron lifetime have been done, which are summarized in Table 2.1. The transition of the world average value given by the Particle Data Group is shown in Figure 2.5.
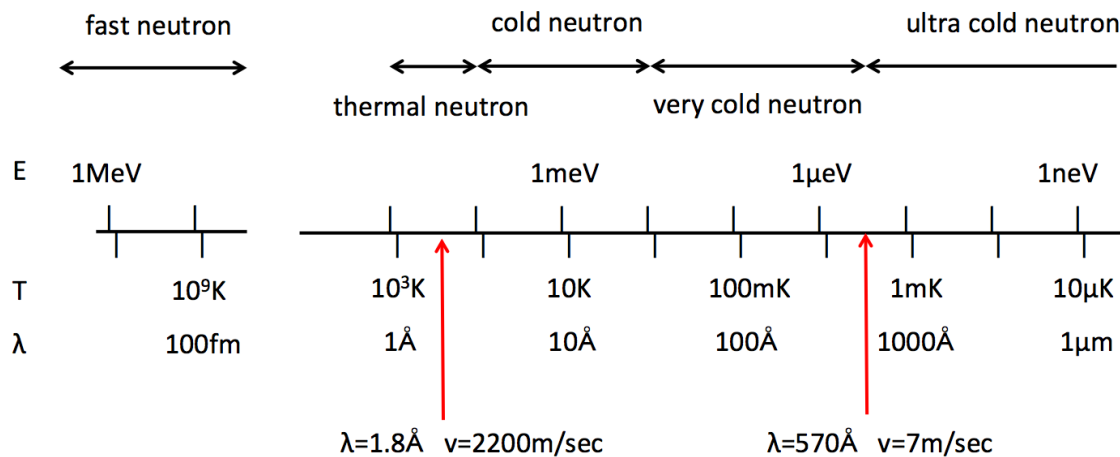
Figure 2.2: Classification of neutrons according to its energy.
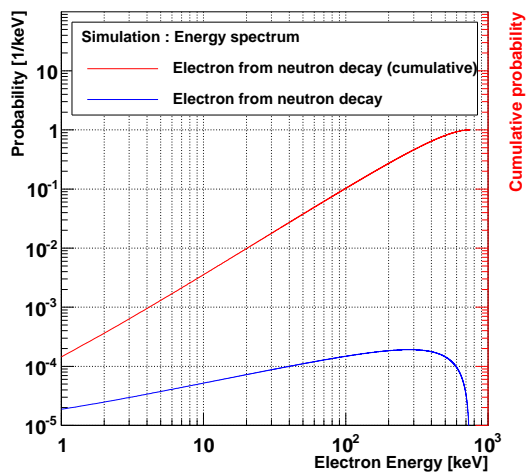
Figure 2.3: A energy spectrum of electrons emitted from the neutron decay.
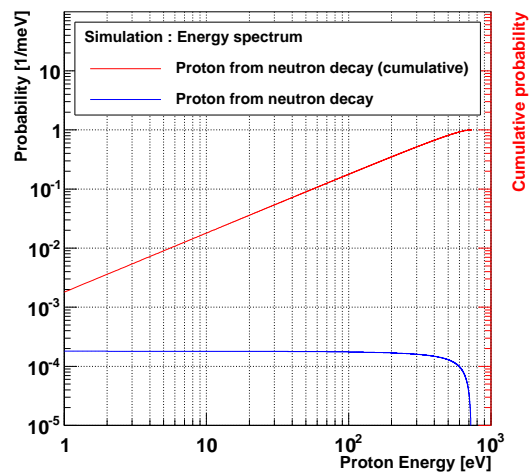
Figure 2.4: A energy spectrum of protons emitted from the neutron decay.

The experiments currently in operation are classified into three methods: "penning trap method", "gravitational trap method" and "magnetic trap method". In the past 20 years the accuracy of the neutron lifetime has improved to 0.1%, resulting in the world average 881.5 ± 1.5 s given by the Particle Data Group [19]. However the included values are not consistent with each other, in particular, the penning trap method by NIST group gives $886.3 \pm 1.2 \pm 3.2$ s [8], while the gravitational method by PNPI group gives $878.5 \pm 0.7 \pm 0.3$ s [9] as shown in Figure 2.6. In the following sections, each method is described.
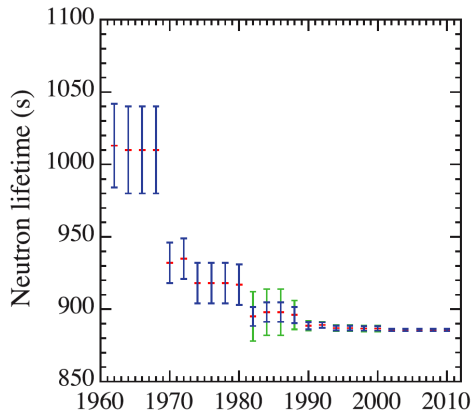
Figure 2.5: History of the neutron lifetime world average given by the Particle Data Group [5].
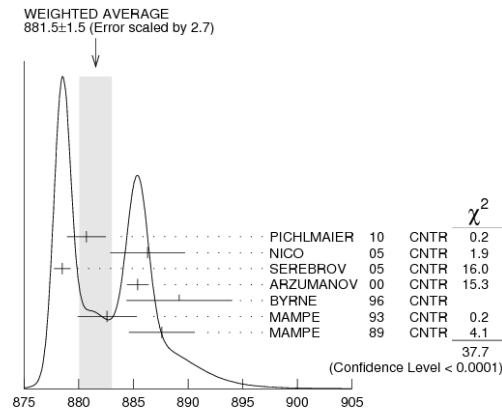
Figure 2.6: Weighted average of the neutron lifetime combined by the Particle Data Group in 2011 [19].

2.3.2   Penning trap method

The most accurate measurement in the penning trap method was obtained by the Sussex-ILL-NIST series of experiments [8, 32] as shown in Figure 2.7. A cold neutron beam passes through a decay volume, so that some neutrons decay and emit the proton, whose maximum energy is 754 eV. Thus the protons are stored in the penning trap with a voltage of 800 V and are led to the detector after turning off the voltage. After the neutron beams exits the trap, it passes through a very thin ^{6}LiF on a silicon substrate, which causes ^{6}Li$(n, \alpha)^3$H reaction. A set of four detectors with well characterized detection solid angle is located beside the silicon substrate. The efficiency for the alpha and triton is also obtained, thus the neutron flux can be measured.

The count rate of the neutron decay S_β is given by

$$S_\beta = \epsilon_p N \frac{L_1}{\tau_n v}, \tag{2.7}$$

τ_n(sec)	Year	Authers	Ref.	Method	Energy
1108 ± 216	1951	J. M. Robson	[20]	beam	CN
1100 ± 165	1959	N. D'Angelo	[21]	beam	CN
1013 ± 26	1959	A. N. Sosnovsky	[22]	beam	CN
919 ± 14	1972	C. J. Cristensen	[23]	beam	CN
875 ± 95	1980	Yu. Yu. Kosvintsev *et al.*	[24]	gravitational trap	UCN
903 ± 13	1986	Yu. Yu. Kosvintsev *et al.*	[25]	gravitational trap	UCN
891 ± 9	1988	P. E. Spivak	[26]	beam	CN
877 ± 10	1989	F. Anton *et al.*	[27]	magnetic trap	VCN
870 ± 8	1989	A. G. Kharitonov *et al.*	[28]	gravitational trap	UCN
$887.6 \pm 3.0^*$	1989	W. Mampe *et al.*	[29]	gravitational trap	UCN
$878 \pm 27 \pm 14$	1989	R. Kossakowski *et al.*	[11]	beam	CN
$888.4 \pm 3.1 \pm 1.1$	1992	V. V. Nesvizhevsky *et al.*	[30]	gravitational trap	UCN
$882.6 \pm 2.7^*$	1993	W. Mampe *et al.*	[31]	gravitational trap	UCN
$889.2 \pm 3.0 \pm 3.8^*$	1996	J. Byrne *et al.*	[32]	penning trap	CN
$885.4 \pm 0.9 \pm 0.4^*$	2000	S. Arzumanov *et al.*	[33]	gravitational trap	UCN
$878.5 \pm 0.7 \pm 0.3^*$	2005	A. Serebrov *et al.*	[9]	gravitational trap	UCN
$886.3 \pm 1.2 \pm 3.2^*$	2005	J. S. Nico *et al.*	[8]	penning trap	CN
878.2 ± 1.9	2009	V. Ezhov *et al.*	[10]	magnetic trap	UCN
$880.7 \pm 1.3 \pm 1.2^*$	2010	A. Pichlmaier *et al.*	[34]	gravitational trap	UCN
881.5 ± 1.5	2011	Particle Data Group	[19]	—	—

Table 2.1: Summary of the experiments of the neutron lifetime. The world average given by the Particle Data Group combines the data with asterisk, which is also shown in Figure 2.6. CN, VCN and UCN stand for cold neutrons, cold neutrons and ultra cold neutrons.

where ϵ_p is the detection efficiency of the proton from the neutron decay, N is the neutron flux, v is the neutron velocity and L_1 is the length of the decay volume, which is located between a red part and a green part in Figure 2.7.

The neutron flux is independently monitored and the count rate S_n is given by

$$S_n = \epsilon_n N \rho \sigma L_2, \tag{2.8}$$

where ϵ_n is a detection efficiency of the triton and alpha from the neutron capture in ^{6}Li, ρ and σ denote the density and the cross section of the absorber, and L_2 is the thickness of the foil. From Eq. (2.7) and Eq. (2.8), the lifetime is expressed as

$$\tau_n = \frac{1}{\rho \sigma v} \left(\frac{S_n/\epsilon_n}{S_\beta/\epsilon_p} \right) \frac{L_1}{L_2}. \tag{2.9}$$

The neutron beam normally contains a broad spectrum of velocities. However, the absorption cross section of cold neutrons is approximately inversely proportional to the neutron velocity [35, 36], hence σv can be treated as a constant*.

---

*In a recent measurement, a capture cross section in ^{3}He is obtained as $(849.77 \pm 0.14 \pm$

The largest systematic uncertainties come from the accuracy of the densities of ^{6}Li. The uncertainty in the capture cross section of the ^{6}Li is also significant.
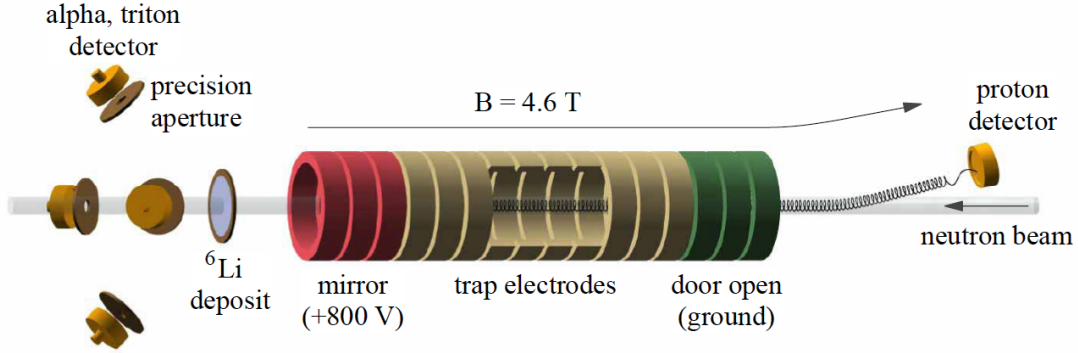
Figure 2.7: A schematic view of the experimental setup by means of beam method by the Sussex-ILL-NIST group [8].

2.3.3   Gravitational trap method

The UCNs are reflected off a surface of the material by Fermi potentials (~ 220 neV) and are trapped by gravity (102 neV/m). Thus the UCNs can be stored in a material bottle for a time comparable to the neutron lifetime. Then the surviving neutrons are counted. The UCNs are observed by Luschikov in 1968 [38] and the first measurement of the neutron lifetime by means of the gravitational trap method is done by Kosvintsev in 1980 [24]. The effects of the wall loss such as inelastic scattering has influence on the systematic uncertainty, which is caused by residual hydrogen atoms on the bottle, thus the study of the hydrogen-free oil such as fomblin oil are usually used to coat the wall. However it is difficult to evaluate the reflectivity of the surface with high precision.

The lifetime measurement uses the number of neutrons measured at two different storage times, S_1 and S_2. Hence the ratio S_1/S_2 is expressed with the neutron life time τ_n and the wall loss τ_{wall} as

$$\frac{\ln(S_1/S_2)}{\Delta t} = \frac{1}{\tau_n} + \frac{1}{\tau_{wall}}. \tag{2.10}$$

The most accurate experiment was developed by the PNPI group and operated at the ILL as shown in Figure 2.8. They invented a new coating, a fluorinated polyether similar to the fomblin oil that is evaporated onto a surface and forms a stable coating at cryogenic temperatures, in this case -160 °C. With this coating,

---

$1.02)E^{-\frac{1}{2}} - (1.253 \pm 0.00^{+0.008}_{-0.049})$ barn, where E is an energy of neutrons in a unit of eV [37]. In the case of cold neutrons, deviation from the 1/v law is less than 0.1%.

the inelastic scattering probability decreased by a factor of 10 smaller than that by the fomblin oil [7]. Consequently τ_{wall}^{-1} becomes 1% of τ_n^{-1}. The neutron lifetime from this experiment was $878.5 \pm 0.7 \pm 0.3$ s [9].
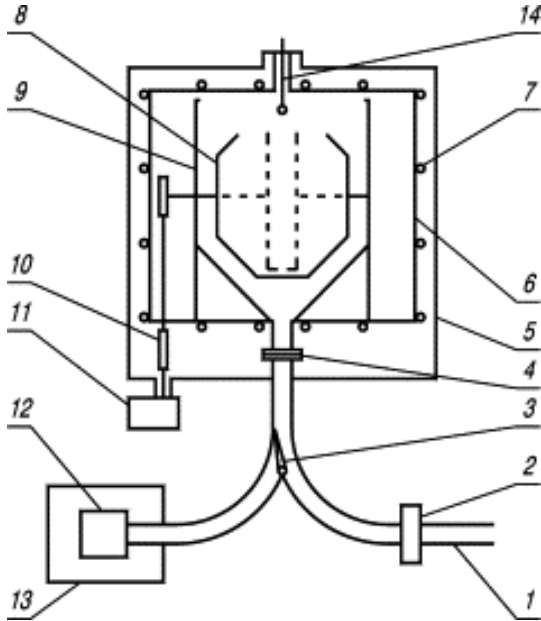
Figure 2.8: A schematic view of the experimental setup by means of the gravitational trap method by the PNPI group [9]: 1 input neutron guide for UCN, 2 inlet valve, 3 selector valve, 4 foil unit, 5 vacuum volume, 6 separate vacuum volume of the cryostat, 7 cooling system for the thermal shields, 8 UCN storage trap with the dashed lines depicting a narrow cylindrical trap, 9 cryostat, 10 trap rotation drive, 11 step motor, 12 UCN detector, 13 detector shield, and 14 vaporizer.
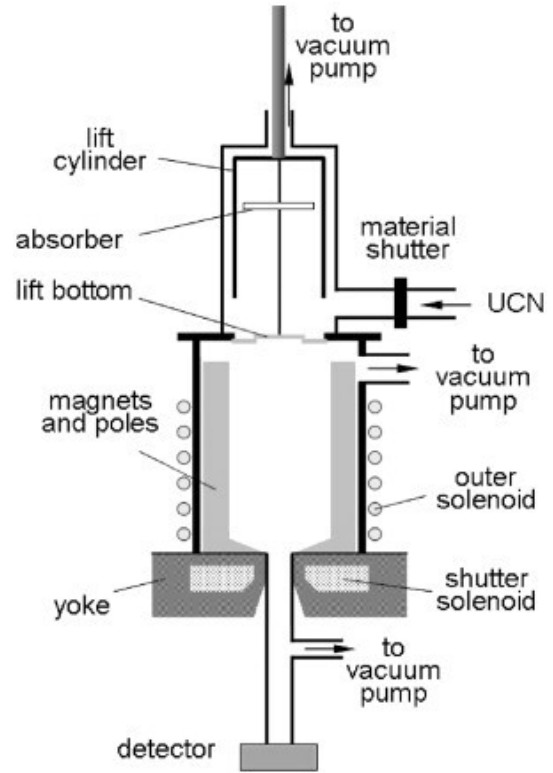
Figure 2.9: A schematic view of the experimental setup by means of the magnetic trap method by the ILL group [10].

2.3.4 Magnetic trap method

Neutrons have a magnetic dipole moment and can be trapped by magnetic-field gradients alone in order to avoid the loss when neutrons come in contact with the wall. The first such measurement is done by Anton *et al.* in 1989 [27] using very cold neutrons whose energy is between the cold neutron and the UCN. The magnetic dipole moment of the neutron is 60 neV/T, thus the gradient will provide a force that returns one spin state toward the center. In principle polarized neutrons can be trapped until they decay. However there is an important loss mechanisms:

the depolarization in the gradient field.

The latest measurement was performed at ILL [10] with UCNs instead of very cold neutrons as shown in Figure 2.9. While the measurement principle is similar to the bottle method, UCNs do not interact with matter in the wall during the storage interval. Neutrons enter the top of the bottle and go down to the main part formed with a cylindrical, 20-pole permanent magnet array. A result from this experiment has been presented at conferences: 878.2 ± 1.9 s but not yet published as of this writing. The quoted uncertainty is statistical only.

2.4   Beam method

A beam method was invented by Robson in 1951 [20], which uses cold neutrons and detects the decay products in flight. However it has not been performed for over 20 years after the experiment by Kossakowski *et al.* [11], which is the preceding study of the experiment in this thesis.

2.4.1   Principle of the Kossakowski's experiment

The electron from the neutron decay is detected in a time projection chamber (TPC). The continuos neutron beam from the reactor at the ILL go through a chopper, which forms monochromatic neutron bunches. Thus the spatial spread of the bunches is limited during their flight path in the TPC. Analyzing the events while the neutrons are completely in the TPC, a detection of 4π solid angle is guaranteed. One should note that only the electron from the neutron decay whose maximum energy is 782 keV can be detected by the TPC, but not the proton since the energy of the proton is less than 0.754 keV.

A small amount of ^{3}He is mixed with the gases. ^{3}He has a large neutron capture cross section of $\sigma_0 = 5333 \pm 7$ barn at $v_0 = 2200$ m/s [39], and the reaction products are the proton and triton whose energy are 572 keV and 191 keV, respectively. Thus the decay and the flux of neutrons can be simultaneously counted in the TPC. In the case of using ^{3}He gas, the density $\rho_{^3\text{He}}$ can be controlled by the pressure and confirmed by the mass spectrometer. Inserting $L_1 = L_2$ into Eq. (2.9), the lifetime is obtained as

$$\tau_n = \frac{1}{\rho_{^3\text{He}}\sigma_0 v_0} \left(\frac{S_n/\epsilon_n}{S_\beta/\epsilon_\beta} \right), \tag{2.11}$$

where ϵ_β is a detection efficiency for the electrons from the neutron decay.

In this method, the determination of the ^{3}He density directly influences the accuracy of the neutron lifetime, so that the gas composition must not change during the measurement. Thus the TPC is placed in a vacuum chamber, which is then filled with gas after vacuuming. The gases do not flow during the experiment.

2.4.2 Experimental setup for the Kossakowski's experiment

In Kossakowski's experiment, a mechanically rotating drum with a hole and a single crystal monochromator were employed as a chopper [40]. The rotating drum made a pulse, but the neutrons in the pulse had various velocities, so that its length did not remain constant as it got transported. Thus the monochromator was located in the downstream of the drum and was reflects neutrons with a certain velocity and then the bunch with a fixed length went to the TPC [41]. A schematic view is shown in Figure 2.10.
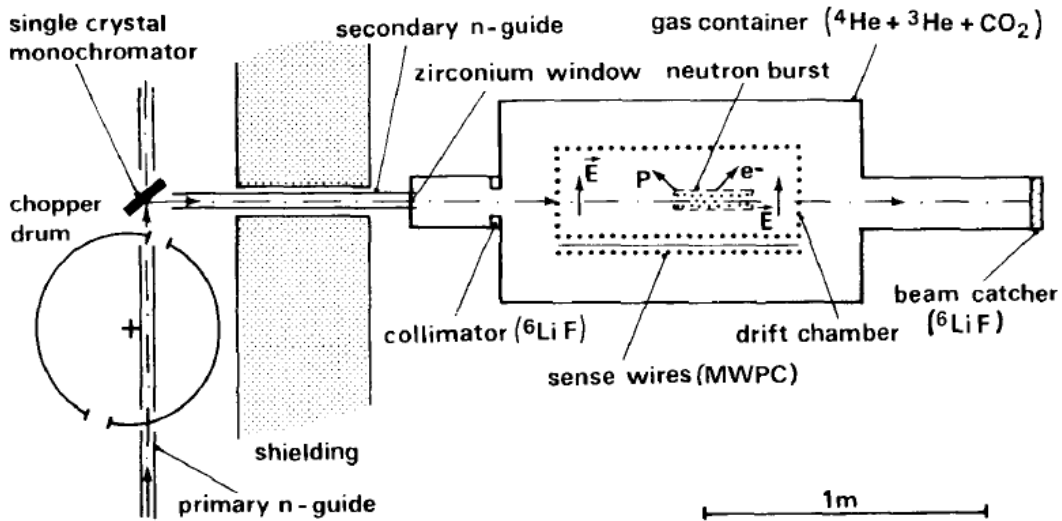
Figure 2.10: A schematic view of the experimental setup by Kossakowski *et al.* [11].

The selected velocity corresponds to 837 m/s, thus only a fraction of 10^{-6} of the neutrons decays within the TPC with a length of 700 mm, which corresponded to 0.1 cps of the neutron decay rate. Since the detectable particle from the neutron decay was only the electron, the background was mainly caused by environmental radiation. For shielding, the TPC was housed in 50 cm thick concrete walls and surrounded by 5 cm thick lead. Cosmic rays events were rejected by making use of plastic scintillators. The neutron capture γ rays also became background, which originated from the gases along the flight path. The gases also scattered the neutron inside the TPC with a probability of about 1% per meter, the materials
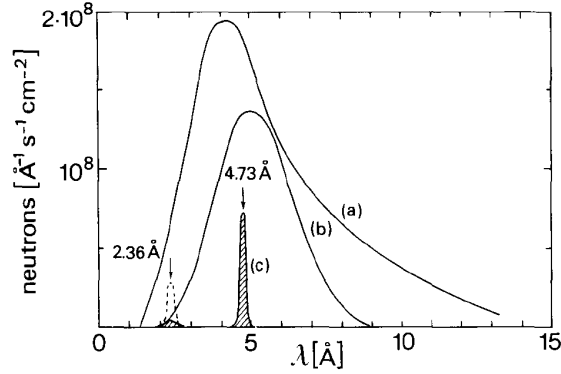
Figure 2.11: Wavelength spectrum of the neutrons at different points of the beam line.
(a) exit of main guide, (b) exit of chopper drum, (c) secondary beam. The first and the
second-order Bragg reflection lines are indicated (4.73 and 2.36 Å), which corresponds
to 837 m/s and 1674 m/s, respectively [11].

around the flight path became a source origin. For shielding the scattered neutrons,
the TPC was placed in a ^{6}LiF coated plexiglas box. ^{6}Li has a large neutron capture
cross section and the branching ratio of the reaction with γ rays is 4×10^{-5}. The
gases for the ionization and multiplication were He and CO_2, whose scattering and
capture cross section are shown in Table 2.2.

	σ_s(barn)	$\sigma_{2\mathrm{body}}$(barn)	σ_γ(barn)
^{3}He	6	5333	0
^{4}He	1.34	0	0
CO_2	14.0	0	0.0039
Ar	0.683	0	0.675
C_2H_2	175.1	0	0.672
C_2D_2	26.4	0	0.008
CH_4	333.6	0	1.33
N_2	23.0	3.66	0.160

Table 2.2: Cross sections for 2200 m/s neutrons in typical gases. The scattering cross
section σ_s does not consider the effect of molecular gas scattering described in Section
4.1.2. $\sigma_{2\mathrm{body}}$ denotes the capture without prompt γ rays and σ_γ denotes the capture
with prompt γ rays.

2.4.3   Results of the Kossakowski's experiment

It took 34 hours to take the data for the first result, $878 \pm 27 \pm 14$ s, whose
uncertainties arised from following items:

- Low statistics due to monochromator,

The wavelength spectrum of the neutrons are shown in Figure 2.11. It is found that almost the neutrons transmit the monochromator, while only a fraction of the neutrons arrived into the TPC. The rate of the neutron decay (S_β) was 0.1 cps, which caused a large statistical uncertainty of 3.1%. The rate of capture of neutron by ^{3}He (S_n) was controlled by the gas pressure and it was set at 1.8 cps.

- Remained background after shielding the radiation,
  After shielding, the environmental background (B_e) and the beam induced background (B_b) remained 80 cps and 20 cps, which dominated the rate of the neutron decay. In order to compare the rate of the neutron decay with that of other background, it is useful to convert it to the case of a continuos beam as 0.1 cps $\times \frac{1 \text{ s}}{400 \ \mu s \times 110 \text{ Hz}} \sim 2$ cps. For this conversion, the duty cycle of the beam pulse is used.

- Low detection efficiency due to the signal selection by using track pattern,
  In order to increase the signal-to-background ratio, the background to the neutron decay was strictly reduced by using signal selection. The electrons from the neutron decay originate along the beam axis, which corresponds to the center of the TPC. Thus they rejected the events whose end points of tracks did not match the center of the TPC, then only the 8% of the background was remained after the selection (ϵ_B). However the rejected events included the electrons from the neutron decay, which are scattered on the material of the TPC, for instance. As a result, the signal selection criteria reduced the detection efficiency for the neutron decay to 87.2% (ϵ_β), which resulted in 1.1% of systematic uncertainty for the correction of the detection efficiency.

  In addition, the separation between the neutron decay and the ^{3}He reaction due to the saturation effect as described in Section 4.4, which reduced the detection efficiency for the ^{3}He reaction to 99.6% (ϵ_n) and introduced 0.6% of systematic uncertainty for the correction of the detection efficiency.

- Subtraction of the background by using sideband region.
  The subtraction of the beam-induced background caused by scattered neutron by gas is difficult for the subtraction since it is associated with the neutron decay. They assumed an isotropic beam-induced background to the neutron decay, and subtracted it by using the sideband region outside the fiducial volume where the neutron decay did not occur. In their analysis

0.9% of the systematic uncertainty was ascribed.

As a result, the lifetime was obtained with 3.5% uncertainties.

Facility	reactor in ILL
Repetition rate	110 Hz
Pulse per repetition	1
Length of pulse	230~250 mm
Velocity	837 m/s
Fiducial time	400 μs
Beam cross-section	15 mm $\times$ 25 mm
Divergence	$\pm$8.7mrad
TPC gas	He : CO_2 = 93 : 7
Gas pressure	95 kPa
Dimensions of TPC	190 mm$\times$190 mm$\times$700 mm
Neutron decay rate (S_β)	0.1 cps
Neutron capture rate in ^{3}He (S_n)	1.8 cps
Environmental background (B_e)	80 cps
Beam-induced background (B_b)	20 cps
Remained background after the selection (ϵ_B)	8%
Efficiency for the neutron decay (ϵ_β)	87.2%
Efficiency for the ^{3}He reaction (ϵ_n)	99.4%
Beam time	34 hour
Statistical uncertainty	3.1%
Correction for ϵ_β	1.1%
Correction for ϵ_n	0.6%
Subtraction of B_b	0.9%
Cross section of ^{3}He	0.17%
Result	$878 \pm 27 \pm 14$ s

Table 2.3: Parameters of the experiment by Kossakowski *et al.* The neutron bunch after the chopper, characteristics of the TPC, and systematic uncertainties are summarized.

Chapter 3

Experiment in this thesis

The key points of the experiment in this thesis are

- monochromatic neutron bunches whose length is shorter than the TPC,

- coincident detection of the neutron decay and the neutron flux in the TPC,

which were conceived by Kossakowski *et al.* In this chapter, the novel approach undertaken in the experiment as well as the experimental setup are described.

3.1   Approaches in this thesis

In order to overcome their shortcomings as discussed in Section 2.4, new approaches are proposed in this thesis as follows. Comparison between the Kossakowski's experiment and this work is summarized in Table 3.1. The whole setup of the experiment is shown in Figure 3.1. The schematic view of the TPC is shown in Figure 3.2.

- Pulsed neutron source / spin flip chopper
  In order to make a high intensity bunch, a pulsed neutron source is more suitable than continuous neutrons extracted from reactors, since the neutron pulse broadens according to its velocity profile. In other words, neutrons with a certain velocity can be selected by means of the time of flight (TOF) with a chopper. Thus the bunch can remain undispersed after the chopper, eliminating the need for a monochromator, so that the transportation efficiency of the neutron becomes better. For this purpose a "spin flip chopper" is newly employed instead of the rotating drum [42]. In the case of the pulsed neutron source, the cycle of the chopper has to decrease with increasing time of flight for a constant length of the bunch, while the cycle rate of the rotating drum used by Kossakowski was kept constant. The SFC can change the

direction of the neutron in a certain region of TOF spectrum by means of the radio frequency, so that it can control the length of the neutron bunch and the repetition rate. The neutron beam and the SFC are described in Section 3.2 and Section 3.3, respectively.

- 4π shielded TPC with no radioactive contamination
  The TPC developed by Kossakowski *et al.* was not cared for the radioactive contamination and was made of no special low-activity material. For the evaluation of the radioactive contamination, many materials are investigated by a germanium detector; a TPC made of polyethel ethel ketone (PEEK) has been developed as described in Section 6.1. In order to shield the scattered neutrons ^{6}Li plates are installed inside the TPC as described in Section 6.2. A lead box and plastic scintillators are designed to surround the TPC with 4π solid angle coverage as described in Section 3.6. Moreover, shields around the SFC and an iron wall are installed to reduce the background arising from the neutron beam as described in Section 3.7. Consequently, the background to the neutron decay can be reduced to 1/10 compared with the TPC developed by Kossakowski *et al.*

- High detection efficiency by use of calorimetric approach
  In this thesis, the TPC employs a calorimetric approach, which achieves more than 99.9% detection efficiencies of the neutron decay and the neutron capture in ^{3}He as described in Section 5.4. Moreover the reduction of the backgrounds makes it possible to loosen the selection for the neutron decay. The ratio of remained background after the selection (ϵ_B) becomes 25%, which increases the detection efficiency as described in Section 5.5. Thus the systematic uncertainty for the correction of the detection efficiency is reduced to 0.1%.

- Subtraction of beam-induced background by use of a data-driven approach. Kossakowski *et al.* accounted 0.9% of systematic uncertainty for the estimation of the beam-induced background by means of the sideband region. In this thesis, new sources of background are investigated at first. Subsequently, the beam-induced background is classified in terms of its origin and subtracted by using ^{3}He-enriched measurements, time of flight spectra and reduced-pressure measurements as described in Section 5.6, 5.7 and 5.8, which reduces the systematic uncertainty to be less than 0.1%.
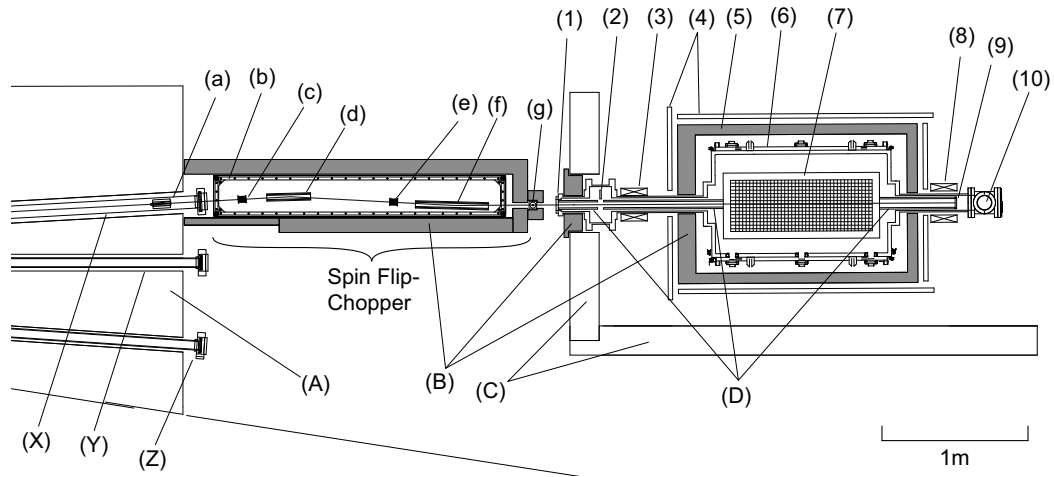
Figure 3.1: A drawing of the experimental setup: (A) beam dump, (B) lead shield, (C) iron shield, (D) ^{6}LiF-PTFE beam collimator, (X) Polarization branch, (Y) Unpolarization branch, (Z) Low divergence branch, (a) short-pass wavelength neutron filter, (b) guide coil, (c) spin flipper, (d) magnetic super mirrors, (e) spin flipper, (f) magnetic super mirrors, (g) neutron beam monitor, (1) Zr window, (2) neutron switching shutter, (3) electron suppression magnet, (4) cosmic veto counter, (5) lead shield, (6) vacuum chamber, (7) TPC, (8) electron suppression magnet, (9) ^{6}LiF beam catcher, and (10) turbo molecular pump.
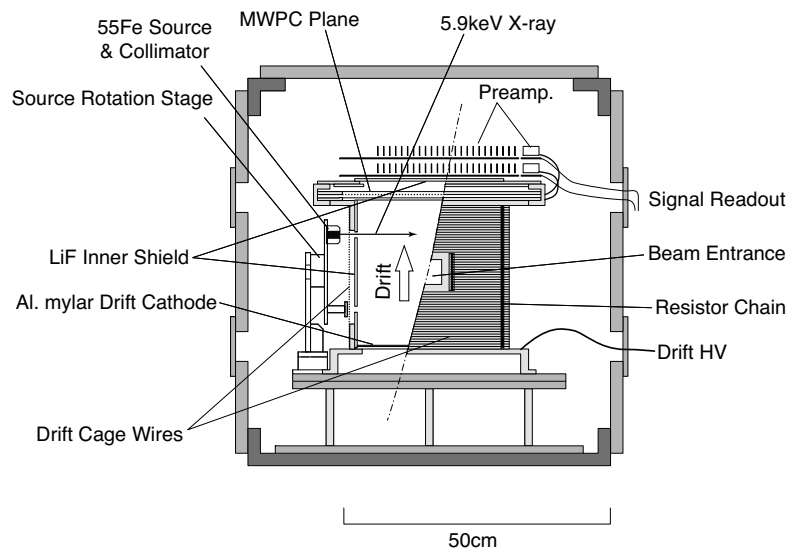
Figure 3.2: A schematic view of the time projection chamber (front view).

	Kossakowski	This work
Facility	reactor in ILL	J-PARC
Repetition rate	110 Hz	40 Hz
Pulse per repetition	1	5∼6
Length of pulse	230∼250 mm	400 mm
Velocity	837 m/s	500 m/s $\sim$ 1200 m/s
Duty factor	4.4%	$\sim$ 7%
Beam cross-section	15 mm×25 mm	20 mm × 20 mm
Divergence	±8.7mrad	±4.2 mrad
TPC gas	He : CO_2 = 93 : 7	He : CO_2 = 85 : 15
Gas pressure	95 kPa	50 kPa $\sim$ 100 kPa
Dimensions of TPC	190 mm × 190 mm × 700 mm	300 mm × 300 mm × 960 mm
S_β	0.1 cps	0.1 cps
S_n	1.8 cps	1∼3 cps
B_e	80 cps	8 cps
B_b	20 cps	2 cps
ϵ_B	8%	25%
ϵ_β	87.2%	> 99.9%
ϵ_n	99.4%	> 99.9%

Table 3.1: Comparison between the preceding study and this work assuming 220 kW of beam power at J-PARC. Parameters of the neutron bunch after the chopper, characteristics of the TPC, and the systematic uncertainties are summarized.

3.2 Neutron Beam

The experiment in this thesis employs the Polarization beam branch at a beamline for neutron fundamental physics (BL05), Material and Life Science Experimental Facility (MLF), Japan Proton Accelerator Research Complex (J-PARC). The property of the pulsed proton provided by Rapid-cycling Synchrotron (RCS) in J-PARC is described in Section 3.2.1. The property of the spallation neutron at the target in MLF is also described. Section 3.2.2 describes the characteristics of each beam branch at BL05 in MLF.

3.2.1 MLF/J-PARC

J-PARC is constructed in JAEA Tokai site as a joint project of the Japan Atomic Energy Agency (JAEA) and High Energy Accelerator Research Organization (KEK) . At J-PARC, a proton linac and 3 GeV and 30 GeV proton synchrotrons will provide MW-class proton beams.

These high intensity proton beams are used to produce various secondary and successive decay particle beams. There are 4 major experimental facilities: Neutrino Facility, Nuclear and Particle Physics Experimental Hall (Hadron Hall), Materials and Life Science Experimental Facility (MLF) and Transmutation Experimental Facility.

Figure 3.3: A bird's view of the J-PARC accelerator [43].

Parameter	Value
Designed injection energy from Linac	400 MeV
Achieved injection energy from Linac	181 MeV
Extraction energy	3 GeV
Designed beam power	1 MW
Achieved beam power	220 kW
Repetition rate	25 Hz

Table 3.2: Parameters of RCS [43].

MLF is aimed at promoting materials science and life science using the intense pulsed neutron and muon beams which are produced using pulsed 3 GeV protons with a repetition rate of 25 Hz. The protons are provided by RCS, which accelerates proton beams from 181 MeV (in the first stage) to 3 GeV. While the design goal of the beam power is 1 MW, the achieved beam power in 2011 is about 220 kW.

The pulsed protons reach into a liquid mercury target at MLF. The resulting spallation neutrons are slowed down in moderators to 1 meV $\sim$ 20 meV, so-called cold neutrons, and have a velocity spectrum of 500 m/s $\sim$ 2000 m/s. There are three types of moderators: coupled moderator, decouple moderator and poisoned moderator. Among the moderators, the coupled moderator provides the most intense neutron beam and is employed for the experiment in this thesis. All moderators circulate supercritical H_2 at 20 K and 1.5 MPa and provide cold neutrons to 23 beam ports. The cold neutrons under Maxwell-Boltzmann velocity distribution are provided to each beam line and are broaden in the experimental areas at a distance of about 16m from the moderator.

Type of moderator	Number of beam port	Time-integrated thermal neutron flux [1/s/cm^2/MW]	Peak Neutron flux at 10 meV [1/eV/s/cm^2/MW]	Pulse width in FWHM at 10 meV
Coupled	11	4.6×10^8	6.0×10^{12}	92
Decoupled	6	0.95×10^8	3.0×10^{12}	33
Poisoned (thicker side)	3	0.65×10^8	2.4×10^{12}	22
Poisoned (thinner side)	3	0.38×10^8	1.4×10^{12}	14

Table 3.3: Designed values of the neutron source at 10m from the moderators assuming 1 MW of the beam power at J-PARC [43].

3.2.2 Polarization branch on BL05

BL05 provides neutrons moderated at the coupled moderator and divides them into three characteristic branches by the bender at a distance of $7.2 \sim 12$ m from the moderator. These branches are called as "Polarization beam branch", "Unpolarization beam branch" and "Low-divergence beam branch".

- The Polarization beam branch is designed for the measurement of lifetime of the neutron and the angular correlation of the neutron decay. Magnetic supper mirror, described in Section 3.3.2 in detail, is housed in the beam bender; only the neutrons whose spin is parallel to the magnetic field are reflected to the downstream.

- The Unpolarization beam branch produces the highest energy and most intense neutron flux of these branches with a super-mirror bender. This beam branch is designed for experiments of neutron small angle scattering to search for a new medium range force and also to produce ultra cold neutron by a Doppler shifter.

- The Low-divergence beam branch is designed for an experiment of a neutron interferometer, which consists of two super-mirror surfaces.

At the distance of 11.75 m from the moderator, horizontal and vertical beam slits were installed to define the beam width and position at the ends of each beam bender. After the slit, the neutrons pass through the boron-lining vacuum duct surrounded by iron and concrete shielding. A drawing of the BL05 and each beam branch are described in Figure 3.4 and Figure 3.5. The flux and the TOF spectrum of the neutron beam are shown in Table 3.4 and Figure 3.6.

Position	Cross Section [cm^2]	Divergence [μstr]	Flux [1/s/cm^2/MW]
(A)	10.0×11.0	2.0×10^2	$(7.3 \pm 0.9) \times 10^8$
(B)	10.0×4.0	1.9×10^2	$(3.9 \pm 0.3) \times 10^7$
(C)	5.0×4.0	1.0×10^2	$(9.4 \pm 0.7) \times 10^7$
(D)	10.0×1.0	5.4×10^{-2}	$(5.4 \pm 0.5) \times 10^4$

Table 3.4: Measured fluxes, divergences at each position in BL05 as described in Figure 3.4.
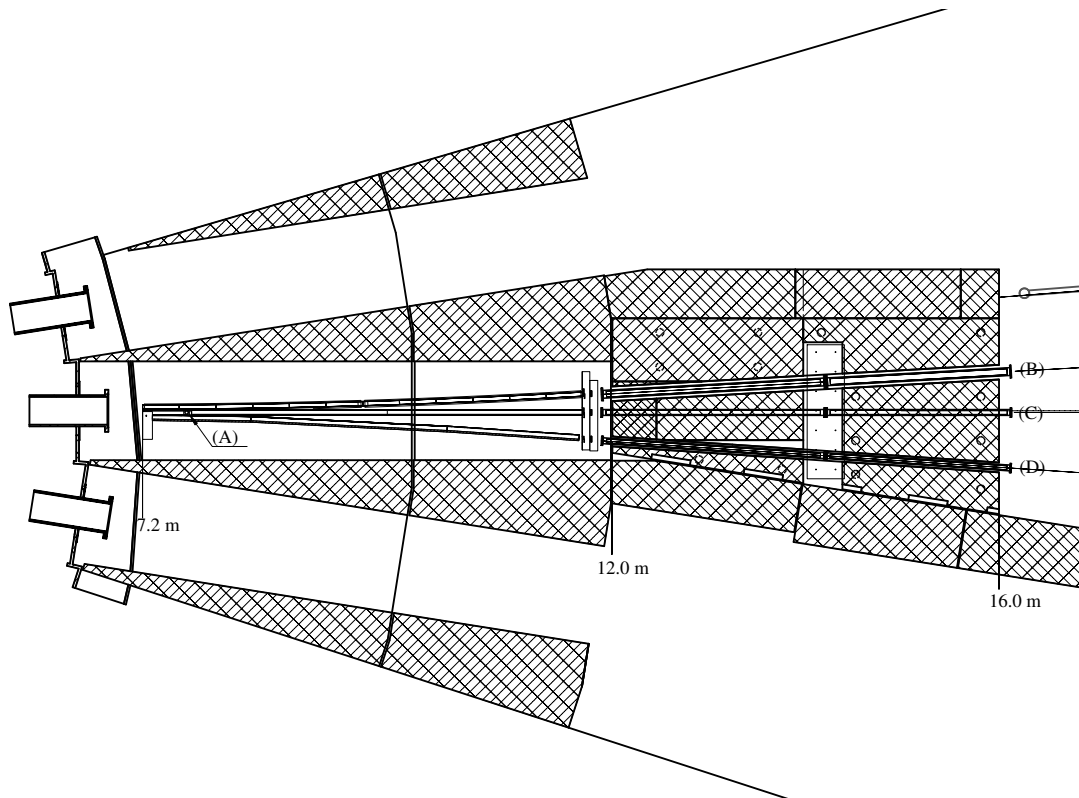
Figure 3.4: A drawing of the BL05; (A) Upstream of the beam benders, (B) Exit of Polarization beam branch, (C) Exit of Unpolarization beam branch, and (D) Exit of Low-divergence beam branch.
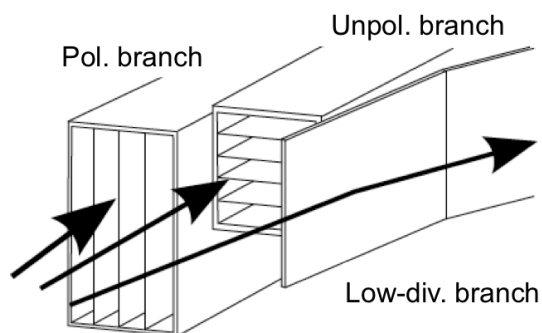
Figure 3.5: A schematic view of each beam branch at upstream of the beam benders in BL05.
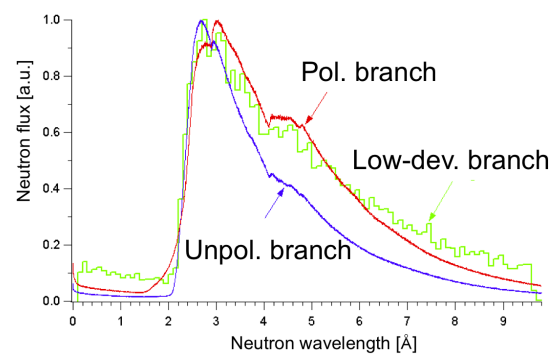
Figure 3.6: Measured neutron flux of each beam branch in BL05.

3.3 Spin flip chopper

In this section, the principle and the performance of the spin flip chopper (SFC) are described. The flight path of the neutron depends on the spin state as described in Section 3.3.1. The SFC has two components, a magnetic super mirror (MSM) and a radio frequency flipper (RFF) in the guide coil, which are described in Section 3.3.2 and 3.3.3, respectively. The performance of the SFC is presented in Section 3.3.4.

3.3.1 Overview of the SFC

The overall view of the SFC is found in Figure 3.7. There are three MSM and two RFF in the guide coil. The MSM is made of several hundred double layers of ferromagnetic-nonmagnetic material inside the permanent magnet. The MSM reflects the neutron from the Polarization branch whose spin is parallel to the magnetic field, while neutrons with an opposite spin are transmitted. The RFF provides an AC magnetic field inside the solenoid coil. If the strength and frequency of the AC magnetic field satisfy the resonance condition with the guide coil, the Larmor rotation starts inside the solenoid coil and the spin of the neutron flips.

Figure 3.8 (top) shows the neutrons from the polarized branch reflected at all the MSM when the RFF is turned off. Figure 3.8 (bottom) shows the neutrons transmitted at the first MSM when the RFF is turned on. Thus RFF can control the length and the repetition of the neutrons which are transported into the TPC.
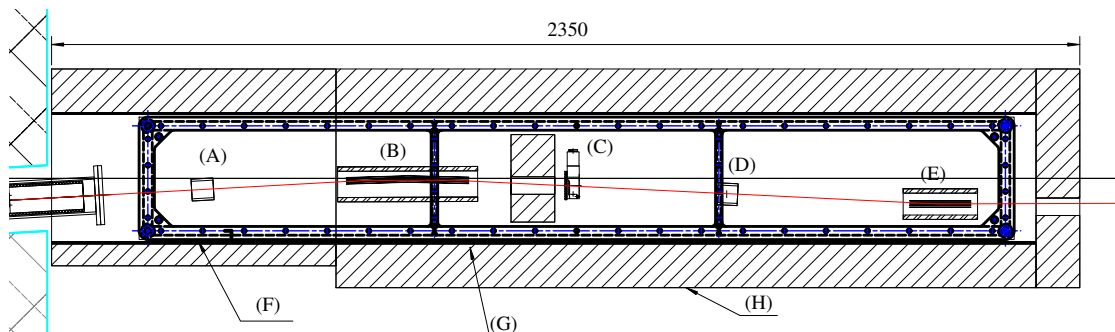
Figure 3.7: A drawing of the SFC at Polarization branch in BL05: (A)a first radio frequency flipper, (B) first and second magnetic supper mirrors, (C) a ^{6}Li shutter, (D) a second radio frequency flipper, (E) a third magnetic supper mirror, (F) a guide coil, (G) boron gum, and (H) lead shields.
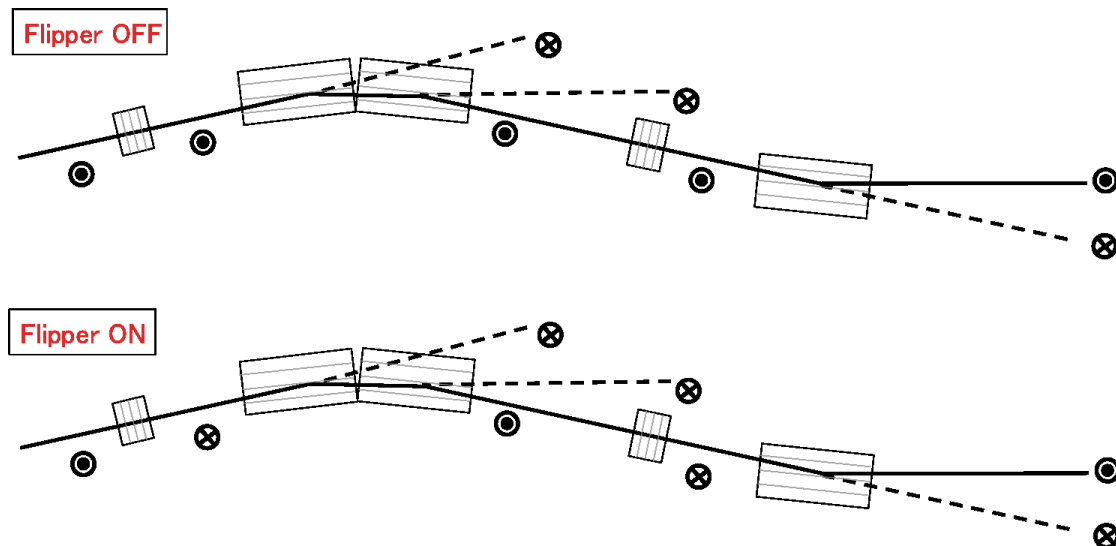
Figure 3.8: A schematic view of the SFC.

3.3.2   Magnetic supper mirror

Let us consider a thin-layer with the angle of the incident neutron θ as shown in Figure 3.9. If the neutron energy perpendicular to the thin-layer is less than the nuclear potential of the thin-layer, the incident neutrons are reflected. However, even one of the largest effective potential is 220 neV for nickel, which corresponds to the speed of neutron of 6.8 m/sec. Thus, in order to make it larger, Mezei proposed a supper mirror alternately stacked two materials with different effective potential by changing their thickness [44]. Consequently, the energetic neutrons are reflected depending of the thickness by means of Bragg reflection. In the field of neutron optics, when the effective potential of the supper mirror is larger than that of the nickel by a factor of m, it is expressed as mQ_c. The performance of the supper mirror with large m-value is sensitive to the roughness of the surface and it is difficult to attain high reflectivity. The relationship between m-value and the number of the layer N is expressed as $N \simeq 4m^4$.

The "magnetic" supper mirror stacks the ferromagnetic and nonmagnetic material, which is placed in strong enough magnetic field to induce magnetic-field saturation (B_s) in the ferromagnetic material. The potential of the ferromagnetic material is expressed as a sum of the nuclear potential V_{nucl} and the magnetic potential $\pm\mu_n B_s$. Thus the nonmagnetic material is selected as its nuclear potential is equal to $V_{nucl} - \mu_n B_s$. As a result, the neutrons whose spin is antiparallel to the magnetic field does not feel the potential gap and transmit the layers. It means the MSM works as a polarizer of the neutron spin.
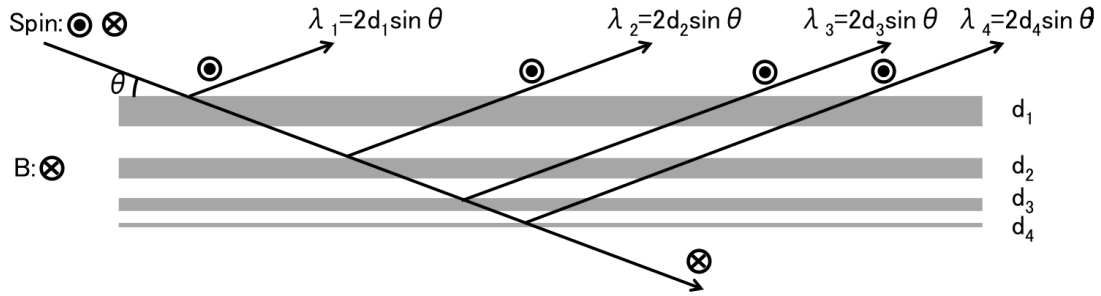
Figure 3.9: A schematic view of the cross section of the magnetic supper mirror.

For this experiment, the magnetic supper mirrors were fabricated with sputtering ion beam in Kyoto University Research Reactor Institute (KURRI) and the specification is summarized in Table 3.5. As shown in Figure 3.10, five of the mirrors are housed in the permanent magnet.

ferromagnetic material	Fe
non-magnetic material	$SiGe_3$
the number of layers	7445
thickness of the thinnest layer	1.9 nm
thickness of the thickest layer	60 nm
critical angle of the mirror	$5\,Q_c$
size of the mirror	140 mm $\times$ 35 mm$\times$ 0.7 mm
gap between mirrors	2.9 mm
the number of mirrors	5
magnetic field	35 mT

Table 3.5: Specification of the magnetic supper mirror.

3.3.3 Radio-frequency flipper

The radio frequency flipper (RFF) consists of the guide coil and the solenoid coil as shown in Figure 3.11 and can be divided into three regions which are depicted in Figure 3.12. The region 1 and region 3 correspond to the outside of the solenoid coil and the constant magnetic field B_y is provided by the guide coil. Inside the solenoid coil, region 2, the constant magnetic field B_y and the AC magnetic field B_z at a frequency ω are provided.

The neutrons are passing through the regions in order and the flipping proba-

Figure 3.10: A photograph of a magnetic supper mirror (MSM).
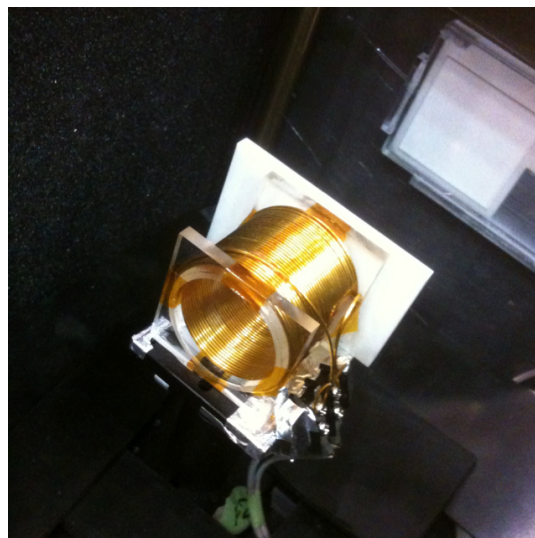
Figure 3.11: A photograph of a radio frequency flipper (RFF).
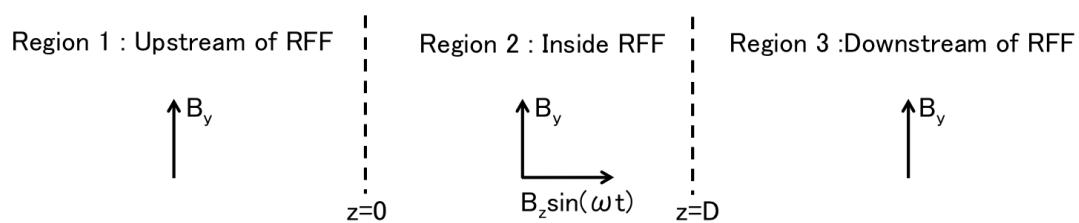
Figure 3.12: An illustration of the Larmor precession inside the radio frequency flipper.

bility in the region 2 is described as

$$
\begin{aligned}
P \ = \ & \frac{B_z^2}{B_z^2 + (B_y - \frac{\hbar}{2|\mu_n|}\omega)^2} \sin^2\left(\sqrt{B_z^2 + \left(B_y - \frac{\hbar}{2|\mu_n|}\omega\right)^2}\, t\right) \\
& + \frac{B_z^2}{B_z^2 + (B_y + \frac{\hbar}{2|\mu_n|}\omega)^2} \sin^2\left(\sqrt{B_z^2 + \left(B_y + \frac{\hbar}{2|\mu_n|}\omega\right)^2}\, t\right).
\end{aligned}
$$

Assuming $B_y \gg B_z$, the probability equals to 1 in case of $\frac{\hbar}{2|\mu_n|}\omega = B_y$ and $B_z t = (n + 1/2)\pi$, which is called as the resonance condition. The specification in this experiment is summarized in Table 3.6.

Diameter of solenoid	50 mm
Length of solenoid	40 mm
Frequency of the magnetic field of the solenoid coil	29 kHz
Amplitude of the magnetic field of the solenoid coil	0.3 mT
Strength of magnetic field of the guide coil	1 mT

Table 3.6: Specification of a radio frequency flipper.

3.3.4 Performance

In practice, some neutrons are reflected at the MSM when the RFF is turned on, since the following items are less than 1:

- $1 - \epsilon_0$: the polarization degree of the polarized branch,

- $1 - \epsilon_R$: the flipping ratio by the RFF,

- $1 - \epsilon_M$: the transmission of the undesirous neutron at the MSM.

ϵ_0, ϵ_R and ϵ_M are around 5×10^{-2}. In this experiment, two RFFs and three MSMs are employed to improve the beam extinction while the RFF is in operation.

Φ_{Beam} represents the spin component of the polarized branch. M_R and M_M denote the transportation matrices of RFF and MSM, respectively. These are expressed with ϵ_0, ϵ_R and ϵ_M:

$$
\Phi_{Beam} = \begin{pmatrix} 1 \\ \epsilon_0 \end{pmatrix}, \quad M_R = \begin{pmatrix} \epsilon_R & 1 \\ 1 & \epsilon_R \end{pmatrix}, \quad M_M = \begin{pmatrix} 1 & 0 \\ 0 & \epsilon_M \end{pmatrix}. \tag{3.1}
$$
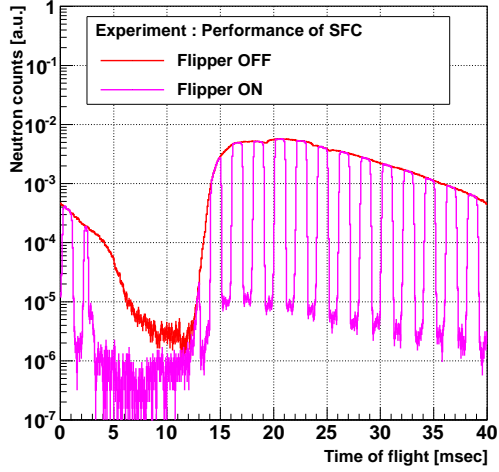
Figure 3.13: Performance of the Spin Flip Chopper.
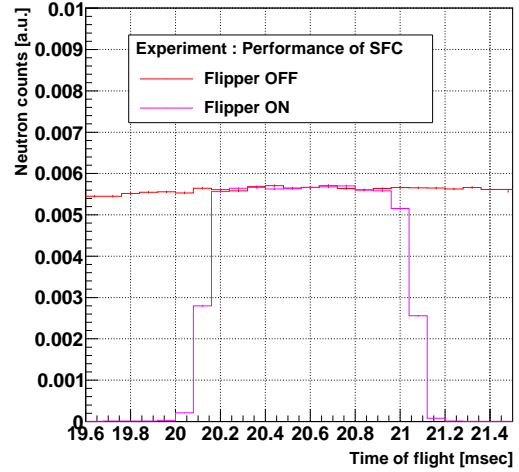
Figure 3.14: Magnified view of Figure 3.13.

Φ_{ON} and Φ_{OFF} are the spin component of the neutrons which go to the TPC when the RFF turns on and turns off, respectively. These can be calculate as

$$
\begin{aligned}
\Phi_{ON} &= M_M^3 \Phi_{Beam} = \begin{pmatrix} 1 \\ \epsilon_0 \epsilon_M^3 \end{pmatrix}, \\
\Phi_{OFF} &= M_M M_R M_M^2 M_R \Phi_{Beam} = \begin{pmatrix} \epsilon_R(\epsilon_0 + \epsilon_R) + \epsilon_M^2 \\ \epsilon_M(\epsilon_0 + \epsilon_R) \end{pmatrix}.
\end{aligned}
$$

From this equation, Φ_{OFF} is expected to be suppressed down to $O(\epsilon^2)$.

The performance of the SFC is shown in Figure 3.13 and Figure 3.14. The contrast of $\Phi_{ON}/\Phi_{OFF} \sim 400$ is achieved. The raising and falling time is about 0.5 ms which corresponds to the length of the RFF, 5 cm. The minimum length of the bunch is 15 cm. These values are summarized in Table 3.8

Cross section of the bunch	2 cm × 2 cm
Minimum length of the bunch	15 cm
Rising slope of the bunch	5 cm
Φ_{ON}/Φ_{OFF}	400

Table 3.7: The performance of the developed SFC.

3.4 Time projection chamber

This section describes the key points of the time projection chamber (TPC) for the simulation (see Chapter 4) and the analysis algorithm (see Chapter 5).

3.4.1 Overview of the TPC

The TPC has a rectangle MWPC part above an open-topped cuboid drift part. In this thesis, z-axis corresponds to direction of the neutron beam. Then y-axis is perpendicular to the ground. Applying high voltage on the bottom of TPC, ionized electrons along the trajectory of a charged particle inside the drift part travel to MWPC part. The TPC is set in the vacuum chamber and the gases are filled after the evacuation.

Sensitive region of the TPC	290 mm (x) $\times$ 300 mm (y) $\times$ 960 mm (z)
Number of anode wire	24 (z direction)
Number of field wire	24 (z direction)
Number of cathode wire	160 $\times$ 2 (x direction)
Gas mixture	He : CO_2 = 85 : 15 with a few ppm of ^{3}He
Gain	50000
Drift velocity	10 mm/μs
Total pressure	50 kPa $\sim$ 100 kPa
High voltage for the drift	6 kV $\sim$ 9 kV
High voltage for the ionization	1450 V $\sim$ 1720 V

Table 3.8: The basic parameter of the TPC.

The TPC in this thesis is completely different from the TPC developed by Kossakowski *et al.* in two ways:

- made of PEEK which contains no radioactive contamination,

- installed ^{6}Li plate for the capture of scattered neutron.

The detailed design and the performance are described in Chapter 6.

3.4.2 Pre-amplifier

The collected charge on the wires is converted to the voltage signal by a charge sensitive preamplifier. The gains, 1 V/pC and 0.1 V/pC, are designed for the neutron decay and the neutron capture in ^{3}He, respectively. The electric connection with wires are summarized in Table 3.9.

Top LiF Frame

Anode/Cathode Frame (t6)

Cathode Frame (t6)

Field Cage Frame (Top)

Field Cage Frame (Bottom)

412.0

MWPC Hanger

Field Cage Front Panel

Field Wire Land (t2)

418.0

400.0

550.0
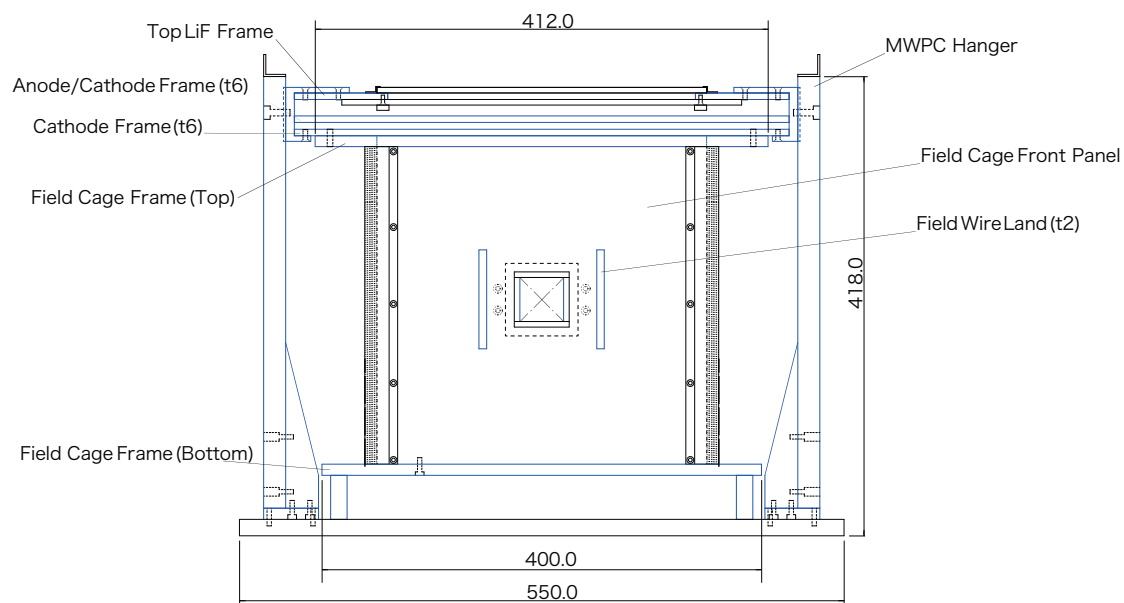
Figure 3.15: A drawing of the front of the TPC (x-y plane).

Top LiF Frame

Anode/Cathode Frame

Cathode Frame

Field Cage Frame (Top)

Side Bar

Corner Piller

MWPC Hanger

Field Cage Frame (Bottom)

Al Pedestal

1070.0

1032.0

289.0

980.0

1080.0
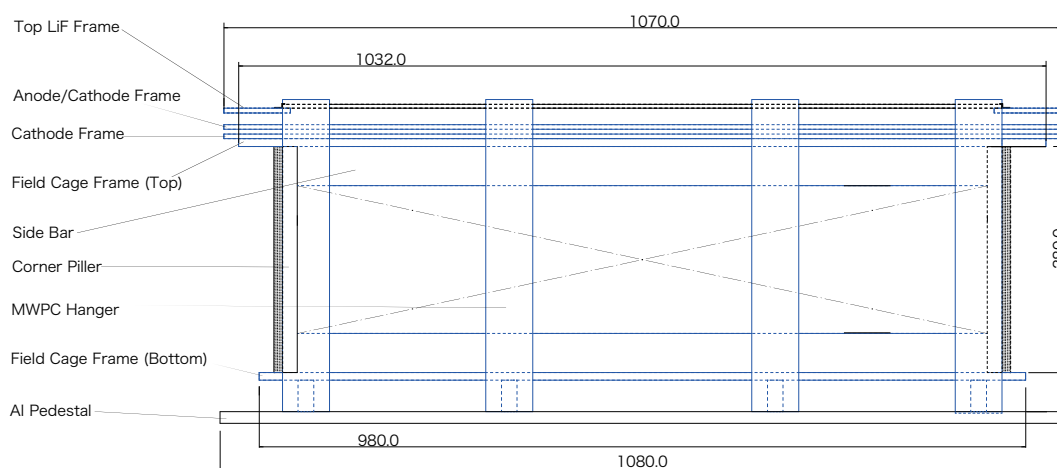
Figure 3.16: A drawing of the side of the TPC (y-z plane).

	Low gain amplifier	High gain amplifier
Wire	anode / cathode (bottom)	field / cathode (top)
Channel	24 ch / 40 ch	24 ch / 40 ch
Gain	1 V/pC	0.1 V/pC
Shaping time	0.5 μsec	0.5 μsec
Consumption power	500 mW/ch	500 mW/ch
ENC	8000	80000

Table 3.9: Specification detail of the pre-amplifier and wire connections.

The circuit board with OPA656 produced by Texas Instruments is developed by S. Satoh (KEK) and the values of discrete components are optimized for this experiment as shown in Figure 3.17. The current fed into the circuit is controlled by R_1 and R_2, which reduce the current to 1/10 in the low gain mode. The first time constant, 7.7 μsec, is set to maximize the signal-to-noise ratio and the signals are shaped in the differentiating and integrating circuit of about 0.5 μsec time constant.
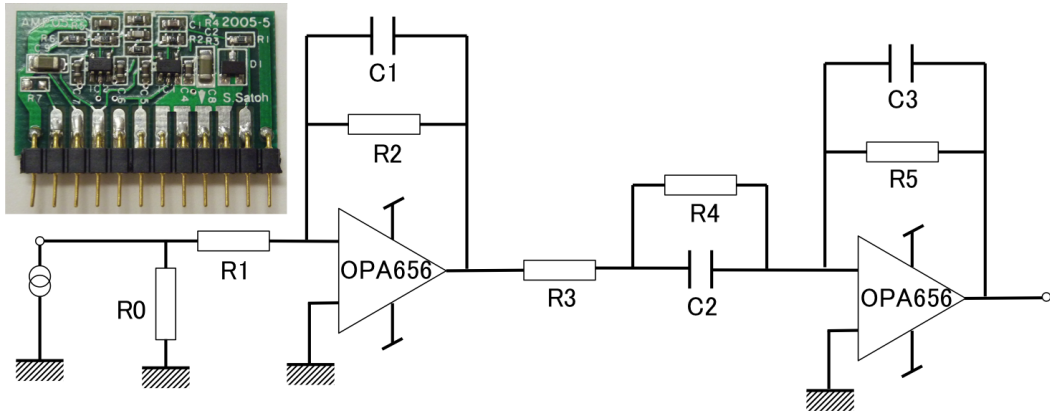
Figure 3.17: A circuit of the amplifier for this thesis. R_0 = NoConnect and $R_1 = 0\Omega$ in high gain mode. R_0=1k Ω and R_1=10 $k\Omega$ in the low gain mode. C_1=1.5 pF, C_2=330 pF, C_3=47 pF, R_2=5.1 MΩ, R_3=1 kΩ, R_4=24 kΩ, and R_5=11 kΩ in common.

3.4.3 Trigger

An event for the acquisition is triggered when any signal of the anodes exceeds the threshold which corresponds to 200 eV. A block diagram of the electronics is given in Figure 3.18. In order to suppress the background due to cosmic ray, signal from the scintillators surrounded TPC vetoes the trigger for 50 μs. Subsequently the waveforms of all wires and the time of flight are recorded via FADC and TDC on

Copper-Lite.
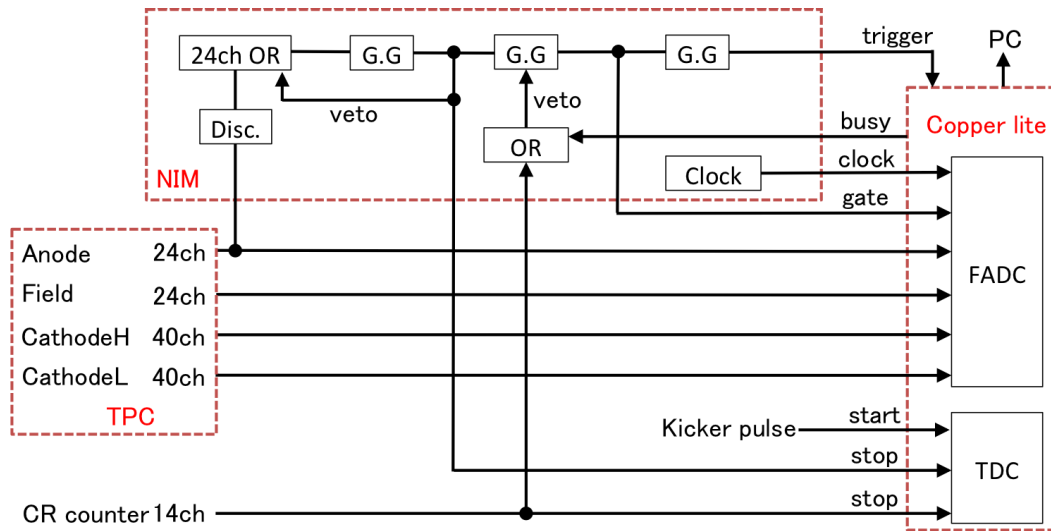
Figure 3.18: A circuit for the trigger and the data acquisition.

3.4.4 Frontend electronics

KEK online group has developed a general purpose pipeline readout board, COP-PER(COmmonPipelined Platform for Electronics Readout), which has four daughter cards, collectively called FINESSE (Front-end INstrumentation Entity for Sub-detector Specific Electronics). Many type of FINESSE such as 500 MHz FADC have been also developed. The data from the FINESSEs is built on the COPPER and transferred via an ethernet port. The acquisition dead-time is 300 μs/event and the busy signal from the Copper-Lite is also considered.

Our using FINESSE and improvement of the FPGA are as follows:

- 65 MHz 12 bit FADC

  The default firmware does not support the self-trigger since the write operation starts at a falling edge of the trigger signal. Thus a ring buffer in the FIFO is implemented, which enables to take the data before the trigger signal.

- 1 GHz 16 bit multihit TDC

  The dynamic rage of the default setting is 60 μs, however it is much shorter than the beam interval of J-PARC, 40 ms. Therefore we implemented frequency divider and lengthen the dynamic range to 52 ms, which corresponds to 1.25MHz.

	65MHz 12bit FADC	1GHz multihit TDC
Number of FINESSE	16	1
Number of channel	8	32
clock	20 MHz	1.25 MHz
sampling point	10 bit	16 bit
data size	2 kbyte/ch	< 1 kbyte
Improvement	support for self-trigger	lengthen the dynamic range

Table 3.10: The specifications of the FADC and TDC.

Figure 3.19: A photograph of a beam monitor.
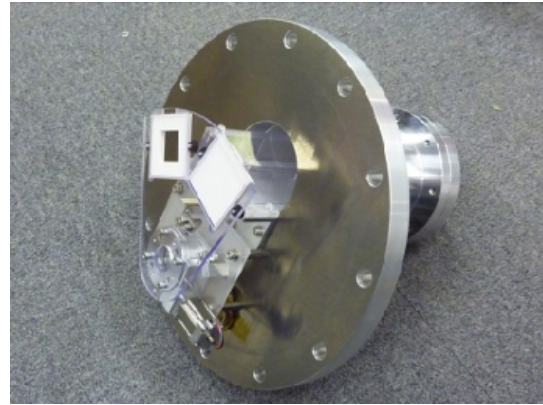
Figure 3.20: A photograph of a ^{6}Li shutter.

3.5 Beam monitor and ^{6}Li shutter

The neutrons captured in B_4C in the SFC generate γ rays. While almost all the γ rays are shielded by the surrounding lead, some of them emerge together with the neutron from the exit of the SFC and becomes the background of the TPC. The background is subtracted by use of a beam monitor and a ^{6}Li shutter located right downstream of the SFC. The pictures are shown in Figure 3.19 and 3.20.

The beam monitor (manufactured by Canberra Industries Inc., MNH10/4.2F) contains small quantities of ^{3}He. The specification is described in Table 3.11. The ^{6}Li shutter moves by a stepping motor inside a vacuum chamber, which has a ^{6}Li plate and an apertured ^{6}Li plate. The beam monitor can measure the relative neutron flux between two shutter conditions with an accuracy of 0.1% for 14 hours.

3.6 Shields for the environmental background

This section describes the designs of the shielding for the environmental radiation (B_e) which consist of the Pb shielding and cosmic-ray veto counter. Assuming 220

Gas	$Ar : CH_4$ = 130 kPa : 13 kPa
Active size	100 mm × 42 mm × 40 mm
Detection efficiency	10^{-5}
Count rate stability	± 0.005 on 72 hours
Background	1 cpm

Table 3.11: Specification detail of a beam monitor.

kW of beam power at J-PARC and 7% of duty factor of the SFC, the rate of the neutron decay is expected to be 0.089 cps (S_β). In order to compare this number with that of other background, it converted to the case of a continuos beam as

$$0.089 \times \frac{1}{0.07} \sim 1.3 \text{ cps.} \tag{3.2}$$

The rate of environmental background without shielding is measured as 123.7 cps at the experimental area in MLF and becomes 30.7 cps after the signal selection as described in Section 5.5. For achieving $S_\beta/B_e \sim 1$, the hits of the TPC due to the environmental radiation is reduced to 4% by the Pb shielding and the cosmic ray veto counter.

3.6.1   Pb shielding

The environmental γ rays mainly originate from ^{40}K (1461keV) and ^{208}Tl (2615keV) in the ground. ^{222}Rn exists in air, whose decay products are also γ-ray sources; ^{214}Pb (295keV, 352keV) and ^{214}Bi (609keV, 1765keV). Lead is used for the shielding of the environmental γ rays and is put into an iron case as shown in Figure 3.21. 10 cm thick lead shield is placed in 1 cm thick iron case for the upstream side. For the other sides the thickness of the lead shield is 5 cm. The iron shields a Pb-Kα X ray with a range of 70 keV to 90 keV due to the excitation and a β ray from ^{210}Bi (Q=1.16MeV) which is a daughter nucleus of ^{210}Pb. For 1461 keV γ ray from ^{40}K the penetrating efficiency is 2% according to a `Geant4` simulation.

Figure 3.23 shows the assembled structure. The aperture ratio is about 1% due to the two holes for the beam pipes. Figure 3.24 shows the performance of the shielding by using a 2-inch NaI detector. The environmental γ rays are suppressed by the shielding. Cosmic rays excite the iodine in NaI and cause a KX ray, thus it is vetoed by surrounding scintillators as described in the next section. As a result the shielding efficiency is evaluated to be 2.0% and is in good agreement with the expectation.

Figure 3.21: A photograph of the bottom of the front of the Pb shielding.
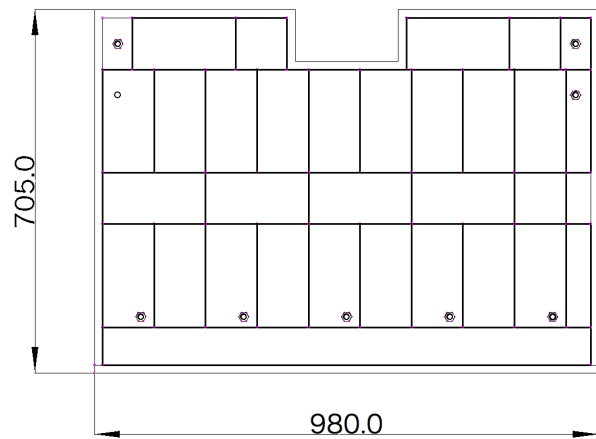
Figure 3.22: A drawing of the bottom of the front of the Pb shielding.

Figure 3.23: A photograph of the Pb shielding.
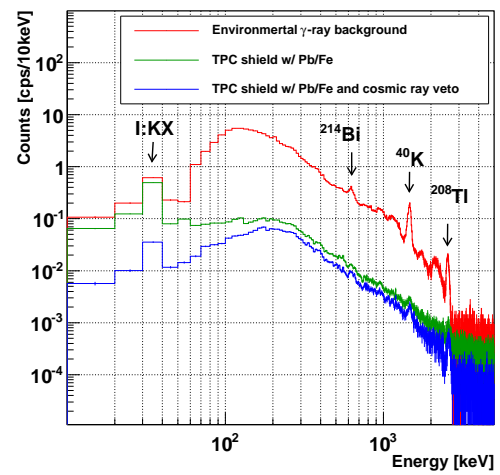
Figure 3.24: A performance of the Pb shielding.

Outer size	1120 mm (x) × 1326 mm (y)× 1656 mm (z)
Inner size	980 mm (x) × 1176 mm (y) × 1466 mm (z)
Aperture ratio	1%
Penetrating efficiency at 1461 keV γ ray	2%
NaI count rate w/o the shielding	119 cps
NaI count rate w the shielding	5.0 cps
NaI count rate w cosmic ray veto	2.3 cps

Table 3.12: Specification detail of the Pb shielding and summary of the performance by using NaI detector.

3.6.2   Cosmic-ray veto counter

Scintillators for the cosmic-ray veto surround the lead shielding as shown in Figure 3.27, Extruded scintillators for the Telescope Array experiment are used. A specification is shown in Table 3.13.

Company	C. I. Industry
Product name	CIMS-G2
Size	1500 mm × 250 mm × 12 mm
Material	MS-IM-62-01
Wavelength of maximum scintillation	420 nm
Scintillation efficiency	60% Anthracene
Decay time	3.0 ∼ 3.2 nsec
Light attenuation length	90 ∼ 110 cm
Refractive index	1.5 ∼ 1.58
Density	1.04 cm^3

Table 3.13: Specification detail of the cosmic ray counter.

The scintillator has grooves at 10 mm intervals and a wavelength shifter, the Y11 produced by Kuraray Co. Ltd. is installed. We use a tyvek sheet manufactured by DuPont Co. as a reflector and R329 manufactured by Hamamatsu Photonics K. K. for the photon detector. These selections are conformed to the Telescope Array experiment.

The efficiency for the cosmic ray is evaluated by cubic scintillators, about 10 cm on a side. While the maximum energy due to the environmental γ ray is less than 2.6 MeV, the cosmic ray can deposit more than 20 MeV in the cubic scintillators. Thus only the cosmic ray can be triggered by means of energy threshold. The efficiency map of each cosmic ray counter is taken and the minimum efficiency is measured to be 97.7%. In case of the assembled structure as shown in Figure 3.27, the efficiency is evaluated to be 95.9%. This value includes the inefficient region

due to the hall for the beam pipes.

Position	A [%]	B [%]	C [%]	D [%]	E [%]
Top	99.52 ± 0.06	99.57 ± 0.02	99.19 ± 0.04	99.73 ± 0.04	99.12 ± 0.04
Front	—	99.60 ± 0.02	98.83 ± 0.04	99.64 ± 0.04	—
Back	—	99.76 ± 0.02	98.92 ± 0.04	99.73 ± 0.04	—
Right	$100.00\_0.06$	99.65 ± 0.02	98.74 ± 0.04	99.73 ± 0.04	98.34 ± 0.04
Left	99.69 ± 0.06	99.46 ± 0.02	97.66 ± 0.04	99.82 ± 0.04	98.93 ± 0.04
Xback	98.58 ± 0.06	—	—	—	—
XFront	97.95 ± 0.06	—	—	—	—

Table 3.14: Detection efficiency of the cosmic ray veto counter at each position described in Figure 3.27.

3.7 Shields for the beam-induced background originated from the outside the TPC

This section describes shields for the beam-induced background originated from outside the TPC which consist of the SFC shielding and the Fe wall. A blue line in Figure 3.29 shows the TOF spectrum of the beam-induced background with the ^{6}Li shutter closed. and it is found that there are two component; the tail between 0∼5 ms and the bumps between 10∼40 ms.

The tail is derived from the fast neutron which is not stopped by the shielding at a distance of 12∼16 m from the moderator. The Polarization beam branch selects neutrons with one spin state for the SFC and the rest including fast neutrons are absorbed by the concrete shielding located upstream of the SFC. However all the neutrons and prompt γ rays are not shielded, so that they become the background to the neutron decay. In addition, BL04 which is constructed next to BL05 is also a background source for our experiment. For the shielding an L-Type iron wall 20 cm thick is set up as shown in Figure 3.29.

The bumps between 10∼40 ms are derived from the neutrons passing through the SFC. While the SFC shapes a desirable neutron bunch, some neutrons are captured on the supper mirror or scattered by the air. Consequently the structure of the bunches is clearly seen and the timing of the peaks corresponds to the time when the neutron bunch reflect on the third magnetic mirror from upstream. Thus the SFC is housed in the boron-lining lead box for the shielding as shown in Figure 3.7. A red line in Figure 3.29 shows the TOF spectrum after shielding. The beam-induced background is reduced to be 2 cps (B_b).
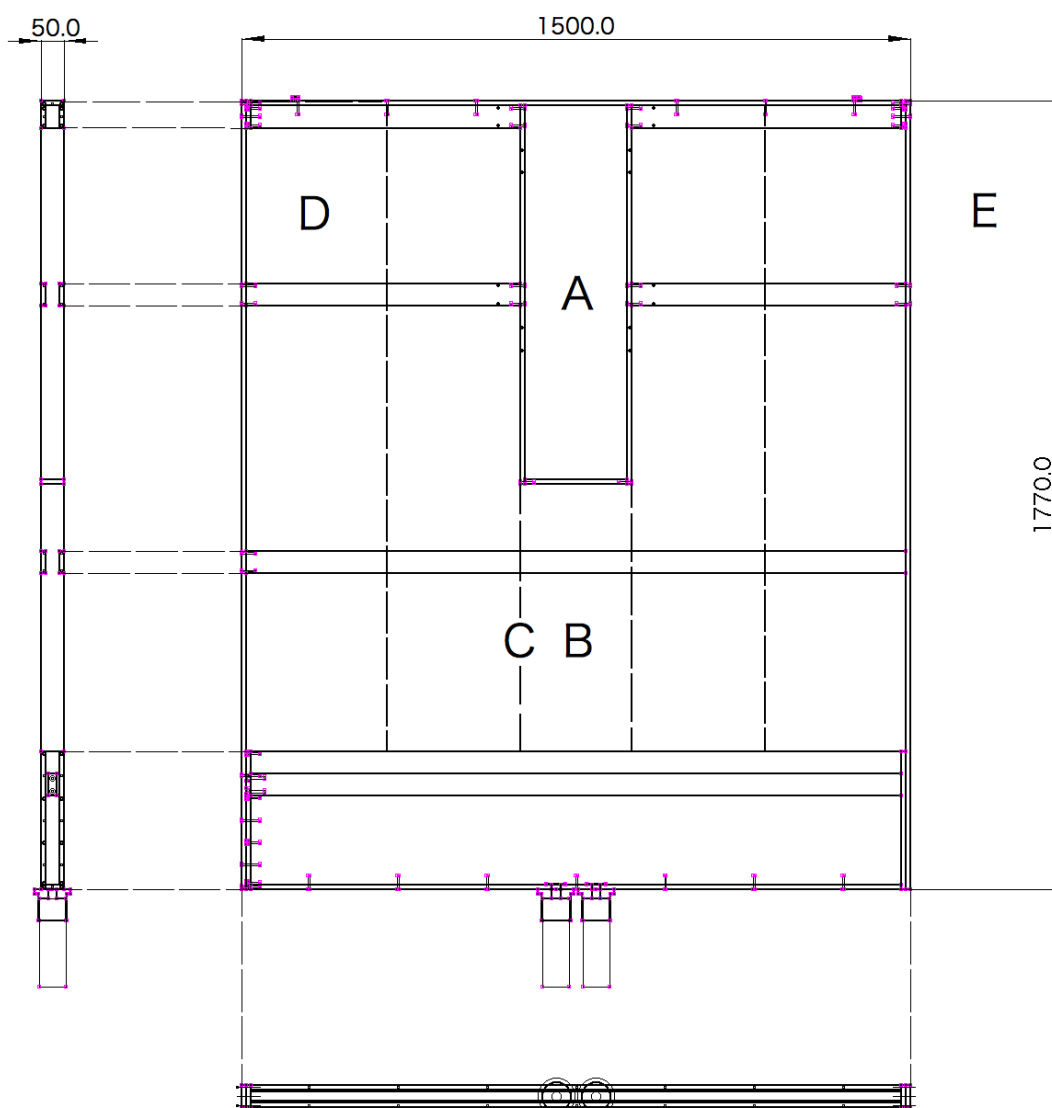
Figure 3.25: A drawing of the front of the cosmic-ray veto counter. Detection efficiencies at positions A, B, C, D, and E are summarized in Table 3.14. A measurement setup is shown in Figure 3.26.
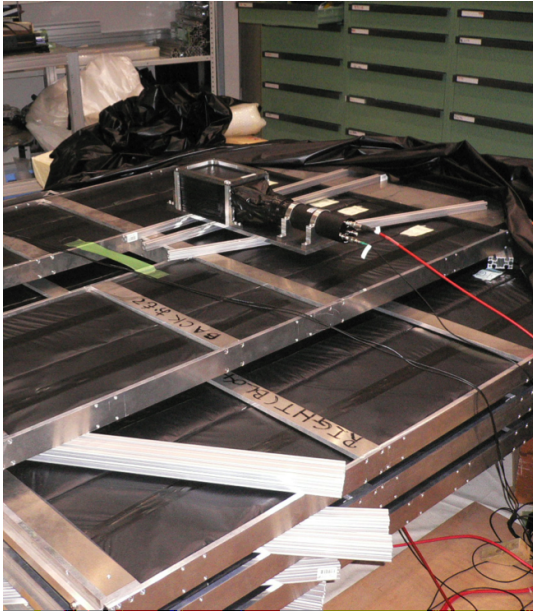
Figure 3.26: A setup for the measurement of detection efficiency of the cosmic-ray veto counters.

Figure 3.27: A photograph of the cosmic ray veto counters.
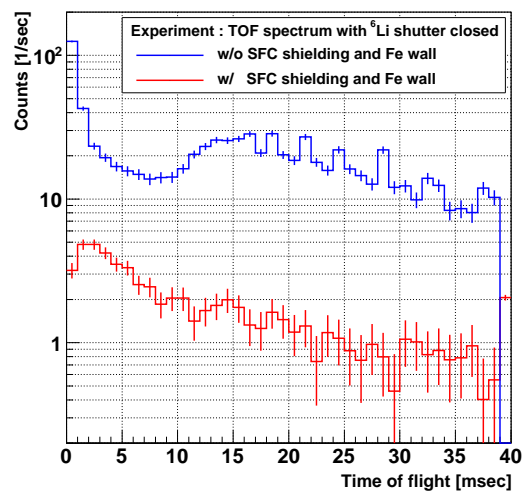
Figure 3.28: A TOF spectrum of the beam-induced background with no shielding (blue) and with SFC shielding and Fe wall (red) The neutron beam is chopped by the SFC and stopped by the ^{6}Li shutter.
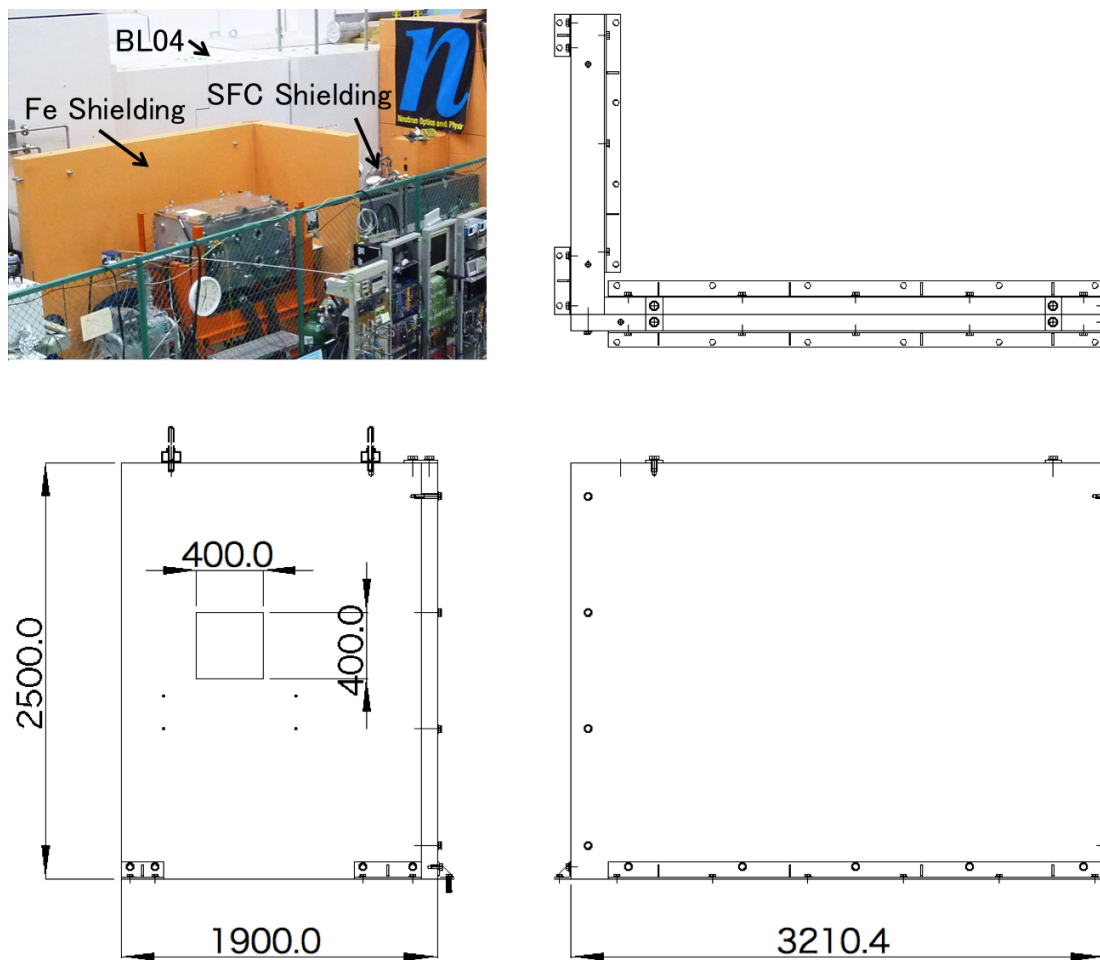
Figure 3.29: A drawing of the Fe shielding and SFC shielding.

Chapter 4

Simulation

This chapter describes the Monte Carlo (MC) simulation for the neutron decay, which includes the behavior of the particles and the response of the TPC. The simulation is applied to the neutron decay, the neutron capture in ^{3}He and various backgrounds as discussed in Chapter 5. The procedure of the simulation is as follows.

- Calculate the interaction of the particles using `GEANT4`

- Ionize atoms along the trajectory of the charged particle

- Drift the ionized electrons

- Cause the multiplication on the wire

- Process the signal

In particular, the interaction of the neutron and multiplication on the wire has been developed for this experiment, as described in Section 4.1 and Section 4.4, respectively.

4.1 Interaction of particles

The Monte Carlo (MC) simulation for the time projection chamber was coded using `GEANT4` release 9.2.p01. An example of MC simulation for the neutron decay is shown in Figure 4.1. The vacuum chamber, the lead shielding and cosmic veto counters are also implemented.

`GEANT4` has selectable physics model, however the behavior of the neutron is not fully reproduced. Thus the items as described as follows are independently developed for the experiment in this thesis.

- Angular correlation of the neutron decay

- Angle and energy of the scattered neutron

- Energy spectrum of the prompt γ ray due to the capture of the neutron

The components are described in 4.1.1, 4.1.2 and 4.1.3, respectively.

4.1.1   Decay of neutron
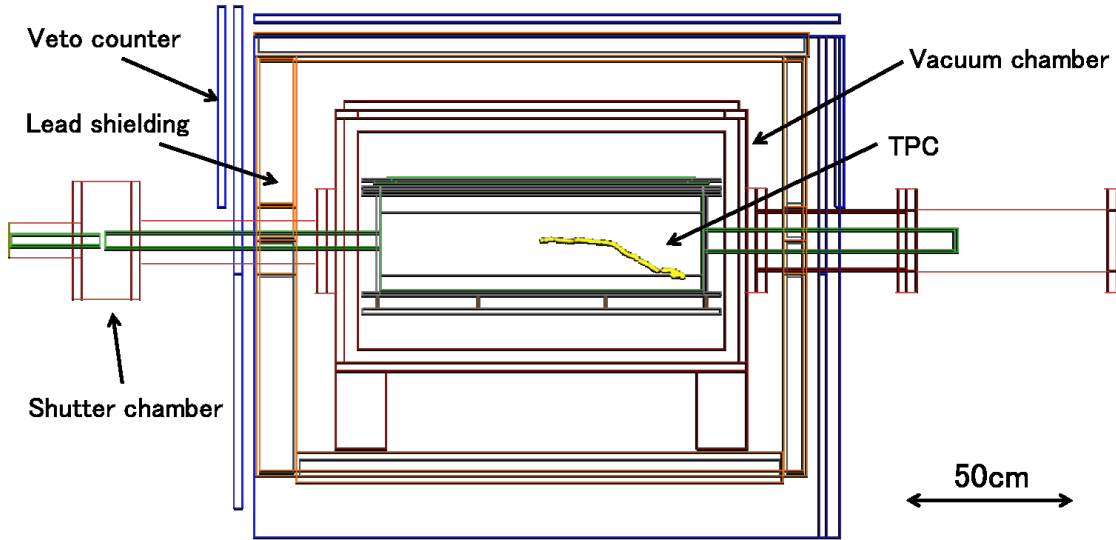
Figure 4.1: Implemented geometry on `GEANT4`. The yellow line represents the electron from the neutron decay inside the TPC. The electron moves from left to right.

The profile of the neutron beam is shown in Figure 4.2, in which the TPC is located from -480 mm to 480 mm. The divergence and attenuation of the beam are considered as described in Section 3.2.2. The attenuation length depends on the gas scattering and the velocity of the neutron, which is calculated in the Section 4.1.2. The neutron decay implemented in G4NeutronBetaDecayChannel.hh, emits the decay products incorrectly on the same plane. Thus the progr am is modified to model the three-body decay correctly.

4.1.2   Scattering of neutron

Scattering of the neutron with an energy less than 20 MeV is implemented in G4NeutronHPElastic.hh, which describes only the scattering by free atoms at a given temperature. However in the case of the molecular gas scattering, coherent scattering due to the structure of the molecule has to be considered [45, 46, 47]. The effects incorporated in the developed code is as follows.
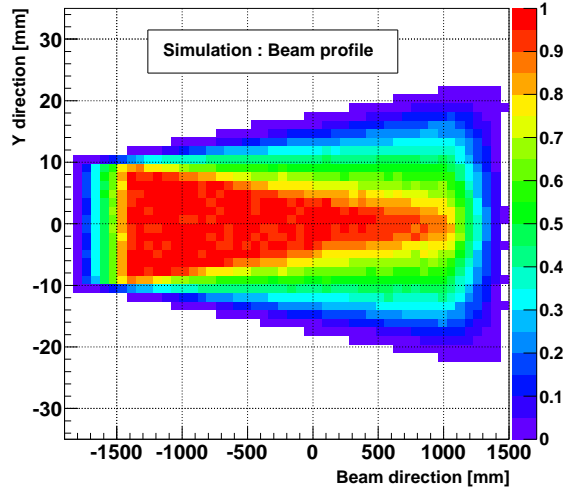
Figure 4.2: A simulated neutron distribution with scattering of gas on Y and Z axis.

- Coherent scattering from the atoms in the molecule
  The neutron with an energy less than 1 eV is assumed to be S-wave, and therefore the scattering of the neutron by a point-like nucleus at rest is spherically symmetric and independent of the velocity. The energy of the neutron provided in MLF/J-PARC corresponds to a wavelength of 0.2 nm $\sim$ 0.8 nm, which is comparable to the distance between C and O in the CO_2 ($\sim$ 0.1 nm). Thus the coherent scattering due to the structure of the molecule is significant. The calculation is performed by using the Semiclassical model based on the Born approximation developed by N. Z. Alcock *et al.* [48]. The cross section $\sigma(\theta, \phi)$ is described with $x_{ij} = \frac{4\pi r_{ij}}{\lambda} \sin(\frac{\theta}{2})$, where r_{ij} is the distance between atoms and λ is the wavelength of the neutron. The equation is obtained as follows.

$$\sigma(\theta, \phi) = -\frac{1}{4\pi} \left(\frac{M}{M+1}\right)^2 \sum_i \sum_j (\sigma_i \sigma_j)^{1/2} \frac{\sin x_{ij}}{x_{ij}}, \qquad (4.1)$$

  where $\sigma_i \sigma_j$ denotes the total scattering cross section in the case of $i = j$, otherwise it denotes the coherent scattering cross section. M represents the mass of the molecule in a unit of amu. $(M/M+1)^2$ indicates the transformation from the center of mass frame to the laboratory frame.

- Thermal motion of the gas molecule
  While the velocity of the neutron is $500 \sim 2000$ m/s, the average velocities of the He and CO_2 at room temperature are 1400 m/s and 400 m/s, respectively.

v_n and v_{gas} represent the velocities of the neutron and the gas so that the number of interaction is proportional to $1 - \frac{v_n \cdot v_{gas}}{v_n^2}$. Therefore the relative velocity, $v_{rel} = \sqrt{v_n^2 + v_{gas}^2}$, is expressed using the Boltzmann distribution as:

$$\bar{v}_{rel} = \int v_{rel} \times 4\pi v_{gas}^2 (\frac{m}{2\pi kT})^{3/2} \exp(\frac{-m v_{gas}^2}{2kT}) dv_{gas}. \tag{4.2}$$

From this equation, the contribution of the thermal motion can be calculated.

The developed code is confirmed to reproduce the scattering of the neutron with the velocity of 3700 m/sec in the preceding experiment as shown in Figure 4.3 [48] In the preceding experiment, CO_2 under 60 atm was employed so that the suppression can be seen in the small angle due to the screening effect. Figure 4.4 represents the velocity dependence of the scattering angle. As the incident neutron becomes slower, the forward scattering is enhanced in particular and the total cross section is increasing.

Thermal motion also has an influence on the velocity after the scattering, which has to be considered since the neutron capture cross section of the atom such as ^{3}He is inversely proportional to the velocity [35, 36]. Figure 4.5 shows the results of the neutron with the velocity of 400~2000 m/sec scattered by He, CO_2 and CH_4 at room temperature. These data are employed for the scattered neutron.

4.1.3   Capture of neutron

The capture of the neutron with an energy less than 20 MeV is implemented in G4NeutronHPCapture.hh and G4NeutronHPInelastic.hh. The cross section and its $1/v$ dependence is incorporated, however the decay products wrongly emit prompt γ rays. Thus the map of the capture position for the scattered neutron is recorded at first, and the correct products without γ rays are subsequently generated on the spot.

Figure 4.6 shows the map of the neutron capture in ^{3}He and ^{6}Li. The neutron is scattered from the beam axis discussed in Section 4.1.1. The velocity and angle of the neutron is calculated as described in Section 4.1.2. Figure 4.7 shows the energy spectrum of the prompt γ ray from the 95% ^{6}Li-enriched plate, which consists of LiF : PTFE = 30wt% : 70wt%. Each contribution is summarized in Table 4.1.

4.1.4   Energy loss of charged particles

Geant4 has selectable physics models based on different principles. For electromagnetic processes for e^- and γ in the low energy domain, Low-energy and Standard
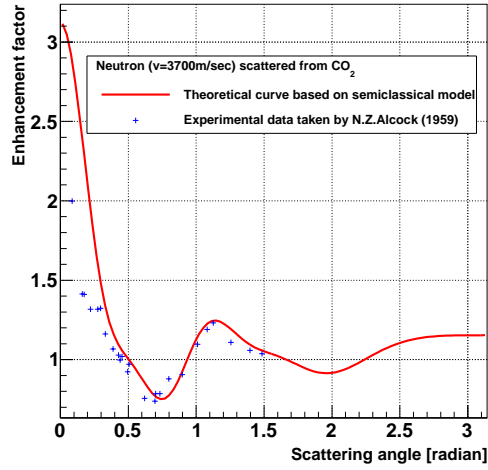
Figure 4.3: The angular distribution of the enhancement factor by an interference of CO_2 molecule. The crossed points are measured values by Alcock *et al.* , and the solid curve is the calculation by using the semi-classical model.
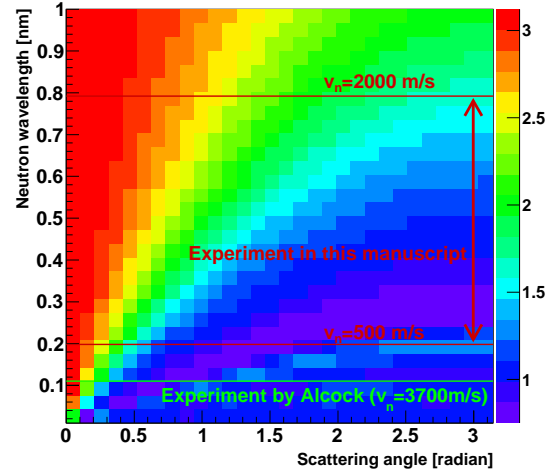
Figure 4.4: The enhancement factor dependence of the scattering angle and neutron wavelength. The green solid line describes the wavelength which Alcock *et al.* was used for their measurement.

	cross section	mole fraction	branching ratio	average number of γ ray
^{6}Li	39 mbarn	0.173	4.1×10^{-5}	1.41
^{7}Li	45 mbarn	0.009	2.5×10^{-6}	1.03
C	3.5 mbarn	0.212	4.5×10^{-6}	1.16
F	39 mbarn	0.606	3.5×10^{-5}	2.78

Table 4.1: Properties of the prompt γ rays from the ^{6}Li plate.

packages are prepared. Low-energy package consists of two different approaches, which are Library-based (Livermore) models and Penelope-like models. Livermore models are based on publicly available evaluated data tables including elements from $Z = 1$ to $Z = 100$ with a validity range of 250 eV $\sim$ 100 GeV. On the other hand, Penelope is a Monte-Carlo code, which directly calculates atomic effects as florescence x ray. The validity range is also 250 eV $\sim$ 100GeV.

The comparison between two packages in release 9.1 are investigated in terms of energy deposition in homogeneous targets [49]. According to this work, the accuracy achieved by simulations involving Library-based processes is comparable to, or better than, the one resulting from Penelope processes. Thus the work in this thesis adapt the Livermore package as below.
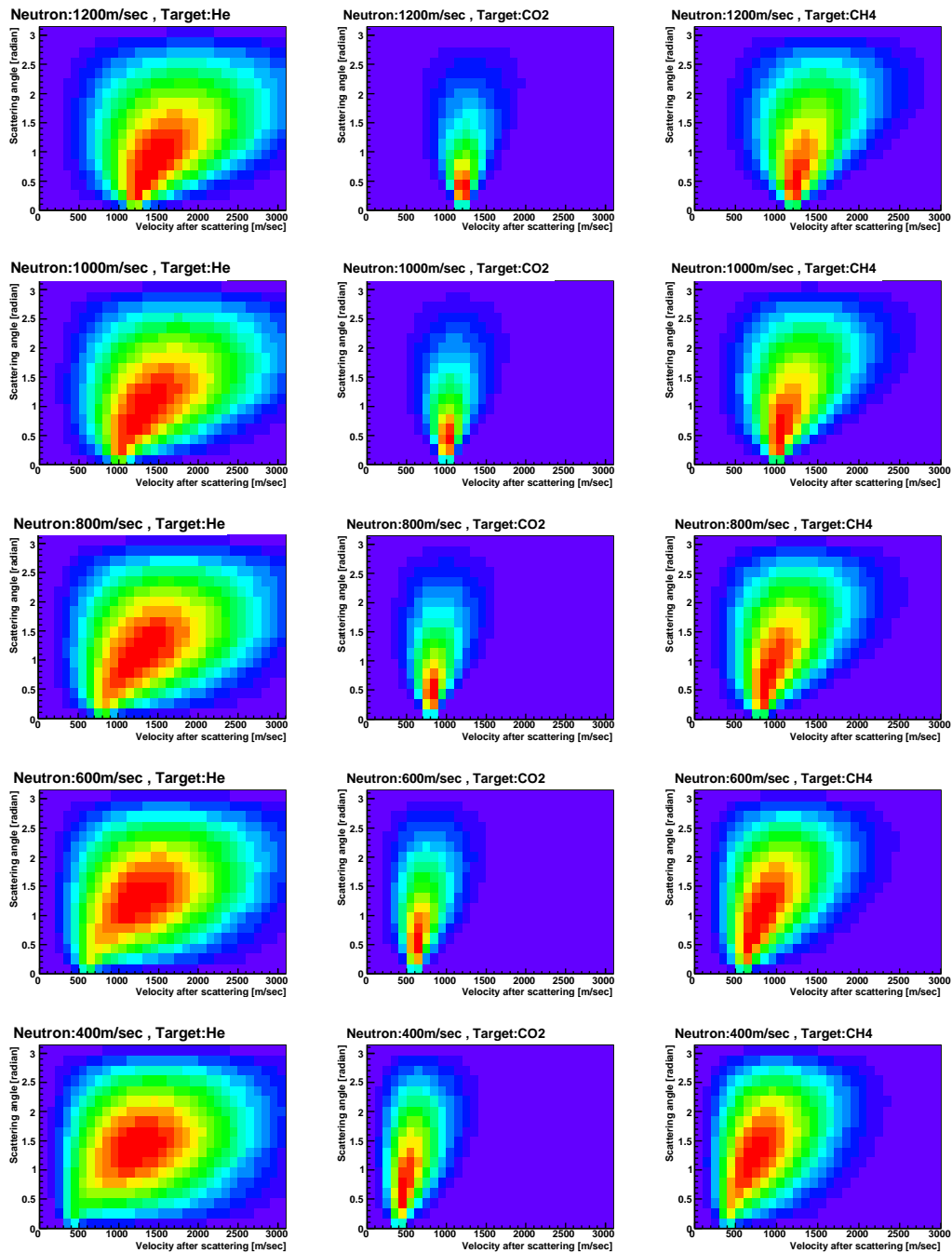
Figure 4.5: Differential scattering cross sections with scattering angle and velocity after scattering for 3 gases (He, CO_2, and CH_4) and 5 different initial velocities.
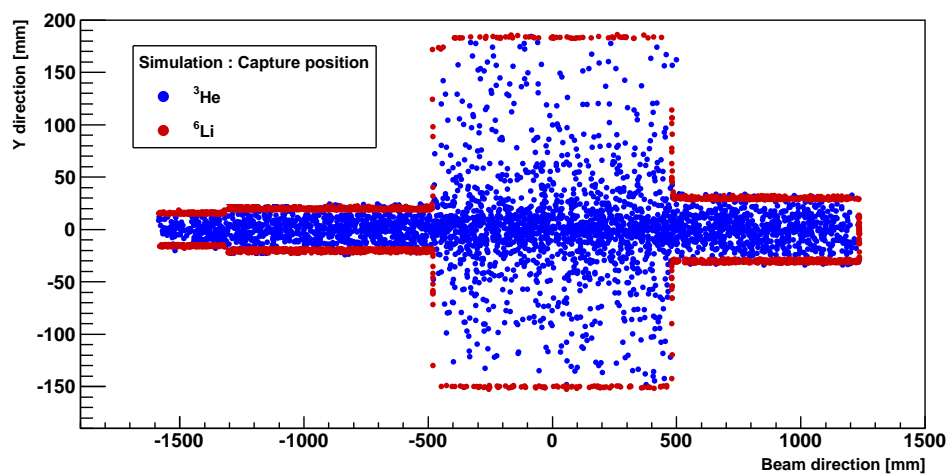
Figure 4.6: A scatter plot of positions of the neutron capture calculated by the simulation taking account of the gas scattering.
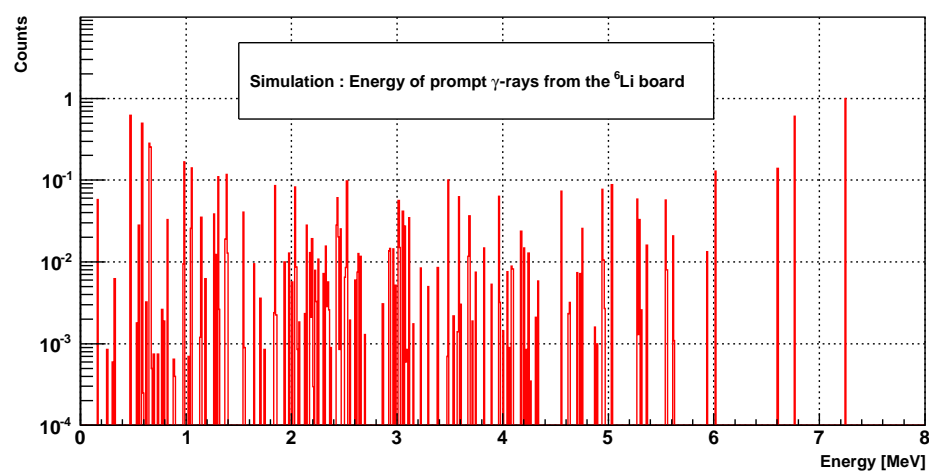
Figure 4.7: The prompt γ ray spectrum generated by neutron capture of ^{6}Li.

From	Low energy EM process	Particle
	G4LowEnergyIonization	e^-
	G4LowEnergyBremsstrahlung	e^-
Livermore	G4LowEnergyPhotoelectric	γ
	G4LowEnergyCompton	γ
	G4LowEnergyGammaConversion	γ
	G4LowEnergyRayleigh	γ
	G4hLowEnergyIonisation	hadrons

Table 4.2: Libraries used in this simulation code.

4.2   Ionization

A charged particle that traverses the gas leaves a track of ionization along its trajectory. The total amount of ionization is characterized by the energy W that is spent, on the average, on the creation of one free electron. The energy W depends on the gas mixture so that many measurements of W have been performed. As shown in Figure 4.8 and 4.9, W values depend on the incident particle and its energy at low energy, while they become constant for electrons with an energy of more than 1 keV and protons with an energy of more than 10 keV, which are summarized in Table 4.3.

	W_α [eV]	W_β [eV]	I [eV]
He	46.0	42.3	24.58
CO_2	34.3	32.8	13.81

Table 4.3: Average energy W spent for the creation of one ionization electron. W_α and W_β are from measurement using α or β sources, respectively. The minimum ionization potential is also indicated.

Ionization process consists of two steps and the energy W is the inclusive value. At first, an incident charged particle ionizes atoms and the second step is caused by electrons which are ejected from the first ionization. Since `GEANT4` also simulates also secondary electrons, the distribution of ionization electron can be obtained by using Poisson statistics.

4.3   Drift and diffusion

The ionization electrons drift in the electric field as they are diffused by the gas molecules. The drift part of the TPC is designed to make a uniform electric field
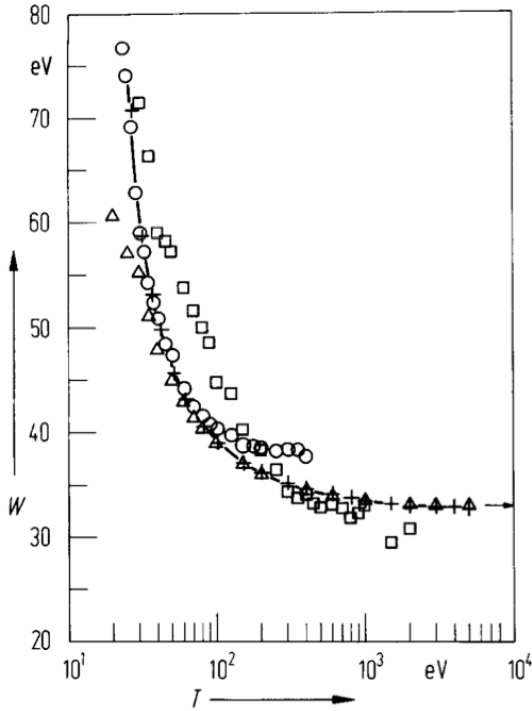
Figure 4.8: W value of CO_2 for the electron as a incident particle [50].
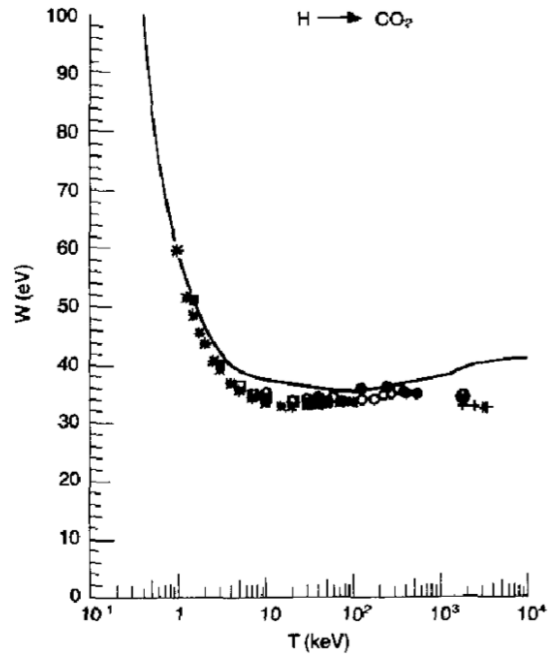
Figure 4.9: W value of CO_2 for the proton as a incident particle [51].

and it is confirmed that the variation of drift velocity is within 1%. The diffusion width is measured to be less than 1mm. Thus in this simulation the drift velocity is treated as uniform and the diffusion is neglected.

4.4 Multiplication

The multiplication on the wire is formulated by H. Oide [52], which takes into account the space-charge effect. As an ionized electron drifts towards the anode wire, it travels in an increasing electric field, which causes avalanche multiplication. A gain factor G is exponentially increasing with the anode voltage V as shown in Figure 6.22. Since V has a linear relationship with electric field on the wire $E(r_0)$ where r_0 is a radius of the wires, $G \propto \exp(E(r_0))$ can be obtained.

G depends on the number of electrons collected on the wire, which are created by the incident charged particle. Let us call G_i the gain factor for the i-th electron arriving at the wire, so that $G_i \propto \exp(E_i(r_0))$ can be assumed, where $E_i(r_0)$ denotes the electric field $E(r_0)$ at the time of i-th avalanche multiplication.

The TPC detects the neutron decay and the neutron capture in ^{3}He. In the former case the multiplied signal is proportional to the number of electrons collected.

However, in the latter case, the number of the initial ionized electrons is so much that the created ions during the avalanche multiplication induce a space-charge effect around the wire, which causes a saturation of the multiplied signal.

Since a mobility of the ions are smaller than that of the electron by three orders of magnitude, the ions can be considered not to move during the whole multiplication. Assuming the electric field decreases proportionally with the created ions, $E_i(r_0)$ is calculated as

$$E_i(r_0) = E_0(r_0) - \alpha \sum_{j=0}^{i-1} G_j, \tag{4.3}$$

where α is a constant determined by the angle θ between the anode wire and a direction of the incident charge particle. By using the relationship $G_i \propto \exp(E_i(r_0))$,

$$\frac{G_{i+1}}{G_i} = \exp(E_{i+1}(r_0) - E_i(r_0)) = \exp(-\alpha G_i) \tag{4.4}$$

can be introduced. Using $\alpha G_i \ll 1$,

$$G_i \simeq \frac{G_0}{1 + i\alpha G_0} \tag{4.5}$$

is a good approximation. Inserting it into Eq (4.4), both sides of the equation are equivalent at a level of $O(\alpha)$. Assuming the number of the collected electrons is n, the effect of the saturation $s(\theta)$ can be computed as the accumulation of each multiplication:

$$s(\theta) \equiv \frac{1}{nG_0} \sum_{i=0}^{n-1} G_i = \frac{\ln(1 + n\alpha G_0)}{n\alpha G_0}. \tag{4.6}$$

Figure 4.10 shows a setup using 5.5-MeV α rays emitted from the ^{241}Am to measure the saturation effect. The energy deposit (ΔE) varies across the wires and the results are summarized in Fig 4.11. The saturation effect increases with the angle because the multiplication region is localized and with the deposit energy because the multiplied ions are accumulated. From this measurement, $n\alpha$ can be obtained as

$$n\alpha = \frac{a\Delta E}{1 + b\tan^{-1}\theta}$$
$$\begin{cases} a = (1.39 \pm 0.06) \times 10^{-3} \\ b = 2.5 \pm 0.4, \end{cases}$$

where a and b are constants. In the MC simulation, the saturation effect is implemented by using this formula and the position dependence is also considered.
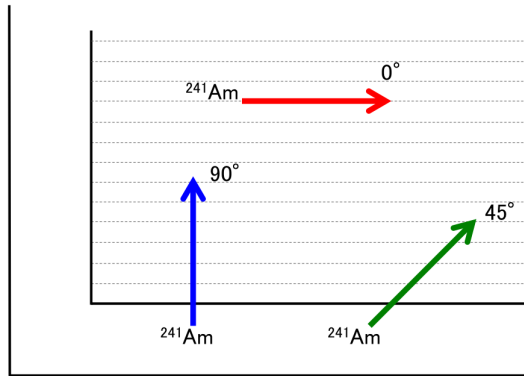
Figure 4.10: A schematic view of the measurement of the saturation effect by using 5.5-MeV α rays emitted from the ^{241}Am. Anode wires are shown in dotted lines.
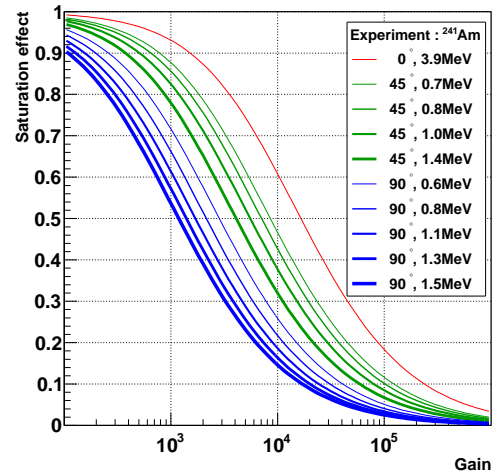
Figure 4.11: Evaluated curves for the saturation effect obtained by fitting the measured value.

4.5 Signal processing

As described in Section 3.4.2, the collected charge on the wire is converted to the voltage signal by a charge sensitive preamplifier. Then all the waveforms are recorded via FADCs on Copper-Lite.

Figure 4.12 (top) shows the event display of the MC simulation. The data format is same as the experimental data, which is also described in Figure 4.12 (bottom).
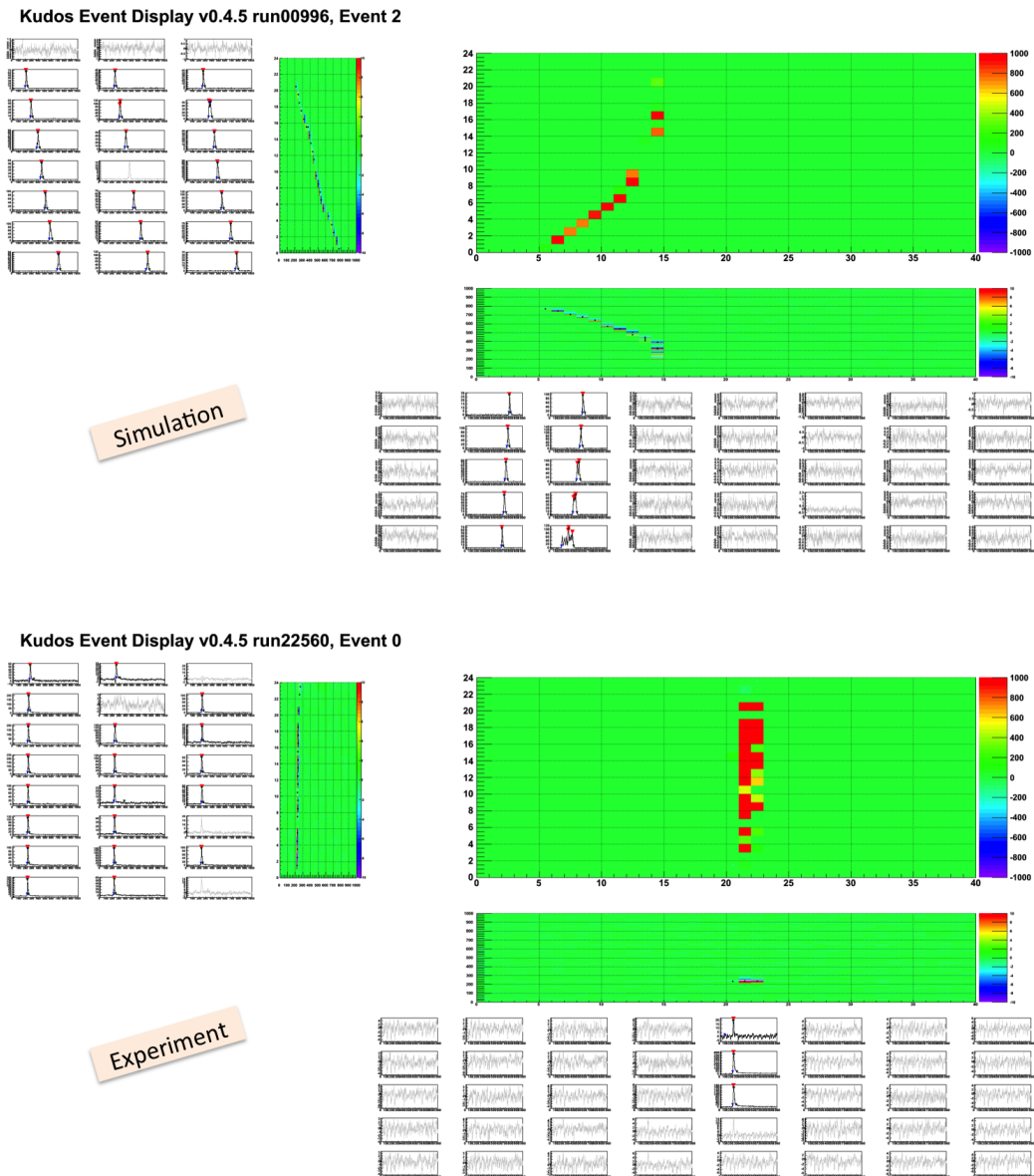
Figure 4.12: Views of the event display drawing a track event made by the simulation (top) and obtained by TPC (bottom).

	Conc.	σ_s(barn)	$\sigma_{2\text{body}}$(barn)	$E_{2\text{body}}$(keV)	σ_γ(barn)	E_γ(MeV)	E_{recoil}(keV)	τ_n
H	—	82.02	0	—	0.3326	—	—	—
^{1}H	99.985	82.03	0	—	0.3326	2.22	1.32	—
^{2}H	0.015	7.64	0	—	0.000519	6.25	6.96	12.32a
He	—	1.34		—	0.00747	—	—	—
^{3}He	0.00014	6	5333.(7.)	764	—	—	—	—
^{4}He	99.99986	1.34	0	—	0	—	—	—
Li	—	1.37		—	70.5	—	—	—
^{6}Li	7.5	0.97	940.(4.)	4783	0.039	—	—	840ms
^{7}Li	92.5	1.4	0	—	0.0454	—	—	—
B	—	5.24	0	—	767.(8.)	—	—	—
^{10}B	20	3.1	0	—	3835.(9.)	—	—	—
^{11}B	80	5.77	0	—	0.0055	—	—	20.2ms
C	—	5.551	0	—	0.0035	—	—	—
^{12}C	98.9	5.559	0	—	0.00353	4.95	1.01	—
^{13}C	1.1	4.84	0	—	0.00137	8.17	2.56	5.7×10^3year
N		11.51		—	—	—	—	—
^{14}N	99.63	11.53	1.83	626	0.0798	10.8	4.20	—
^{15}N	0.37	5.21	0	—	0.000024	8.87	—	7.1sec
O	—	4.232	0	—	0.00019	—	—	—
^{16}O	99.762	4.232	0	—	0.0001	3.27	0.339	—
^{17}O	0.038	4.2	0	—	0.236	4.37	0.570	—
^{18}O	0.2	4.29	0	—	0.00016	4.18	delay	26.5sec
F	100	4.018	0	—	0.0096			11.2sec

Table 4.4: Table of the parameters related with the neutron capture or scattering.

	Conc.	σ_s(barn)	σ_{2body}(barn)	E_{2body}(keV)	σ_γ(barn)	E_γ(MeV)	E_{recoil}(keV)	τ_n
Al	100	1.503	—	—	0.231	—	—	2.24sec
Cr	—	3.49	—	—	3.05	—	—	—
^{50}Cr	4.35	2.54	—	—	15.8	—	—	27.7day
^{52}Cr	83.79	3.042	—	—	0.76	—	—	—
^{53}Cr	9.5	8.15	—	—	18.1(1.5)	—	—	—
^{54}Cr	2.36	2.6	—	—	0.36	—	—	3.50min
Fe	—	11.62	—	—	2.56	—	—	—
^{54}Fe	5.8	2.2	—	—	2.25	—	—	2.74a
^{56}Fe	91.7	12.42	—	—	2.59	—	—	—
^{57}Fe	2.2	1	—	—	2.48	—	—	—
^{58}Fe	0.3	28.(26.)	—	—	1.28	—	—	44.5day
Ni	—	18.5	—	—	4.49	—	—	7.6×10^4a
^{58}Ni	68.27	26.1	—	—	4.6	—	—	—
^{60}Ni	26.1	0.99	—	—	2.9	—	—	—
^{61}Ni	1.13	9.2	—	—	2.5	—	—	—
^{62}Ni	3.59	9.5	—	—	14.5	—	—	100.1a
^{64}Ni	0.91	0.017	—	—	1.52	—	—	2.52hour
Zr	—	6.46	—	—	0.185	—	—	—
^{90}Zr	51.45	5.1	—	—	0.011	—	—	—
^{91}Zr	11.32	9.7	—	—	1.17	—	—	—
^{92}Zr	17.19	6.9	—	—	0.22	—	—	1.53×10^6a
^{94}Zr	17.28	8.4	—	—	0.0499	—	—	64.0day
^{96}Zr	2.76	3.8	—	—	0.0229	—	—	16.7hour

Table 4.5: Table of the parameters related with the neutron capture or scattering.

Chapter 5

Analysis algorithm for the measurement of the neutron lifetime

In this chapter, a newly developed analysis algorithm for the measurement of the neutron lifetime is discussed. The experiment in this thesis classifies the backgrounds according to the physics processes and evaluates them quantitively. Then

- 99.9% detection efficiency by use of calorimetric approach,

- subtraction of the background by using data-driven approach,

have been developed.

5.1 Overview of the analysis algorithm

For the measurement of the neutron decay, the counts of the neutron decay (S_β) and the neutron capture in ^{3}He (S_n) have to be extracted from the analyzed data. In Table 5.1, a developed analysis algorithm is described. Assuming the data taking under 100 kPa with a ^{3}He pressure of 0.1 Pa ($N^{100\text{kPa}/0.1\text{Pa}}$), it includes various backgrounds. The backgrounds are categorized according to methods of the subtraction as described in Section 5.3: B_β^{energy}, B_β^{n}, B_β^{tof}, B_β^{gas}, B_n^{energy}, B_n^{tof} and B_n^{gas}.

In this algorithm, three other conditions of the filling gas are employed as shown in Table 5.2. $N^{100\text{kPa}/1.0\text{Pa}}$ is a ^{3}He-enriched measurement with a ^{3}He pressure of 1.0 Pa. $N^{50\text{kPa}/0.1\text{Pa}}$ and $N^{50\text{kPa}/1.0\text{Pa}}$ are taken under reduced pressures, 50 kPa.

In the first step, S_β, S_n and B_β^{energy} are discriminated by using a calorimetric approach with more than 99.9% detection efficiency for both reactions as described

Approach	Data ($N^{100\text{kPa}/0.1\text{Pa}}$)	
	$N^{100\text{kPa}/0.1\text{Pa}} = S_\beta + B_\beta^{\text{energy}} + B_\beta^{\text{n}} + B_\beta^{\text{tof}} + B_\beta^{\text{gas}} + S_n + B_n^{\text{tof}} + B_n^{\text{gas}}$	
calorimetry	$\downarrow$	$\downarrow$
	$N_\beta^{100\text{kPa}/0.1\text{Pa}} = S_\beta + B_\beta^{\text{n}} + B_\beta^{\text{tof}} + B_\beta^{\text{gas}}$	$N_n^{100\text{kPa}} = S_n + B_n^{\text{tof}} + B_n^{\text{gas}}$
Signal selection	$\downarrow$	$\downarrow$
	$N_\beta'^{100\text{kPa}/0.1\text{Pa}} = S_\beta' + B_\beta'^{\text{n}} + B_\beta'^{\text{tof}} + B_\beta'^{\text{gas}}$	$N_n'^{100\text{kPa}} = S_n' + B_n'^{\text{tof}} + B_n'^{\text{gas}}$
^{3}He-enriched measurement ($N^{100\text{kPa}/1.0\text{Pa}}$)	$\downarrow$ $\downarrow$ $\downarrow$	$\downarrow$ $\downarrow$ $\downarrow$ $\downarrow$ $\downarrow$ $\downarrow$
	$N_{\beta'}'^{100\text{kPa}} = S_\beta' + B_\beta'^{\text{tof}} + B_\beta'^{\text{gas}}$	
TOF spectra	$\downarrow$	$\downarrow$
	$N_{\beta''}'^{100\text{kPa}} = S_\beta' + B_\beta'^{\text{gas}}$	$N_{n''}'^{100\text{kPa}} = S_n' + B_n'^{\text{gas}}$
reduced-pressure measurement ($N^{50\text{kPa}/0.1\text{Pa}}$, $N^{50\text{kPa}/1.0\text{Pa}}$)	$\downarrow$ $\downarrow$ $\downarrow$	$\downarrow$ $\downarrow$ $\downarrow$
	S_β'	S_n'

Table 5.1: Analysis algorithm for the neutron lifetime.

in Section 5.4. In the second step, the signal selections are applied for the reduction of the background as described in Section 5.5. An influence on the detection efficiency of the TPC under the reduced pressure is also discussed. The resulting candidate of the neutron decay includes the background due to the neutron capture in ^{3}He ($B_\beta'^{\text{n}}$). An amount of $B_\beta'^{\text{n}}$ depends on the pressure of ^{3}He and is evaluated by ^{3}He-enriched measurement ($N^{100\text{kPa},1\text{Pa}}$) in the third step, which is described in Section 5.6. In the fourth step, the backgrounds due to radioactivation, environmental radiation and prompt γ ray originated from outside the TPC (B_β^{tof}, B_n^{tof}) are subtracted by using TOF spectrum as described in Section 5.7. Finally, the remaining backgrounds depends on the total pressure of the gas ($B_\beta'^{\text{gas}}$, $B_n'^{\text{gas}}$), so that the reduced-pressure measurements ($N^{50\text{kPa},0.1\text{Pa}}$, $N^{50\text{kPa},1\text{Pa}}$) are employed as described in Section 5.8.

Consequently S_β' and S_n' are extracted from the analyzed data with more than 99.9% detection efficiencies for both reactions and the neutron lifetime is calculated

	^{4}He	CO_2	^{3}He
$N^{100\text{kPa}/0.1\text{Pa}}$	85 kPa	15 kPa	0.1 Pa
$N^{100\text{kPa}/1.0\text{Pa}}$	85 kPa	15 kPa	1.0 Pa
$N^{50\text{kPa}/0.1\text{Pa}}$	42.5 kPa	7.5 kPa	0.1 Pa
$N^{50\text{kPa}/1.0\text{Pa}}$	42.5 kPa	7.5 kPa	1.0 Pa

Table 5.2: Measurements under various gas pressure for the subtraction of the background by using data-driven approach.

as

$$\tau_n = \frac{1}{\rho_{^3\text{He}}\sigma_0 v_0} \left(\frac{S'_n/\epsilon_n}{S'_\beta/\epsilon_\beta} \right), \tag{5.1}$$

which is discussed in Section 2.4.

5.2 Signal of the neutron decay

If the SFC is not active, all the neutrons are reflected on the supper mirror and go into the TPC, which yields 1.2×10^6 neutron/s with a power of 220 kW. Figure 5.1 and Table 5.3 show the condition of the SFC which enables to maximize the rate of neutron decay. In the following, the fiducial volume with a length of 800 mm are assumed. The length of the bunch corresponds to a half of the fiducial volume (400 mm). The interval between the bunches are set to be equal to the distance between the window and the beam dump (2826 mm). On this condition, 13.9% of the neutrons pass the TPC and the sum of the fiducial time per cycle t_1 corresponds to 2.8 ms. Consequently the rate of the neutron decay becomes $1.2 \times 10^6 \times 7.3 \times 10^{-8} = 8.9 \times 10^{-2}$ decay/s. A subset of the time when the neutron does not exist inside the TPC, t_0, is set to be 6 ms as shown in Figure 5.1, which is used for the subtraction by use of the TOF spectrum.

5.3 Backgrounds

Backgrounds to the neutron decay are divided into four categories: B_β^{energy}, B_β^{n}, B_β^{tof} and B_β^{gas}. Backgrounds to the neutron capture in ^{3}He are divided into three categories: B_n^{energy}, B_n^{tof} and B_n^{gas}.

In the following, 400-mm bunches with a velocity of 1000 m/s inside the 2826-mm vacuum chamber. which corresponds to 400 μs of the fiducial time. The ratio of the event in the fiducial time is calculated as 400mm/2826mm = 0.14.
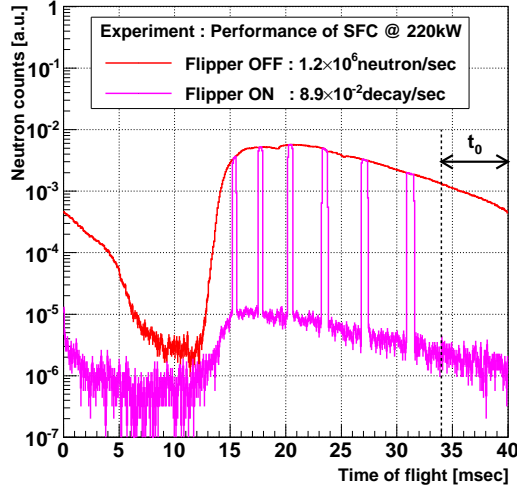
Figure 5.1: TOF spectrum assuming 6 of 400 mm-bunches per 1 pulse and 2826 mm of the interval of bunches. 2826 mm corresponds to the distance between the window of the vacuum chamber and the beam dump.

Velocity [m/sec]	Neutron ratio[10^{-2}]	Fiducial time [ms/cycle]	Decay ratio[10^{-8}]
1250	1.4	0.32	0.50
1085	2.4	0.36	0.98
941	3.1	0.42	1.5
816	3.0	0.49	1.7
708	2.3	0.56	1.4
615	1.6	0.65	1.2
total	13.9	2.8 ($\equiv t_1$)	7.3

Table 5.3: Neutron decay ratio inside the 800mm of the fiducial volume assuming 6 of 400 mm-bunches per 1 pulse and 2826 mm of the interval of bunches.

5.3.1   Backgrounds to the beta decay

Backgrounds are categorized according to methods of the subtraction. $B_\beta^{\mathrm{energy}}$ (B_0) can be discriminated by the calorimetric approach. B_β^{n} (B_1) can be subtracted by using measurements under different pressure of ^{3}He. B_β^{tof} can be subtracted by using TOF spectrum and consists of $B_2 \sim B_5$. B_β^{gas} is subtracted by using measurements under reduced pressures and consists of $B_6 \sim B_8$.

- S_β

  The neutron with a lifetime of 881.5 s decays at a rate of 1.1×10^{-6} per meter and 4.3×10^{-7} of the neutrons decays in the fiducial time. In the TOF spectrum, the detected neutron decay increases as the bunch comes in

the TPC and becomes constant while the bunch is fully inside the fiducial volume. It then decreases as the bunch gets out of the TPC. A schematic TOF spectrum is shown in Figure 5.20.

- B_β^{energy}

  - B_0 : Recoiled nucleus due to prompt γ rays
    The neutron is captured in CO_2 inside the TPC with a probability of 3.4×10^{-6} per meter and prompt γ rays are emitted, which recoils the nucleus with an energy of 1 keV.

- B_β^{n}

  - B_1 : Off-axis neutron capture in ^{3}He
    The neutron is scattered by He and CO_2 inside the TPC with a probability of 3.3×10^{-2} per meter. Some scattered neutron are captured in ^{3}He on the way to the ^{6}Li plates. In particular, the neutron captured in ^{3}He near the ^{6}Li plates becomes background to the neutron decay, since decay product, a proton or a triton, goes into the ^{6}Li plates and deposit only a portion of Q-value in side the TPC.

- B_β^{tof}

  - B_2 : Prompt γ rays outside the TPC
    On the Polarization beam branch in the BL05/MLF, only the cold neutron can be transferred by the supper mirror at a distance of 7.2$\sim$12 m from the target. The rest is captured in the iron and concrete shielding at a distance of 12$\sim$16 m from the target and emit prompt γ rays, which causes the spectrum to decrease exponentially with time. As shown in Figure 3.28, the rate of B_2 between 15$\sim$34 ms is 1.0 cps; the rate of B_2 between 34$\sim$40 ms is 0.8 cps.

  - B_3 : Radioactivation inside the TPC
    Radioactive atoms generated by the neutron capture and their decay products become the background to the neutron decay. In the ^{6}Li plate, ^{20}F ($\tau = 11.2$s) is the most dominant component following by ^{8}Li ($\tau = 840$ms). Both have lifetime longer than the beam interval of 40 ms, thus the time structure of this background is almost flat.

  - B_4 : Radioactivation outside the TPC
    Outside the TPC, Pb and Fe in the shields and Si in the supper mirror

are radioactivated. Their lifetime is also longer than 40 ms, thus the time structure is almost flat.

- B_5 : Environmental radiation

  Environmental radiation consists of naturally-occurring radioisotopes, cosmic rays and radioisotopes inside the TPC itself, whose time structure is flat. In this section, the rate of the environmental radiation is assumed as 1.4 cps, which can be obtained in Section 6.3.

- B_β^{gas}

  - B_6 : Prompt γ rays from ^{6}Li plate

    The neutron is scattered by He and CO_2 inside the TPC with a probability of 3.3×10^{-2} per meter and captured in the ^{6}Li plates. The branching fraction to prompt γ rays is about 8.3×10^{-4} and an average number of the prompt γ rays is 2.0. A Compton electron due to prompt γ rays reaches the TPC with a probability of 9.5×10^{-3}, which results in the background in the fiducial time with a rate of 2.0×10^{-8} per neutron. The time structure is the same as that of the neutron decay signal.

  - B_7 : Prompt γ rays from CO_2

    The neutron is captured in CO_2 inside the TPC with a probability of 3.4×10^{-6} per meter, which emit 1.5 of the prompt γ rays on an average. A Compton electron due to prompt γ rays reaches the TPC with a probability of 1.5×10^{-3}, which results in the background in the fiducial time with a rate of 3.0×10^{-9} per neutron. The time structure is the same as that of the neutron decay signal.

  - B_8 : Off-axis neutron decay

    Some scattered neutron decay in its flight on the way to ^{6}Li plates with a probability of 2.2×10^{-7}. which results in the background in the fiducial time with a rate of 3.3×10^{-9} per neutron. The time structure is the same as that of the neutron decay signal.

The event probability of each signal in the fiducial time is described in Table 5.4. Not all process is applicable and the relevant factor are listed. P_s is the scattering probability per meter, P_γ is the emission probability of the prompt γ ray, N_γ is the average number of the prompt γ ray, P_β is the emission probability of β ray including the neutron decay, P_{time} is the ratio of the event in the fiducial time and P_{TPC} is the hit probability of the TPC in the fiducial time.

	L	P_s	P_γ	N_γ	P_β	P_{time}	P_{TPC}
S_β	2.82	—	—	—	1.1×10^{-6}	0.14	4.3×10^{-7}
B_0	2.82	—	3.4×10^{-6}	—	—	0.14	1.3×10^{-8}
B_1	2.82	3.3×10^{-2}	—	—	2.2×10^{-7}	0.14	3.3×10^{-9}
B_2	—	—	—	—	—	—	—
B_3	2.82	3.3×10^{-2}	—	—	6.5×10^{-6}	0.01	2.1×10^{-9}
B_4	—	—	—	—	5.0×10^{-10}	0.01	5.0×10^{-12}
B_5	—	—	—	—	—	—	—
B_6	2.82	3.3×10^{-2}	8.3×10^{-5}	2.0	9.5×10^{-3}	0.14	2.0×10^{-8}
B_7	2.82	—	3.4×10^{-6}	1.5	1.5×10^{-3}	0.14	3.0×10^{-9}
B_8	2.82	3.3×10^{-2}	—	—	2.2×10^{-7}	0.14	3.3×10^{-9}

Table 5.4: The probabilities of each step of the generation of the background due to the gas inside TPC.

5.3.2 Backgrounds to the neutron capture in ^{3}He

Backgrounds to the neutron capture in ^{3}He are also categorized according to methods of the subtraction.

- S_n : Neutron capture in ^{3}He
  The neutron is captured in ^{3}He which subsequently decays into a proton and triton (σ=5333 barn, Q-value=782 keV) The rate with a ^{3}He partial pressure of 4.0 mPa at 276 degrees Kelvin corresponds to that of the neutron decay.

- B_n^{energy} : Neutron capture in N_2 inside the TPC
  The neutron is captured in N_2 and decays into a proton and ^{14}C (σ=1.83 barn, Q-value=626 keV). The contamination of the nitrogen is caused by outgassing or air leak, thus this reaction increases over time. The rate with a N_2 partial pressure of 5.8 Pa ($= 4.0$ mPa$\times\frac{5333\,\text{barn}}{1.83\,\text{barn}} \times 2$) at 276 degrees Kelvin corresponds to that of the neutron decay. The time structure is the same as that of the neutron capture in ^{3}He.

- B_n^{tof} : Environmental radiation
  The flat background stems from natural α-activity on the surface of the detector such as radon. The half-life of the radon is 3.8 day, thus this reaction decreases over time.

- B_n^{gas} : Scattered neutron capture in ^{3}He inside the TPC
  The neutron is scattered by He and CO_2 inside the TPC with a probability of 3.3×10^{-2} per meter and some scattered neutron are captured in ^{3}He. The time structure is the same as that of the neutron decay signal.

In particular B_n^{energy} is caused by N_2 contained in the outgas and the reaction of $^{14}N(n,p)^{14}C$ cannot be discriminated from the neutron capture in ^{3}He with the energy resolution of the TPC as shown in Figure 5.2. Thus we have no choice to thoroughly remove the N_2 gas from the vacuum chamber to reduce the $^{14}N(n,p)^{14}C$ reaction to less than 0.1% of the ^{3}He$(n,p)^3$H reaction.
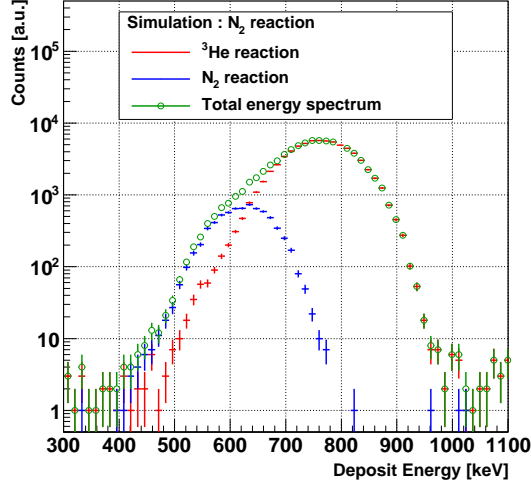
Figure 5.2: The expected pulse height spectrum of ^{3}He reaction candidates. The red cross is the ^{3}He spectrum measured by the TPC with an anode voltage of 1100V. The blue cross is the expected N_2 spectrum obtained by linear scaling of the Q-value as 10% of ^{3}He events.

5.4   Signal separation by using calorimetric approach

5.4.1   Separation between S_β and S_n

An electron from the neutron decay has an energy up to 782 keV and the energy of the proton is less than 0.754 keV. On the other hand, the neutron capture in ^{3}He generates the proton and triton with energies of 579 keV and 191 keV, respectively. Figure 5.3 and 5.4 show the rate of energy loss per unit length (dE/dx) and range of the electron and proton in the gas inside the TPC (He : CO_2 = 85kPa : 15kPa). It is found that the dE/dx of the electron is smaller than that of the proton by two orders of magnitude. According to the Bethe-Bloch formula, dE/dx decreases as β^{-2} with increasing energy and it reaches 0.8 keV/cm.

The energy deposit varies substantially depending on the initial energy of the electron. Figure 5.5 and Table 5.5 show the relationship between the energy of
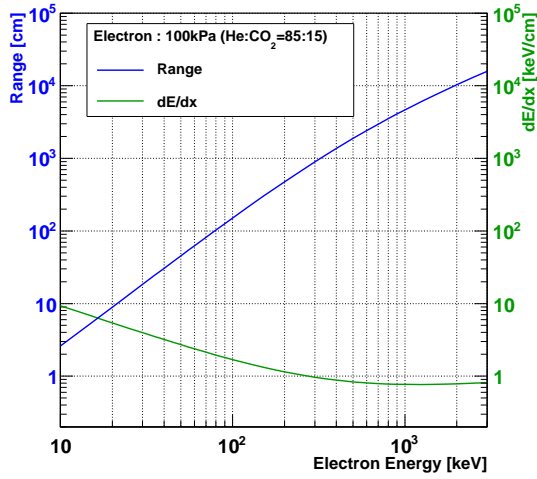
Figure 5.3: Flight range and dE/dx for electron with its energy.
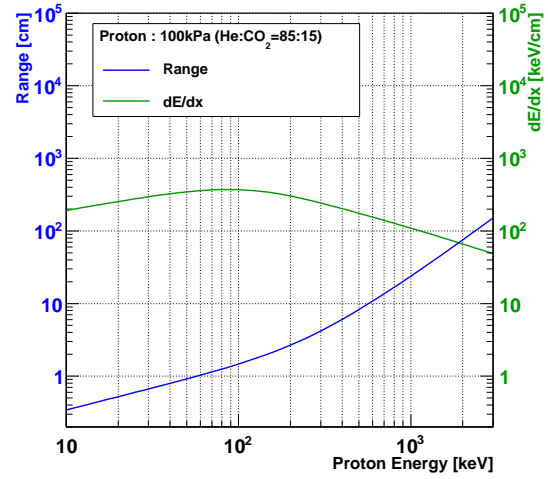
Figure 5.4: Flight range and dE/dx for proton with its energy.

the electron and the energy deposit inside the TPC ($300mm \times 290mm \times 960mm$), assuming the neutron decays in the fiducial volume ($20mm \times 20mm \times 800mm$). At low energy the energy deposit inside the TPC is increasing until the range of trajectory excesses the TPC size. Then it is decreasing with a progressive reduction in dE/dx.
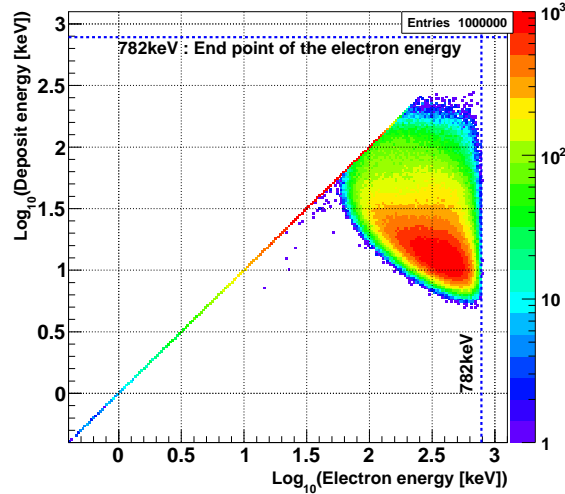
Figure 5.5: The relation between electron initial energy and the energy deposit on the TPC under 100 kPa.

The neutron capture in ^{3}He is also shown (blue, Figure 5.6),

Figure 5.6 shows the energy spectra of the neutron decay (red), the neutron

Electron energy	0$\sim$60 keV	60$\sim$200 keV	200$\sim$782 keV
Terminal position	inside the TPC	inside/outside the TPC	outside the TPC
Deposit energy	0$\sim$60 keV	12$\sim$200 keV	8$\sim$30 keV

Table 5.5: Energy, terminated position and deposit energy in TPC for electrons produced by the neutron decays on the beam axis under 100 kPa.

capture in ^{3}He (blue) and the neutron capture in CO_2 (green). The neutron capture in ^{3}He has a broad energy spectrum due to the saturation effect as described in Section 4.4. This simulation assumes the gain of MWPC as 50000 in Eq. 4.6. Figure 5.7 shows the separation between the neutron decay and the neutron capture in ^{3}He by means of the maximum energy deposit among the field wires, since a Bragg peak of the protons and tritons from the ^{3}He reaction is much higher than that of the electrons. The selection in terms of the range of the trajectory is also effective for the separation. By requiring the events with a range of less than 10cm (red, Figure 5.7), the extraction of the ^{3}He reaction can be fully achieved by using a threshold of 35 keV. Thus the analyzed data ($N^{100\text{kPa}/0.1\text{Pa}}$) is divided into candidates of the neutron decay ($N_\beta^{100\text{kPa}/0.1\text{Pa}}$) and candidates of the neutron capture in ^{3}He ($N_n^{100\text{kPa}/0.1\text{Pa}}$). However the candidates of the neutron decay include off-axis neutron capture in ^{3}He (pink, Figure 5.7), which is subtracted by using ^{3}He-enriched measurement as described in Section 5.6.

5.4.2   Separation between S_β and B_β^{energy}

A nucleus in the gases captures the neutron and the emitted prompt γ ray recoils the nucleus with an energy of $\frac{E_\gamma^2}{2M}$, where E_γ is the energy of prompt γ ray and M is the mass of the recoil nucleus. This event occurs along the neutron beam axis, thus can not be distinguished from the neutron decay. Table 5.6 summarizes the recoil energy E_{recoil} for the prompt γ ray and the maximum energy E_γ for typical nuclei. The natural abundance and the neutron capture cross section are also shown.

Among the using gas, the cross sections of helium and oxygen are negligibly small, however ^{12}C has also large neutron capture cross section and corresponds to 2.5 times larger than the neutron decay rate. The recoil energy is 1.01 keV, thus more than 99.9% of the electrons from the neutron decay can be be distinguished by means of the energy spectrum. In addition, carbon contains ^{13}C at a rate of 1.1% and its recoil energy is 2.56 keV. To avoid the influence on the neutron decay, ^{13}C-free CO_2 is needed.
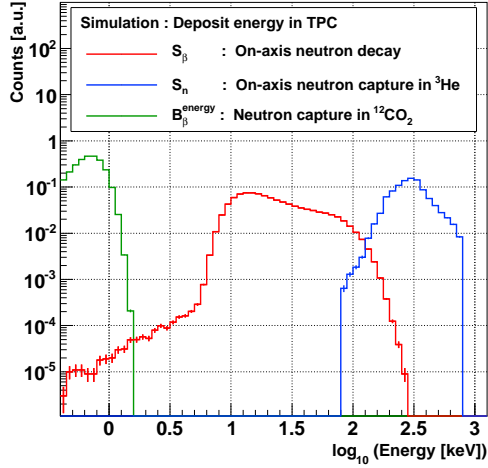
Figure 5.6: Energy spectrum of the deposit energy inside the TPC by neutron decay (red), neutron capture in ^{3}He (blue), and CO_2 (green) under 100 kPa.
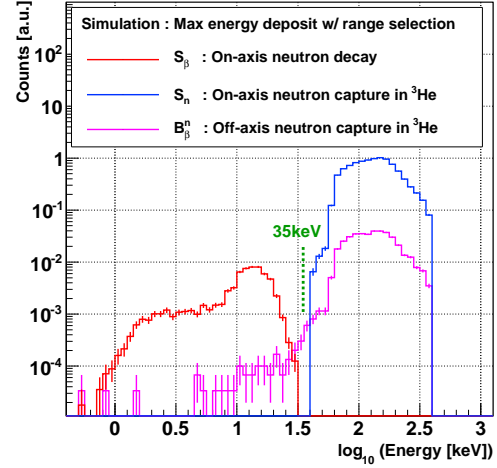
Figure 5.7: Simulated maximum energy depositions among the wires after the range selection by on-axis neutron decay (red), on-axis neutron capture in 3He (blue) and off-axis neutron capture in 3He (pink) under 100 kPa.

The separation between S_β and B_β^{energy} depends on the fluctuation of the number of initial ionized electrons, which is determined by W value as Section 4.2. However it is deteriorated by a recombination effect at the time of ionization (R), an attenuation efficiency during the drift ($A(y)$) and a non-uniformity of the gain (G). The output of the TPC caused by deposit energy E is described as following equation.

$$Output \propto \frac{E}{W} \times (1 - R) \times \{1 - A(y)\} \times G. \tag{5.2}$$

Figure 5.8 shows more than 99.9% electrons from the neutron decay under 50

	Natural abundance	σ_γ	E_γ [MeV]	E_{recoil} [keV]
^{1}H	99.985	0.3326	2.22	1.32
^{2}H	0.015	0.000529	6.25	6.96
^{4}He	99.99986	0	—	—
^{12}C	98.9	0.00353	4.95	1.01
^{13}C	1.1	0.00137	8.17	2.56
^{16}O	99.762	0.0001	3.27	0.339
^{17}O	0.0038	0.236	4.37	0.570

Table 5.6: Neutron capture cross sections, energy of emitted gamma, and their recoil energies for isotopes.

kPa and 100 kPa can be separated from B_β^{energy} with an energy threshold of 1.4 keV, if the performance of the TPC satisfied the requirement as shown in Table 5.7.
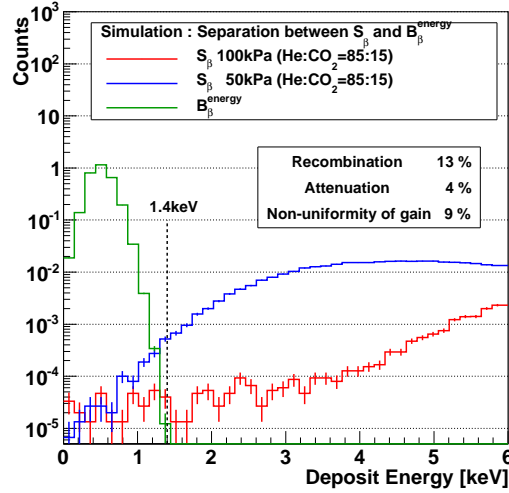
Figure 5.8: A separation between the electron from the neutron decay and the neutron capture in CO_2. Assumed detector performance of the TPC is also shown.

Recombination at the time of ionization	$< 13\%$
Attenuation during the drift of 150 mm	$< 4\%$
Non-uniformity of the gain	$< 9\%$

Table 5.7: Requirement for the performance of the TPC in order to separate the neutron decay (S_β) and the recoiled nucleus (B_β^{energy}).

5.5   Signal selection by using track finding

In order to select the neutron decay and the neutron capture in ^{3}He, a new variable X and a weighted center in x axis are introduced, respectively, which do not decrease the detection efficiency for both reactions under the reduced pressure.

5.5.1   Selection of the neutron decay

For the reduction of the background to the neutron decay, the signal selection criteria are as follows:

- the deposit energy is larger than that of the recoiled nucleus (1.4 keV),

 • the trajectory has a intersection with fiducial volume.

Even after the selection, more than 99.9% detection efficiency for the neutron decay is performed. The first criterion is for the discrimination of B_0 and the second criterion is explained in the following sentence.

By using the topological difference between the neutron decay and the background, an effective subtraction of the background is performed. For instance, the prompt γ rays from the ^{6}Li plates knock out the electrons on material of the TPC itself, thus they originate on the inside wall of the TPC. On the other hand, the neutron decay occurs along the beam axis.

One should note that the end points of the tracks do not necessarily correspond to the center of the TPC, since the probability of the backscattering on the ^{6}Li plate is more than 1% as shown in Figure 5.9. In particular, more than 0.1% electrons come back to the fiducial volume. The TPC reconstructs the tracks by orthogonal wires and has difficulty separating close tracks.
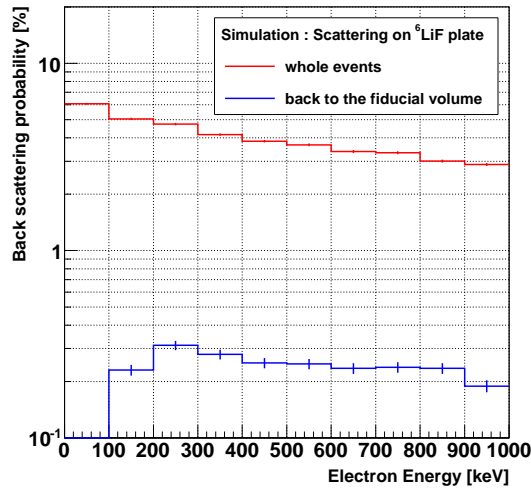
Figure 5.9: A probability of the back scattering on the wall inside the TPC. All scattering events are shown in a red line and those which go back to the fiducial volume are shown in a blue line.

Thus a new variable X is introduced as follows:

1. define the region of neutron bunch on the beam axis,

2. search fa pair of anode and cathode wires (which are orthogonal by design) whose pulses have temporal overlap,

3. calculate the closest distance from the beam axis.

The procedure is also described in Figure 5.10. Since the distance is calculated for not only the end points but also for all the hits, a robust analysis can be performed as shown in Figure 5.11 in case the track reconstruction get worse due to the backscattering.
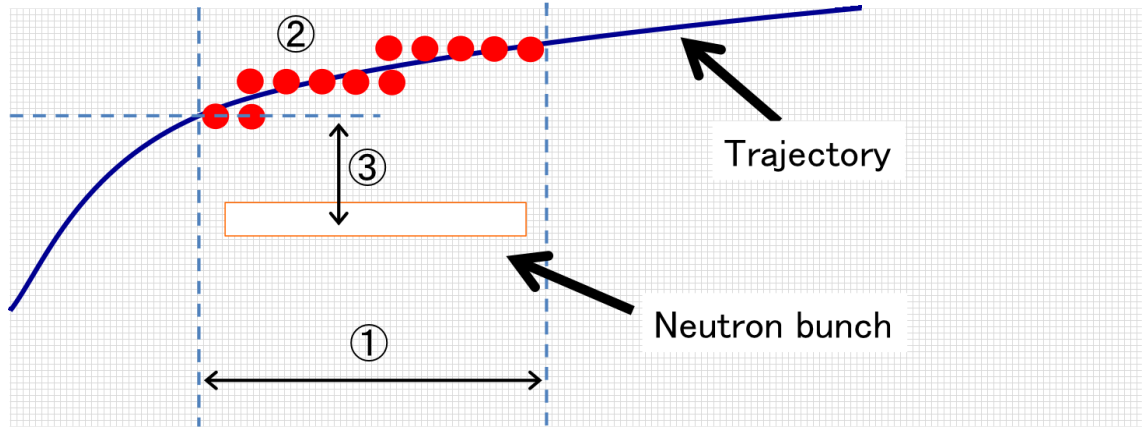
Figure 5.10: A schematic view of trajectory in TPC (XY image).
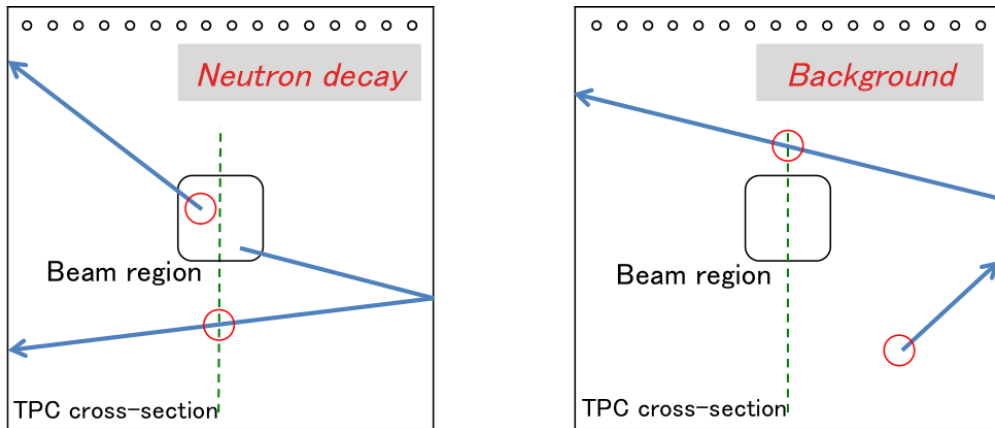
Figure 5.11: A schematic view of a trajectory in TPC (YZ image) in case of neutron decay (left) and background (right). A distance between a red circle and a green line corresponds to X value.

Figure 5.12 shows the X distribution for the neutron decay and B_β^{gas}. The distribution of the neutron decay is localized as $X < 4$ wires. The background due to the γ ray from CO_2 (B_7) has the same distribution as the neutron decay, since it is associated with the recoil atom along the beam axis. On the other hand, the background due to the γ ray from the ^{6}Li plates (B_6) and the off-axis neutron decay (B_8) have broad distributions in X which are smeared along the size
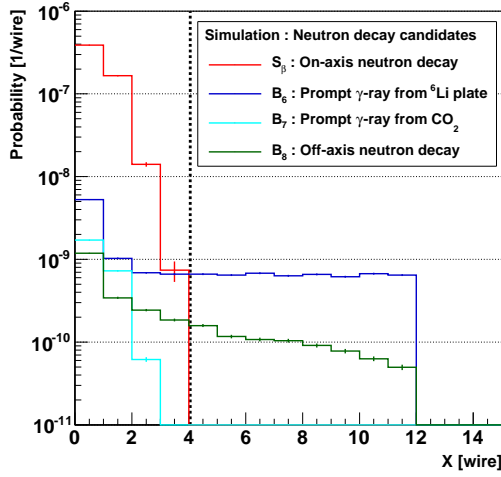
Figure 5.12: The simulated X distribution of signal and backgrounds.
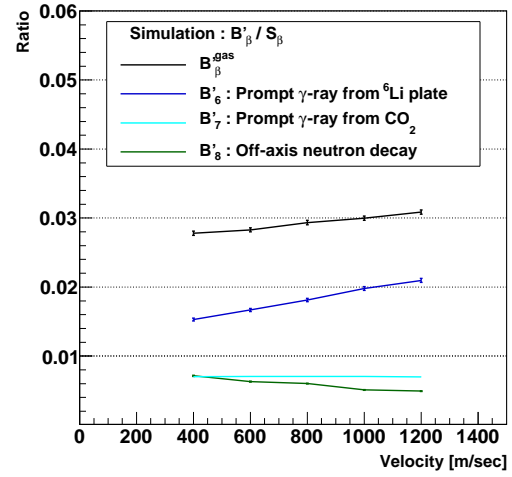
Figure 5.13: The ratio of signal to backgrounds with X less than 4 wires.

of the TPC. The background ratios due to the scattered neutron have a velocity dependence as shown in Figure 5.13, since the scattering cross section, angle and velocity of the scattered neutron are correlated with the incident velocity. The results for the selection are summarized in Table 5.8,

		B/S	B'/S
B_0	Recoiled nucleus due to prompt γ rays	3.0	3.0
B_1	Off-axis neutron capture in ^{3}He	7.7×10^{-3}	2.0×10^{-4}
B_2	Prompt γ rays outside the TPC	1.0	0.25
B_3	Radioactivation inside the TPC	4.9×10^{-3}	1.9×10^{-3}
B_4	Radioactivation outside the TPC	1.2×10^{-5}	3.0×10^{-6}
B_5	Environmental radiation	3.4	1.1
B_6	Prompt γ rays from ^{6}Li plate	4.7×10^{-3}	2.0×10^{-2}
B_7	Prompt γ rays from CO_2	7.0×10^{-3}	7.0×10^{-3}
B_8	Off-axis neutron decay	7.7×10^{-3}	5.1×10^{-3}

Table 5.8: Probabilities for each step of background generating due to the gases inside the TPC.

5.5.2 Selection of the neutron decay under reduced pressure

The energy loss in the gas decreases under the reduced pressure, so that variation of the detection efficiency has to be considered. In this simulation, the measured detection efficiencies by using cosmic ray as described in Section 6.4 are applied.
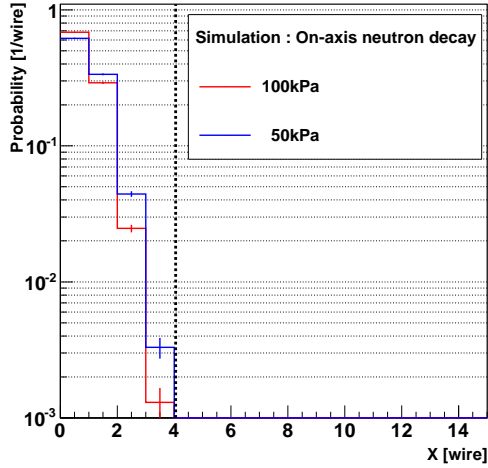
Figure 5.14: The simulated X distribution of signal with gas pressure of 100 kPa (red) and 50 kPa (blue).
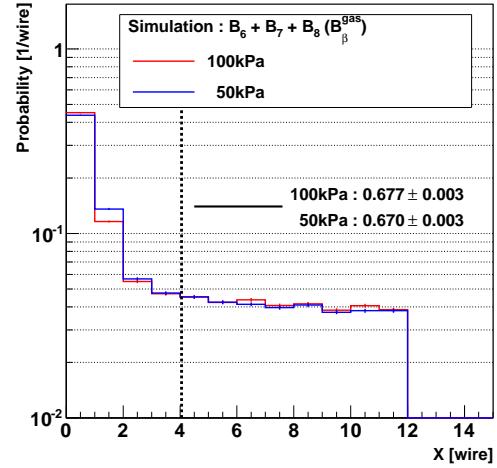
Figure 5.15: The X distribution of signal with gas pressure of 100 kPa (red) and 50 kPa (blue).

Figure 5.14 shows the X distribution of the neutron decay under 100 kPa and 50 kPa. It is found that both distributions are localized within less than 4 wires.

Figure 5.15 shows the X distribution of the summation of B_β^{gas} under 100 kPa and 50 kPa. The ratios in $X < 4$ wires are 67.7% and 67.0%, respectively, and the difference is $1.0 \pm 0.6\%$. Since the total background ratios are about 3% under 100 kPa as shown in Figure 5.13, the difference of the detection efficiency has a $3\% \times 1\% \sim 0.03\%$ effect on the counting rate, which is negligible.

5.5.3   Selection of the neutron capture in ^{3}He

As same as in the neutron decay, the track pattern of the on-axis neutron capture in ^{3}He is different from that of the off-axis neutron capture in ^{3}He. For the selection of the on-axis neutron capture in ^{3}He, a weighted center of the energy deposit can be used because the decay products, triton and proton, are stopped in the gas and are not scattered in their flight. Figure 5.16 shows the distribution of the weighted center and the background ratio is 0.28% in the case of 1000m/sec neutron. The velocity dependence is shown in Figure 5.17. The distribution of the off-axis neutron capture in ^{3}He is described by use of the angular distribution of the scattered neutron $P(\theta, \phi)$ as

$$P(x) \;=\; \int_D \frac{P(\theta, \phi)}{\cos\theta \sin\phi} dy dz,$$
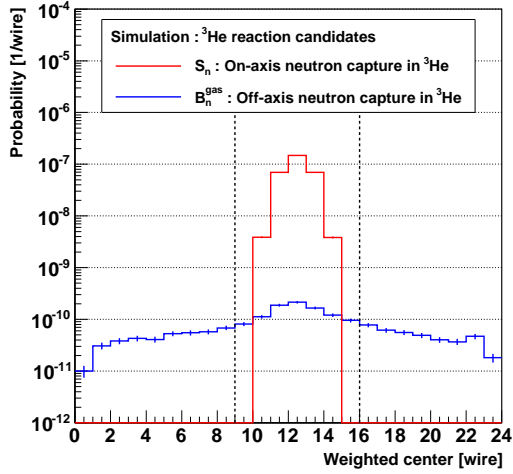
Figure 5.16: The weighted mean center of ^{3}He events.
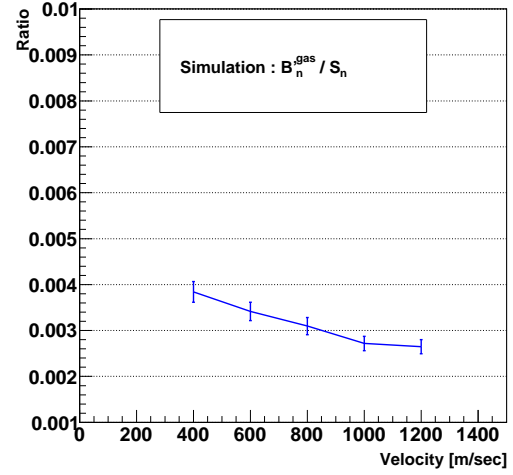
Figure 5.17: The ratio of off-axis to on-axis ^{3}He events whose weighted mean is in the central region.

where D is a plane inside the TPC which is perpendicular to the x axis. Since the angular distribution is analytically calculated.

5.5.4 Selection of the neutron capture in ^{3}He under reduced pressure

Figure 5.18 shows the distribution of the weighted center of the on-axis neutron capture in ^{3}He under 100 kPa and 50 kPa. The energy loss in the gas decreases under the reduced pressure, so that the ranges of the decay products become longer. However it is found that the distribution under 50 kPa is also localized as well as that under 100 kPa

Figure 5.19 shows the distribution of the weighted center of the off-axis neutron capture in ^{3}He under 100 kPa and 50 kPa. The ratios within the dashed line are 55% and 52%, respectively, and the difference is about $6 \pm 4\%$. Since the background ratios are less than 0.4% under 100 kPa as shown in Figure 5.17, the difference of the detection efficiency has a $0.4\% \times 6\% \sim 0.02\%$ effect on the counting rate, which is negligible.
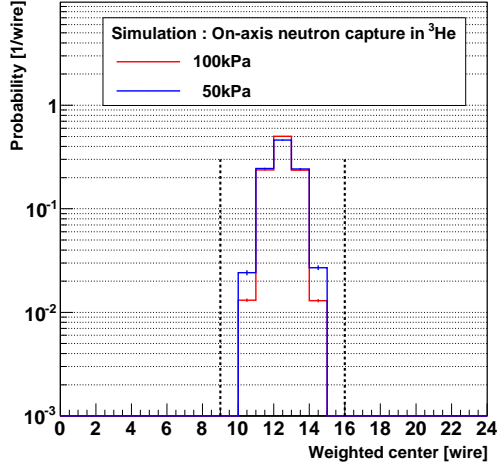
Figure 5.18: The simulated weighted center distribution of ^{3}He reaction with gas pressure of 100 kPa (red) and 50 kPa (blue).
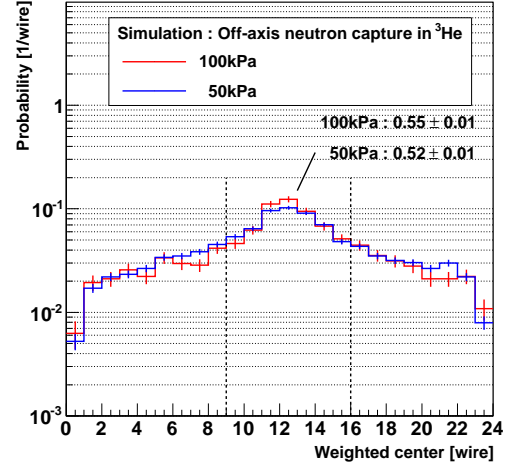
Figure 5.19: The simulated weighted center distribution of background to ^{3}He reaction with gas pressure of 100 kPa (red) and 50 kPa (blue).

5.6   Subtraction by using ^{3}He-enriched measurement

The off-axis neutron capture in ^{3}He (B_β^{n}) is included in the candidates of the neutron decay ($N_\beta^{100\mathrm{kPa}/0.1\mathrm{Pa}}$), which depends on the pressure of ^{3}He. Thus the ^{3}He-enriched measurement ($N_\beta^{100\mathrm{kPa}/1.0\mathrm{Pa}}$) is employed. Ratios of the ^{3}He pressures and the neutron flux between the measurements are denoted as k and α, so that each counting rate is wrote down as

$$
\begin{aligned}
N_\beta^{\prime\,100\mathrm{kPa}/0.1\mathrm{Pa}} &= S_\beta^\prime + B_\beta^{\prime\,\mathrm{gas}} + B_\beta^{\prime\,\mathrm{tof}} + B_\beta^{\prime\,\mathrm{n}}, \\
N_\beta^{\prime\,100\mathrm{kPa}/1.0\mathrm{Pa}} &= \alpha(S_\beta^\prime + B_\beta^{\prime\,\mathrm{gas}} + B_\beta^{\prime\,\mathrm{tof}} + kB_\beta^{\prime\,\mathrm{n}}).
\end{aligned}
$$

The neutron flux is measured by the neutron monitor as described in Section 3.5. In this calculation, k can be obtained as $1.0\mathrm{Pa}/0.1\mathrm{Pa} = 10$. From the two equations, the candidates of the neutron decay without the off-axis neutron capture in ^{3}He ($N_{\beta^\prime}^{\prime\,100\mathrm{kPa}}$) is calculated as

$$
N_{\beta^\prime}^{\prime\,100\mathrm{kPa}} = S_\beta^\prime + B_\beta^{\prime\,\mathrm{gas}} + B_\beta^{\prime\,\mathrm{tof}} = \frac{\alpha k N_\beta^{\prime\,100\mathrm{kPa}/0.1\mathrm{Pa}} - N_\beta^{\prime\,100\mathrm{kPa}/1.0\mathrm{Pa}}}{\alpha(k-1)}. \tag{5.3}
$$

The measurement time for $N_\beta^{\prime\,100\mathrm{kPa}/0.1\mathrm{Pa}}$ and $N_\beta^{\prime\,100\mathrm{kPa}/1.0\mathrm{Pa}}$ are denoted as $t^{100\mathrm{kPa}/0.1\mathrm{Pa}}$ and $t^{100\mathrm{kPa}/1.0\mathrm{Pa}}$. The total measurement time is described as $t^{100\mathrm{kPa}} = t^{100\mathrm{kPa}/0.1\mathrm{Pa}} +$

$t^{100\text{kPa}/1.0\text{Pa}}$. The uncertainty of the $N_{\beta'}^{'100\text{kPa}}$ is write down as following.

$$\Delta N_{\beta'}^{'100\text{kPa}} = \left| \frac{\sqrt{\alpha^2 k^2 \frac{N_\beta^{'100\text{kPa}/0.1\text{Pa}}}{t^{'100\text{kPa}/0.1\text{Pa}}} + \frac{N_\beta^{'100\text{kPa}/1.0\text{Pa}}}{t^{'100\text{kPa}/1.0\text{Pa}}}}}{\alpha(k-1)} \right| \tag{5.4}$$

$$= \left| \frac{\alpha k \sqrt{N_\beta^{'100\text{kPa}/0.1\text{Pa}}} + \sqrt{N_\beta^{'100\text{kPa}/1.0\text{Pa}}}}{\alpha(k-1)\sqrt{t^{100\text{kPa}}}} \right| \tag{5.5}$$

$$= \left| \frac{1+\alpha k}{1-\alpha k} \right| \sqrt{\frac{N_\beta^{'100\text{kPa}}}{t^{100\text{kPa}}}}, \tag{5.6}$$

where $t^{100\text{kPa}/0.1\text{Pa}} : t^{100\text{kPa}/1.0\text{Pa}} = \alpha k \sqrt{N_\beta^{'100\text{kPa}/0.1\text{Pa}}} : \sqrt{N_\beta^{'100\text{kPa}/1.0\text{Pa}}}$ is optimum. In addition, $N_\beta^{'100\text{kPa}} \sim N_\beta^{'100\text{kPa}/0.1\text{Pa}} \sim N_\beta^{'100\text{kPa}/1.0\text{Pa}}$ is assumed. In case of $\alpha = 1$ and $k = 10$,

$$\frac{\Delta N_{\beta'}^{'100\text{kPa}}}{N_{\beta'}^{'100\text{kPa}}} = \frac{1.2}{\sqrt{N_\beta^{'100\text{kPa}} t^{100\text{kPa}}}} \tag{5.7}$$

can be obtained.

5.7 Subtraction by using TOF spectrum

By using the TOF spectrum, the influence of the radioactivation and the environmental radiation can be evaluated. Not only that, the ^{6}Li shutter as shown in Section 3.5 enables to subtract the background due to the prompt γ ray from outside the TPC. The counting rates are classified by the region in the TOF spectrum and the condition of the ^{6}Li shutter as shown in Table 5.9. t_1 and t_0 correspond to the fiducial time and a subset of the time when the neutron bunch is not in the TPC, respectively. s_1 and s_0 denote the measurement with the ^{6}Li shutter opened and closed.

	Beam inside the TPC	No beam inside the TPC
Shutter opened	$N'^{100\text{kPa}}(s_1, t_1)$	$N'^{100\text{kPa}}(s_1, t_0)$
Shutter closed	$N'^{100\text{kPa}}(s_0, t_1)$	$N'^{100\text{kPa}}(s_0, t_0)$

Table 5.9: Classification by means of condition of the ^{6}Li shutter and the TOF spectrum.

5.7.1 Neutron decay

Assuming the SFC is set to produce one neutron bunch which arrives at the center of the TPC at 20 ms, the top of Figure 5.20 depicts a time spectrum for the

neutron decay, with the ^{6}Li shutter opened. The TPC has a 4π acceptance for the neutron decay in the time interval between the dashed lines. On the other hand, the bottom of Figure 5.20 depicts the distribution, with the ^{6}Li shutter closed. t_1 can be stretched for the statistics as long as possible and is denoted as $t_0 = k't_1$, where k' is a constant. Each spectrum is described in terms of the individual signal and background components as:

$$
\begin{aligned}
N'^{100\text{kPa}}_{\beta'}(s_1, t_1) &= S'_\beta + B'^{\text{gas}}_\beta + B'_2(s_1, t_1) + B'_3(s_1) + B'_4(s_1) + B'_5(s_1), \\
N'^{100\text{kPa}}_{\beta'}(s_1, t_0) &= B'_2(s_1, t_0) + k'B'_3(s_1) + k'B'_4(s_1) + k'B'_5(s_1), \\
N'^{100\text{kPa}}_{\beta'}(s_0, t_1) &= \alpha'\{B'_2(s_0, t_1) + B'_4(s_0) + B'_5(s_0)\}, \\
N'^{100\text{kPa}}_{\beta'}(s_0, t_0) &= \alpha'\{B'_2(s_0, t_0) + k'B'_4(s_0) + k'B'_5(s_0)\},
\end{aligned}
$$

where α' is a ratio of the neutron flux between the measurements. The radioactivation and environmental radiation are constant during the beam cycle of 40 ms, thus the time expressions are omitted in B_4, B_5 and B_6. B_2 is scaled according to the flux, so that following equation can be obtained.

$$
\alpha' = \frac{B'_2(s_0, t_1)}{B'_2(s_1, t_1)} = \frac{B'_2(s_0, t_0)}{B'_2(s_1, t_0)}.
$$

Finally the candidates of the neutron decay without B^{tof}_β ($N^{100\text{kPa}}_{\beta''}$) is calculated as

$$
\begin{aligned}
N'^{100\text{kPa}}_{\beta''} &= S'_\beta + B'^{\text{gas}}_\beta \\
&= N'^{100\text{kPa}}_{\beta'}(s_1, t_1) - \frac{1}{k'}N'^{100\text{kPa}}_{\beta'}(s_1, t_0) \\
&\qquad - \frac{N'^{100\text{kPa}}_{\beta'}(s_0, t_1) - \frac{1}{k'}N'^{100\text{kPa}}_{\beta'}(s_0, t_0)}{\alpha'}, \qquad (5.8)
\end{aligned}
$$

$$
\begin{aligned}
\Delta N'^{100\text{kPa}}_{\beta''} &= \frac{1}{\sqrt{t'^{100\text{kPa}}}}\left(\sqrt{N'^{100\text{kPa}}_{\beta'}(s_1, t_1) + \frac{1}{k'^2}N'^{100\text{kPa}}_{\beta'}(s_1, t_0)} \right. \\
&\qquad \left. + \frac{1}{\alpha'}\sqrt{N'^{100\text{kPa}}_{\beta'}(s_0, t_1) + \frac{1}{k'^2}N'^{100\text{kPa}}_{\beta'}(s_0, t_0)} \right), \quad (5.9)
\end{aligned}
$$

where $t'^{100\text{kPa}}$ denotes the summation of the measurement time with shutter opened and the shutter closed. Assuming $k' = 6.0\text{ms}/2.8\text{ms}$ as discussed in Section 5.2 and $\alpha' = 1.0$, the expected rates of each components are described in Table 5.10.

Substituting these values into Eq. (5.9), the statistical uncertainty is obtained as

$$
\frac{\Delta N'^{100\text{kPa}}_{\beta''}}{N'^{100\text{kPa}}_{\beta''}} = \frac{1.0 \times 10^1}{\sqrt{t'^{100\text{kPa}}}} \qquad\qquad (5.10)
$$
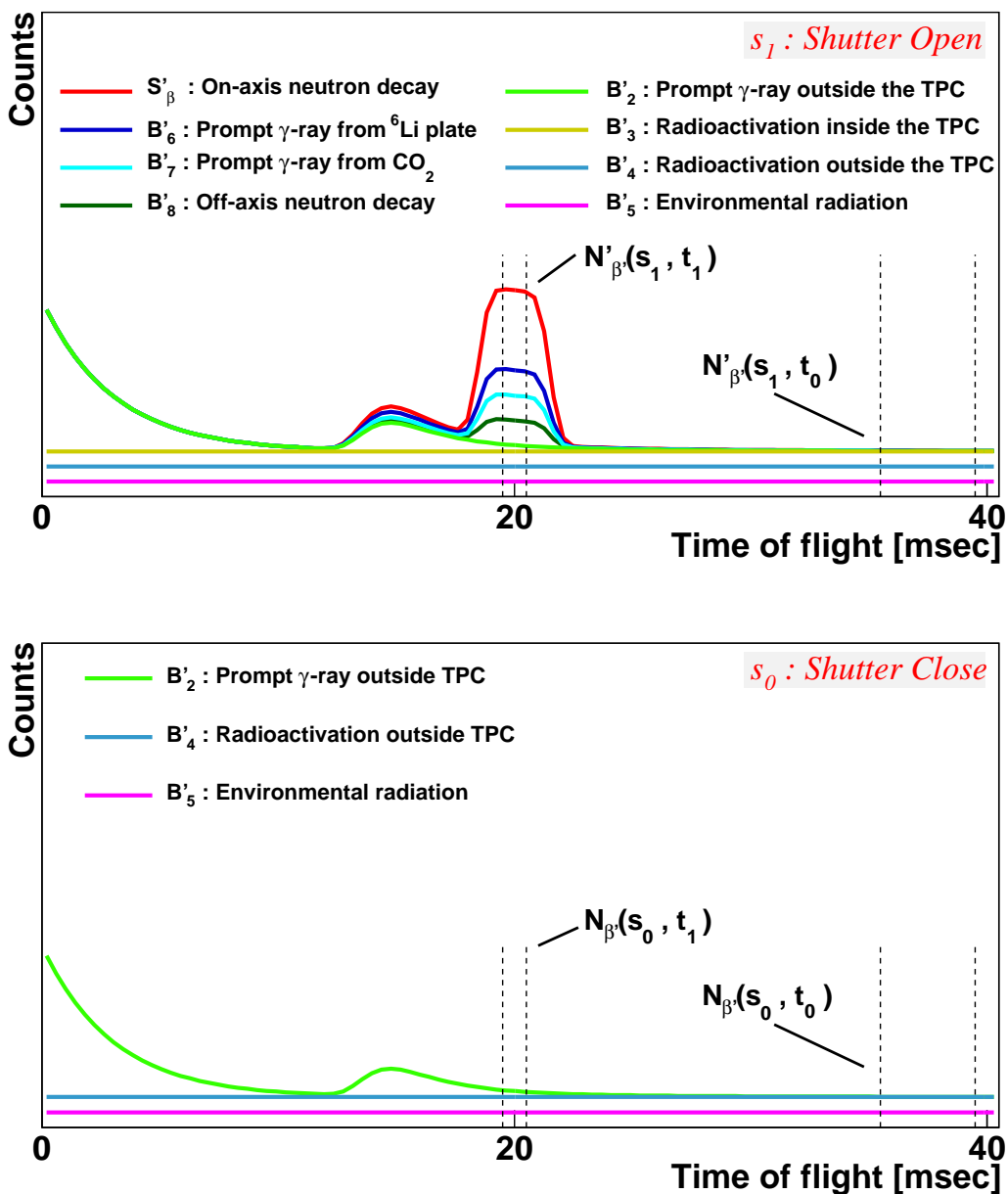
Figure 5.20: A schematic drawing of signal and background in TOF with the shutter open (top) and closed (bottom).

	$N_{\beta'}^{'100\text{kPa}}(s_1, t_1)$	$N_{\beta'}^{'100\text{kPa}}(s_1, t_0)$	$N_{\beta'}^{'100\text{kPa}}(s_0, t_1)$	$N_{\beta'}^{'100\text{kPa}}(s_0, t_0)$
S'	8.9×10^{-2}	—	—	—
B_2'	1.7×10^{-2}	3.0×10^{-2}	1.7×10^{-2}	3.0×10^{-2}
B_3'	4.4×10^{-4}	9.5×10^{-4}	—	—
B_5'	9.8×10^{-2}	2.1×10^{-1}	9.8×10^{-2}	2.1×10^{-1}
$B_\beta'^{\text{gas}}$	2.7×10^{-3}	—	—	—
Total	2.1×10^{-1}	2.4×10^{-1}	1.2×10^{-1}	2.4×10^{-1}

Table 5.10: Expected amount of the neutron decay and backgrounds in the TOF spectrum.

which corresponds to 0.48% of the statistical uncertainty for the 50 days of beam time with 220 kW of beam power.

5.7.2　Neutron capture in ^{3}He

Figure 5.20 depicts a time spectrum for the candidates of the neutron capture in ^{3}He, with the shutter opened. The distribution with the shutter closed consists of only the environmental radiation, thus the subtraction can be simplified and performed in the same manner as the neutron decay:

$$N_{n''}^{'100\text{kPa}} = S_n' + B_n'^{\text{gas}} = N_n^{'100\text{kPa}}(s_1, t_1) - \frac{1}{k'} N_n^{'100\text{kPa}}(s_1, t_0).$$

The count rate of the neutron capture in ^{3}He is controlled by the pressure. In the case of 0.1 Pa of the ^{3}He, the count rate is 25 times larger than that of the neutron decay. Thus the statistical uncertainty arising from the neutron capture in ^{3}He can be negligible.

5.8　Subtraction by using reduced-pressure measurement

All the remaining background at this stage is caused by the gas inside the TPC, so that the amount of the background is proportional to the gas pressure. The same procedures are applied to the data taking under 50 kPa ($N^{50\text{kPa}/0.1\text{Pa}}$ and $N^{50\text{kPa}/1.0\text{Pa}}$). The TPC performance under the reduced pressure is discussed in Section 5.5.2 and 5.5.4. Consequently, $N_{\beta''}^{'50\text{kPa}}$ and $N_{n''}^{'50\text{kPa}}$ can be obtained, which are wrote down as

$$
\begin{aligned}
N_{\beta''}^{'50\text{kPa}} &= \alpha''(S_\beta' + k'' B_\beta'^{\text{gas}}), \\
N_{n''}^{'50\text{kPa}} &= \alpha''(S_n' + k'' B_n'^{\text{gas}}),
\end{aligned}
$$
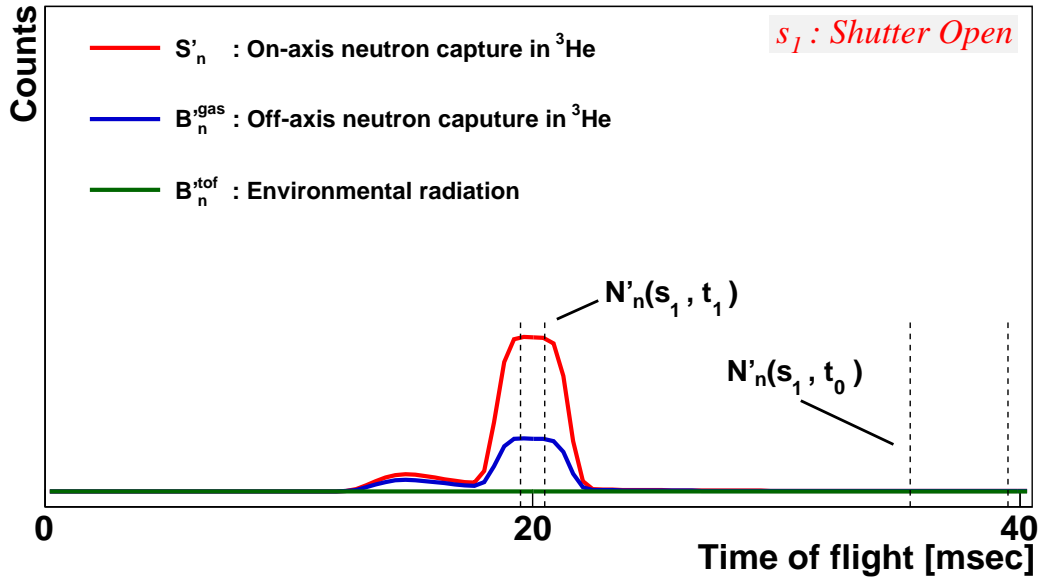
Figure 5.21: A schematic drawing of ^{3}He reaction candidates in TOF with shutter open.

where α'' and k'' are ratios of the neutron flux and the total pressure between the measurements, respectively. By comparing $N'^{100\text{kPa}}_{\beta''}$ and $N'^{100\text{kPa}}_{n''}$, S'_β and S'_n are extracted as

$$S'_\beta = \frac{N'^{50\text{kPa}}_{\beta''} - \alpha'' k'' N^{100\text{kPa}}_{\beta''}}{\alpha''(1 - k'')},$$

$$S'_n = \frac{N^{50\text{kPa}}_{n''} - \alpha'' k'' N^{100\text{kPa}}_{n''}}{\alpha''(1 - k'')}.$$

Finally, $\frac{S_n}{S_\beta}$ in the Eq. 5.1 can be obtained as

$$\frac{S'_n}{S'_\beta} = \frac{N'^{50\text{kPa}}_{\beta''} - \alpha'' k'' N'^{100\text{kPa}}_{\beta''}}{N'^{50\text{kPa}}_{n''} - \alpha'' k'' N'^{100\text{kPa}}_{n''}}.$$

In case of $\alpha = 1.0$ and $k = 1/2$, $t'^{50\text{kPa}} : t'^{100\text{kPa}} = 2 : 1$ is optimum, where $t'^{50\text{kPa}}$ denotes the total time for the measurement under 50 kPa. Thus

$$\frac{\Delta \tau_n}{\tau_n} = \sqrt{3} \frac{\Delta N'^{100\text{kPa}}}{N'^{100\text{kPa}}} \tag{5.11}$$

can be obtained. In 150 days an achievable statistical uncertainties are 0.82% with a power of 220 kW and 0.24% with a power of 1 MW as shown in Table 5.11.

In this section, the rate of the environmental background (B_5) is assumed as $B'_5/S = 1.1$, which can be obtained in the next chapter. The statistical uncertainty

| | | uncertainty [%] | |
		220 kW	1 MW
50 kPa	100 days	0.34	0.099
100 kPa	50 days	0.48	0.14
total	150 days	0.82	0.24

Table 5.11: Achievable statistical uncertainties.
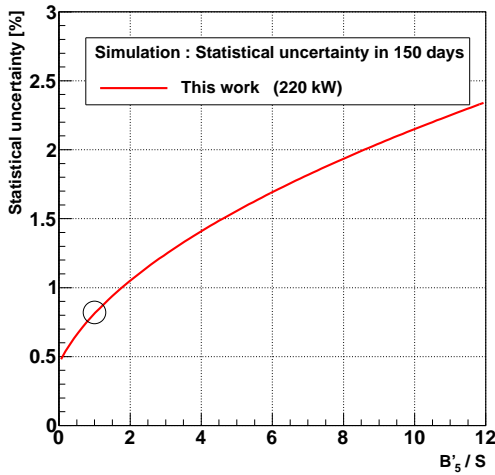
Figure 5.22: The achievable statistical uncertainty as a function of an amount of the environmental background after the signal selection (B'_5). A black circle describes the achieved $B'_5/S'_\beta \sim 1$ by the developed TPC in this thesis.
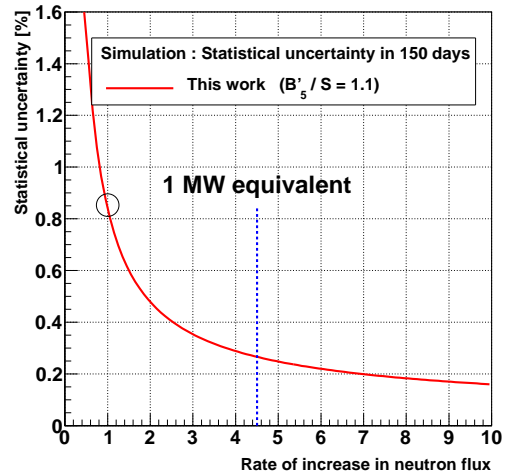
Figure 5.23: The achievable statistical uncertainty as a function of the beam power of J-PARC. A black circle describes the current beam power, 220 kW.

is depends on B'_5/S as shown in Figure 5.22, thus the reduction of the environmental background is required. The developed TPC in this thesis is aiming to achieve $B'_5/S \sim 1$.

Figure 5.23 shows a beam-power dependence of the statistical uncertainty, which motivates high flux of the neutron beams.

Chapter 6

Time projection chamber

In this chapter, the performance of the TPC is described. The requirement is summarized in Table 6.1.

Requirement	Value
environmental background	$B'_5/S \sim 1$
^{6}Li plate coverage	100%
detection efficiency for S_β and S_n	$> 99.9\%$

Table 6.1: Requirements for the TPC.

6.1 Development of the TPC without radioactive contamination

6.1.1 Material candidate

G10, which is commonly used for gas detectors, is made of continuous glass woven fabric base impregnated with an epoxy resin binder. While G10 has high mechanical strength, a silica, the raw materials for glass contains the Uranium-Thorium series radioisotopes. Ceramic made from alumina also contains ^{40}K in the K_2O mixed for workability. Thus other materials, three plastics and one ceramic are investigated for radioactive contamination. These materials are selected by means of the other aspects as shown in Table 6.2.

- Poly Ethel Ethel Ketone (PEEK)
  A thermoplastic resin produced by Yasojima Proceed Co. Ltd whose product name is PEEK450G. PEEK consists of only C, H and O without natural materials, thus the impurities cannot be mixed in. It has good fabrication

accuracy by means of the extrusion method and weldability due to the thermoplastic property.

- Poly Phenylene Sulfide (PPS)
  A thermoplastic resin produced by Yasojima Proceed Co. Ltd whose product name is FORTRON. The PPS consists of only C, H, O and S also without natural materials. The mechanical strength and water absorption are better than PEEK.

- Phenol Formaldehyde resin (PF)
  A thermohardening resin produced by Yasojima Proceed Co. Ltd whose product name is PS1121. The PF consists of only C, H and O without the natural materials and costs less than PEEK. However the mechanical strength is inferior to PEEK.

- Alumina
  A special ceramic produced by Ariake Materials Co. Ltd whose product name is MA995. The potassium content is reduced to 0.01wt%. Due to the sinter forming, the fabrication accuracy is worse than the above extruded plastics.

	G10	PEEK	PPS	PF	Alumina
density [g/cc]	1.8	1.3	1.4	1.4	3.9
bending elastic modulus [GPa]	20	3.6	3.9	0.15	350
melt point [°C]	—	334	278	130	1500
water-absorbing ratio [%]	0.10	0.14	0.04	0.3	0
volume resistance [Ω·m]	10^{11}	10^{14}	10^{14}	10^{12}	10^{15}
cost [1000JPY/kg]	3.3	45	8	5	100

Table 6.2: Properties of the material candidates which are density, bending elastic modulus, melt point, volume resistance and cost.

PEEK is selected by not only the low level of radioactivity as described in the next subsection, but also its insulating capacity for the high voltage, mechanical strength for the wire tension, heat tolerance for soldering, water absorption for vacuuming and cost as described in Table 6.2.

6.1.2 Study of the radioactive contamination by using germanium detector

According to the `Geant4` simulation, the requirement for the material of the TPC is calculated to be less than 0.01 Bq/cc. A germanium detector at Proton Beam
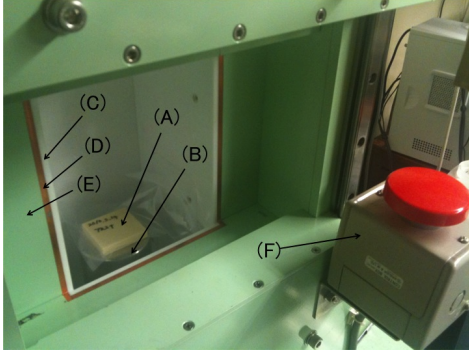
Figure 6.1: (A) sample, (B) Germanium detector, (C) Acrylic, (D) Oxygen-free copper, (E) Lead, and (F) Switch.
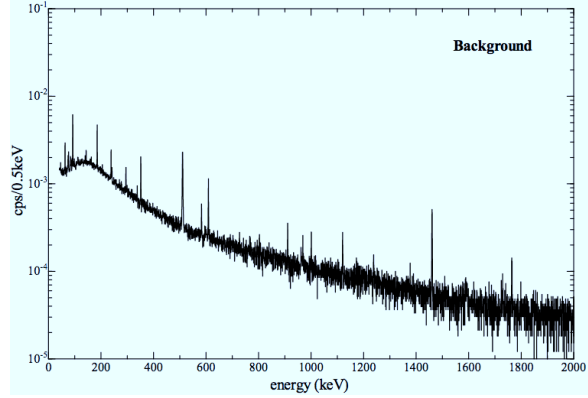
Figure 6.2: The measured value of radioactive contents for each materials in unit is Bq/cc.

Application Building in KEK is used for the measurement of the radioisotope. Figure 6.1 shows a picture of the sample laid on the germanium detector. The detector is surrounded by 1 cm thick acrylic plate, 1 cm thick oxygen-free copper and 10 cm thick lead. The energy spectrum of the measurement with no sample is indicated in Figure 6.2 and its counting rate is 1.26 cps.

PEEK, PPS, PS , Alumina and G10 are investigated for the material of TPC. In addition electronics such as pre-amplifiers, resistors, capacitors and cables are checked. Stainless steel and aluminum for the vacuum chamber, lead and iron for the shields and ^{6}Li plate for the neutron shielding are also tested. Figure 6.3 and 6.4 shows the energy spectrum of the G10 and PEEK after subtraction of the background as shown in Figure 6.2 for instance. It is found that there is no significant peak in the spectrum of PEEK.

In order to convert from the counting rate of the germanium detector to Bq, self-shielding have to be considered. An efficiency of the self-shielding ϵ is empirically expressed in terms of the energy of γ ray, E_γ, as

$$\ln \epsilon = a + b \ln E_\gamma + c(\ln E_\gamma)^2, \tag{6.1}$$

where a, b and c are calculated from the composition of each material. The results are summarized in Table 6.3. For the material of the TPC, PEEK, PS and Alumina satisfy the requirement. Among these candidates, PEEK has a better fabrication accuracy than that of Alumina and a better bending elastic modulus than that of PS. Thus PEEK is chosen for the material of the TPC. However due to the lower bending elastic modulus than that of G10, the wire tension make the PEEK frame would distort, so that a pretension is applied while soldering the wires to
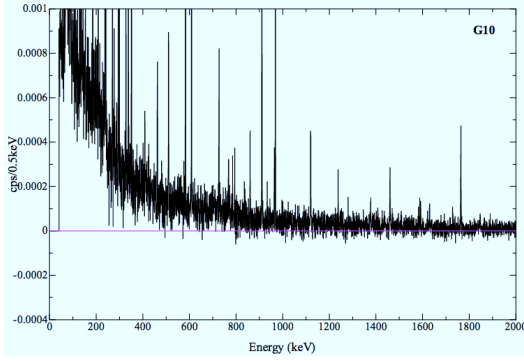
Figure 6.3: A energy spectrum of the germanium detector with G10. The background was subtracted.
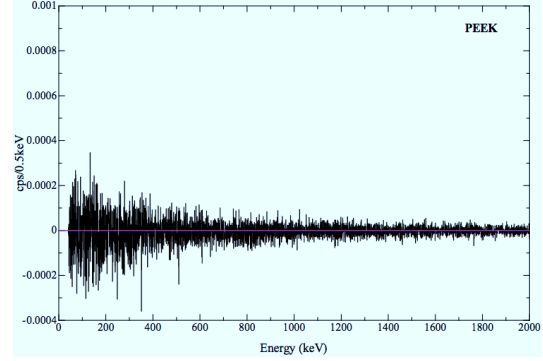
Figure 6.4: A energy spectrum of the germanium detector with PEEK. The background was subtracted.

the frame as described in the next section.

The radioisotopes in the other components of the TPC such as pre-amplifier, resistor, capacitor and ^{6}Li plate, are also confirmed to be satisfied the requirements.

6.1.3 Design of TPC

The TPC consists of a drift part and a MWPC part. The electrons ionized by a passing charged particle inside the drift part move under the electric field which is generated by a positive voltage applied on the bottom of the drift part and energized wires as shown in Figure 6.5. Resistors are installed between the wires and make a uniform field. Whole picture is shown in Figure 6.6.

The MWPC consists of three-layered wires. The anode wires are parallel to the neutron beam and the cathode wires are perpendicular to the beam. Considering the energy loss of the minimum ionization under 100 kPa (He : CO_2 = 85 : 15), the pitch of anode wire set to be 12 mm enables to collect at least one ionized electron at 99.9% by using `Geant4`. Field wires are located between the anode wires for the confinement of the electric field. The gap between the anode and cathode is set to be 6 mm for axial symmetry. The cross section of the electric field can be shown in Figure 6.7 and the detail specification is described in Table 6.4.

Two 6-mm thick PEEK frames are used for the MWPC part. One has the anode/field wires and the top of the cathode wires on both sides; the other has the bottom of the cathode wires on one side. The wires are soldered to the circuit on the kapton film pasted on the PEEK frame as shown in Figure 6.8. The position of wires are determined by grooves with a width of 100 μm as shown in Figure 6.9.

The anode plane consists of 24 sense wires (ϕ 20 μm) and 24 field wires

Isotope	^{212}Pb	^{214}Pb	^{228}Ac	^{214}Pb	^{208}Tl	^{214}Bi	^{212}Bi	^{208}Tl	^{228}Ac	^{40}K	^{214}Bi
E$_\gamma$[keV]	239	295	338	352	583	609	727	861	911	1461	1765
PEEK	—	—	—	—	—	—	—	—	—	—	—
PPS	0.0016	—	—	—	—	0.0028	0.0080	—	—	0.0068	—
PS	—	—	—	—	—	—	0.0080	—	—	—	—
Alumina	—	—	—	—	—	(0.0026)	—	—	0.0020	—	—
G10	0.0480	0.0272	0.0424	0.0257	0.0135	0.0201	0.0480	0.0142	0.0412	0.022	0.0267
Pre-amplifier	—	—	—	—	—	—	—	—	—	—	—
Resistor	—	—	—	—	—	—	—	—	—	—	—
Capacitor	—	—	—	—	—	—	—	—	—	—	—
^{6}Li plate	—	—	—	—	(0.0006)	—	—	—	—	—	—
SUS304	0.0012	—	—	—	(0.0011)	(0.0025)	—	—	—	0.0116	—
Al	0.0028	—	—	—	—	—	—	—	—	0.0072	—

Table 6.3: Radioisotopes in the samples in Bq/cc unit.

Figure 6.5: A photograph at the front of the field cage.
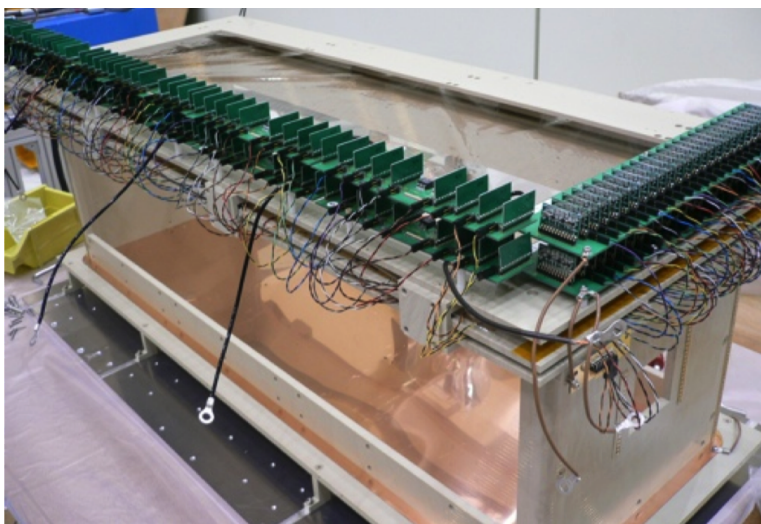
Figure 6.6: A photograph of a whole image of TPC without ^{6}Li plate.
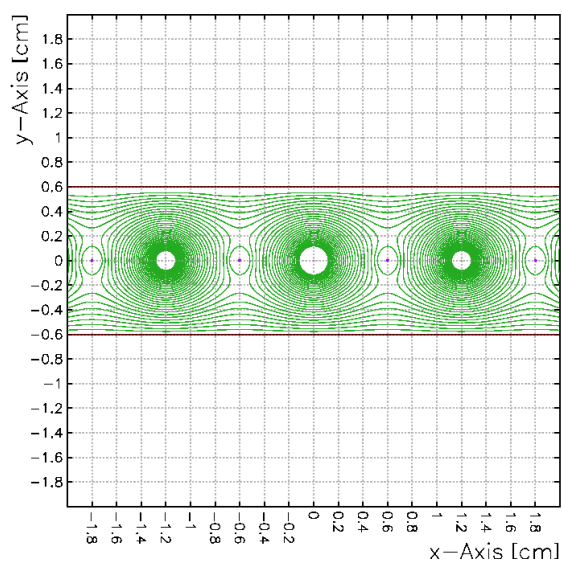
Figure 6.7: A electric field around the anode wire, calculated by Garfield.

	cathode (top)	anode / field	cathode (bottom)
diameter	ϕ 50 μm	ϕ 20 μm / ϕ 50 μm	ϕ 50 μm
$\Delta r_a/r_a$	0.02	0.02	0.02
material	Au-Be-Cu	Au-W / Au-Be-Cu	Au-Be-Cu
pitch	6 mm	6 mm	6 mm
Angle to the beam	90°	0°	90°
Applied voltage	0 V	1720 V / 0 V	0 V
AMP mode	high	high / low	low

Table 6.4: Specification details of wires; cathode, anode, and field.

(ϕ 50 μm) alternatively placed every 6 mm with applied voltages of 1720 V and 0 V, respectively. Each cathode plane consists of 6mm-spaced 160 cathode wires (ϕ 50 μm) and 4 cathode wires are linked up to an amplifier.

The resistor of 1 MΩ connects the anode wire to a power supply so that only a small fraction of the signal is lost into the power supply. In addition, the capacitor of 1 nF connects the anode wire for decoupling the amplifier.

As described in Section 5.4.2, the non-uniformity of the gain at the anode wires has to be suppressed less than 9%, which is influenced by a non-uniformity of the diameter of the anode wire $\Delta r_a/r_a$, a displacement of the anode wire Δx and a deformation of the cathode wire Δy as described in Table 6.5. In the case of the developed TPC, $\Delta r_a/r_a < 0.02$ and $\Delta x < 0.05$ mm are obtained.

A deformation of the cathode wire depends on the tension T as in the following equation:

$$\Delta y = \frac{FL^2}{8T}, \tag{6.2}$$

where F is a electric force from the anode wire and L is a length of the cathode wire. In this experiment 20 g of the wire tension is required, which corresponds to $dG/G = 1\%$.

Imperfection	dG/G
non-uniformity of the diameter of the anode wire	$2.9\Delta r_a/r_a \sim 6\%$
displacement of the anode wire	$0.49\Delta x \sim 2\%$
deformation of the cathode wire	$0.69\Delta y \sim 1\%$
total	7%

Table 6.5: A relationship between imperfections of the wires and expected variations of the gain, which is calculated according the work by G. A. Erskine [53]. Δx and Δy are in mm unit.

Figure 6.8: A closeup view of the MWPC part.
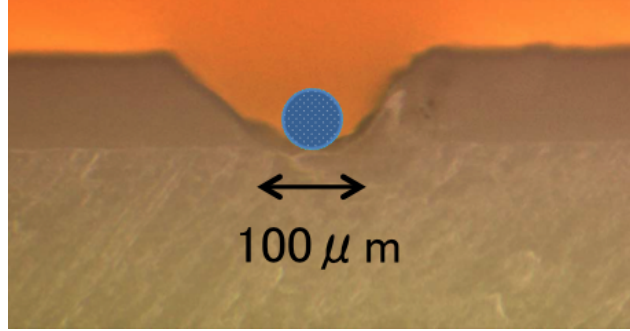
Figure 6.9: A closeup view of the cross section of the MWPC part.
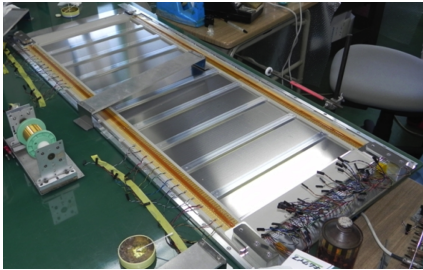
Figure 6.10: A photograph of the tensioning device.
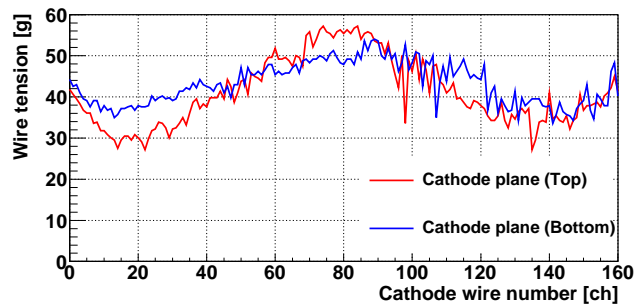
Figure 6.11: A distribution of the tension on each wire.

However the mechanical strength of PEEK is lower than G10, the frame bends beneath the burden of the wire tension. Calculating the displacement under the desirable tension, the suitable pre-tension is applied to the frame during the soldering as shown in Figure 6.10. Figure 6.11 shows a variation of the wire tension and the minimum tension is 27.2 g, which is higher than designed value, 20 g.

The non-uniformity of the gain is expected to be less than 7% in total. The measurement is shown in Figure 6.30.

6.1.4   Design of vacuum chamber

For the purpose of the determination of the ^{3}He density, the TPC is housed in a vacuum chamber and the gas is filled after the vacuuming. During the operation of the TPC, there is no gas flow into the vacuum chamber. Figure 6.12 shows a stainless-steel vacuum chamber, which has three aluminum flanges with feedthroughs. The detail specification is summarized in Table 6.6.

The stainless steel and the aluminium are also checked by the germanium detector. As shown in Table 6.3, both materials contain ^{212}Pb and ^{40}K. While

Figure 6.12: A photograph of the vacuum chamber.

Specification	Values
Chamber material	stainless-steel (SUS304)
Chamber outer size	680 mm (x) × 730 mm (y) × 1230 mm (z)
Chamber inner size	630 mm (x) × 680 mm (y) × 1180 mm (z)
Lid material	aluminium (A5052)
Upper lid size	630 mm (x) × 25 mm (y) × 1180 mm (z)
Side lid size	25 mm (x) × 680 mm (y) × 1180 mm (z)
Dry pump vacuum rate	450 l/min (Adixen ACP28)
Turbo pomp vacuum rate	210 l/sec (PFEIFFER TMU261)
Achieved vacuum (1 day)	1×10^{-4} Pa
Outgas rate (w/o baking)	5×10^{-5} Pa/sec
Leak rate	4.4 Pa/day

Table 6.6: Specification detail of the vacuum chamber.

the β ray from the radioisotope is mostly stopped inside the material, a Compton electron induced by the γ ray from the radioisotope can hit the TPC. ^{212}Pb emits 239 keV γ ray with 88% branching ratio and ^{40}K emits 1461 keV γ ray with 11% branching ratio. Table 6.7 summarizes the `Geant4` simulation of the radioisotopes contained in the vacuum chamber. As a result, the background rate is expected to be 0.21 cps, which satisfies the requirement.

6.2 Installation of the ^{6}Li plate

In the TPC, some of the incident neutrons are scattered by the gas and captured in the material of the TPC with prompt γ ray. Thus the scattered neutrons have

	material	Stainless-steel (SUS304)	Aluminium (A5052)
	volume [cm^3]	1.3×10^4	2.2×10^4
^{212}Pb	Bq	$(1.6 \pm 1.1) \times 10^1$	$(6.2 \pm 0.9) \times 10^1$
	Hit probability	$(1.5 \pm 0.1) \times 10^{-3}$	$(1.7 \pm 0.1) \times 10^{-3}$
	TPC hit [cps]	$(2.4 \pm 1.8) \times 10^{-2}$	$(10.5 \pm 2.2) \times 10^{-2}$
^{40}K	Bq	$(1.5 \pm 0.8) \times 10^2$	$(1.6 \pm 1.1) \times 10^2$
	Hit probability	$(2.7 \pm 0.2) \times 10^{-4}$	$(2.3 \pm 0.2) \times 10^{-4}$
	Expected TPC hit [cps]	$(4.1 \pm 2.5) \times 10^{-2}$	$(3.7 \pm 2.9) \times 10^{-2}$
	Total TPC hit [cps]	0.21 ± 0.05	

Table 6.7: Radioactive contamination inside the materials of the vacuum chamber.

Figure 6.13: A photograph of ^{6}Li plate.

Figure 6.14: A photograph of the inside of TPC.

to be captured by some nuclei such as ^{3}He, ^{6}Li and ^{14}N, all of which causes two body decays without γ-ray emission. The products of the two body decays are also nuclei thus they can be easily stopped by a thin material.

In this experiment, 95% ^{6}Li-enriched plate which consists of LiF : PTFE = 30wt% : 70wt% is produced for the scattered neutron as shown in Figure 6.13. As shown in Table 4.1, more than 99.99% of the reaction in the plate is $n +^6 \text{Li} \rightarrow^3 \text{H} + \alpha$ (Q=4.8 MeV) and 200 μm thick pure PTFE on the surface is sufficient to stop the decay products. The plates are installed into the TPC and the coverage from the beam axis is 100%. Figure 6.14 shows the picture inside the TPC and the bottom is covered by 12 μm thick aluminized mylar, which prevents the buildup of static electric charge. The slit on the left is used for the calibration. A ^{55}Fe stage on a rotating table is set up beside the drift part. Figure 6.15 shows the ^{55}Fe stage with a collimator (left) and the LiF (top and bottom). During calibration, ^{55}Fe moves to a position lateral to the slit.

It is noteworthy that the ^{6}Li plate is a dielectric material and is installed
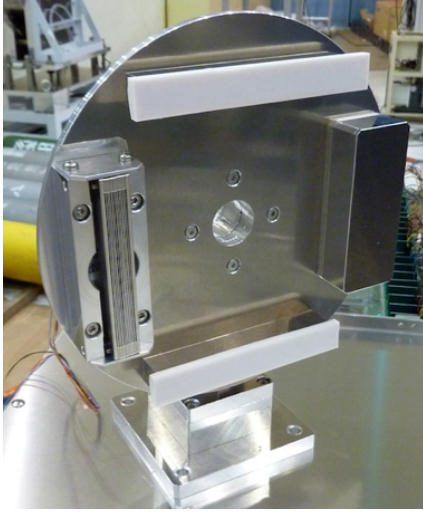
Figure 6.15: A photograph of the rotating table of ^{55}Fe stage.
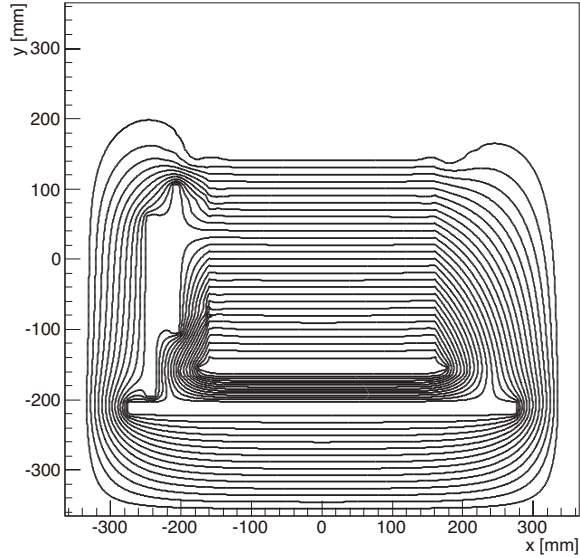
Figure 6.16: A XY image of the electric field of the drift region.

inside the wire. Relative permittivity of the ^{6}Li plate is measured as $\epsilon_r = 3.0$ by KEYCOM Corp. and that of the PEEK is $\epsilon_r = 3.2$ from its specification sheet. Thus the electric field is confirmed to be uniform by a calculation as shown in Figure 6.16.

Drift velocities under 50 kPa, 75 kPa and 100 kPa are measured by using electrons due to the environmental γ ray and can be calculated as shown in Figure 6.17. While the discharge voltage also decreases under reduced pressure, the drift velocity is inversely proportional to the pressure. It is confirmed that the drift velocity of 1 cm/μs can be possible. Figure 6.18 shows the position dependence under 100 kPa and 300 V/cm and the variation is less than 1%.

6.3 Performance of the background suppression

An environmental background of the TPC was 123.7 cps in the experimental area in the MLF. After housing in the lead shielding, the counting rate is decreased to 58.4 cps and the surrounding cosmic ray counters reduces it to 7.7 cps. According to the analysis algorithm as discussed in Section 5.4.2, the backgrounds for the neutron decay are events with an energy of more than 1.4 keV and with a hit in the fiducial region. Thus the selections, the energy cut and the fiducial cut, are applied and the eventual backgrounds can be obtained as 1.4 cps. Figure 6.19
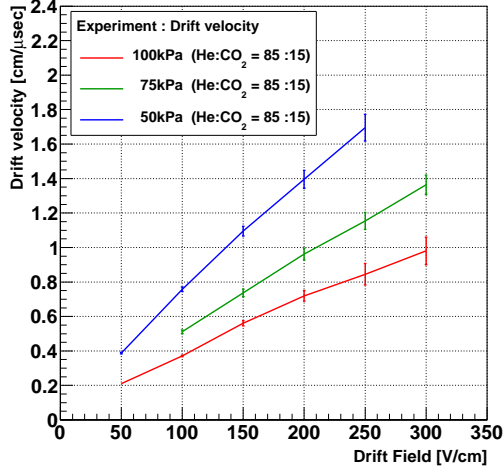
Figure 6.17: The measured drift velocity with different drift fields. The red, green and blue points show the gas pressure of 100, 75 and 50 kPa, respectively.
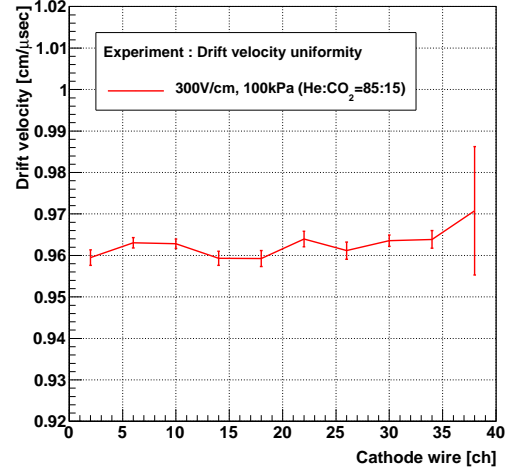
Figure 6.18: The position dependence of the drift velocity.

shows the energy distribution and Figure 6.20 shows the X distribution. These values are summarized in Table 6.8.

Assuming 220 kW of beam power at J-PARC and 7% of duty factor of the SFC as discussed in Section 5.2, the rate of the neutron decay is expected to be 0.089 cps. Thus the signal-to-background ratio is calculated as

$$S/N = \frac{8.9 \times 10^{-2}}{1.4 \times 7.0 \times 10^{-2}} \sim 1.1. \tag{6.3}$$

As described in Section 3.6, the Pb shielding stop 98% of environmental γ ray from the measurement of the NaI detector and the surrounding cosmic-ray veto counters trigger 96% of the cosmic ray from the measurement of the cubic scintillator. For further reduction of the background, an improvement of the Pb shielding and the cosmic-ray veto counter is needed.

	Total count[cps]	Energy cut[cps]	Fiducial cut[cps]
Environmental BG	123.7	100.1	30.7
+ Pb shield	58.4	44.2	13.9
+ Cosmic-ray veto	7.7	4.3	1.4

Table 6.8: The measured event rate inside MLF, with a shield, and with cosmic-ray veto (successive application).
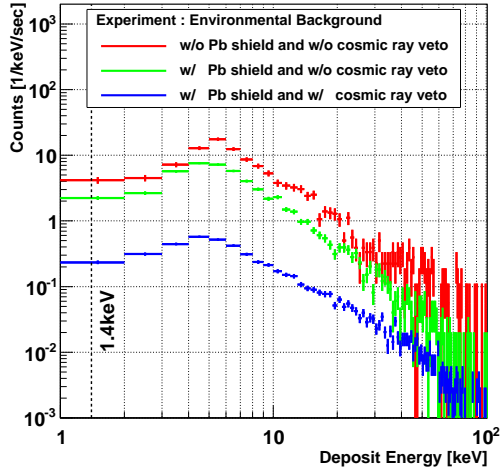
Figure 6.19: Energy spectrums of environmental background. A red, green and blue lines represent the spectrum with no shielding, only with Pb shielding and with Pb shield and cosmic ray veto.
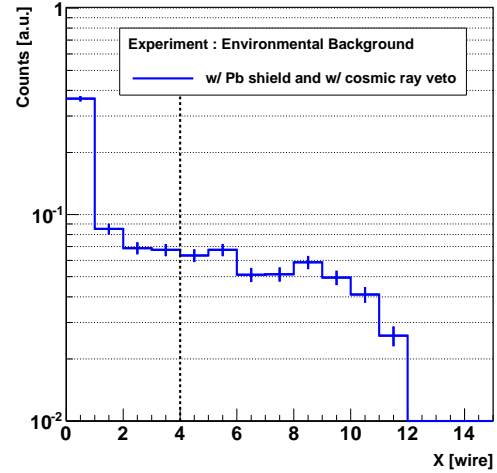
Figure 6.20: X distribution of the environmental background with Pb shielding and cosmic ray veto.

6.4 Performance for the particle detection

In order to achieve more than 99.9% detection efficiency for the neutron decay and the neutron capture in ^{3}He, the following items have to be satisfied:

- Detection for more than 99.9% of the neutron decay and the neutron capture in ^{3}He,

- Separation between the neutron decay and the neutron capture in ^{3}He,

- Separation between the neutron decay and the neutron capture in CO_2.

In this section, these items are investigated.

6.4.1 Setup for the measurement

The performance of the TPC is evaluated by using 5.9-keV X rays from ^{55}Fe, cosmic rays and neutrons as shown in Table 6.9 and Figure 6.21. For the measurement of the detection efficiency of the anode wires by use of the cosmic rays, the TPC is rotated 90 degrees. The MWPC part of the TPC consists of two PEEK frame and a gap between the plates is 6 mm. 5.9-keV X rays from ^{55}Fe at position A in Figure 6.21 pass through the gap and converts into an electron inside the wire cell. Thus it is possible to directly measure the gain of MWPC. The drift part has two slits at

positions B and C, and another ^{55}Fe on the rotating table enables to evaluate the recombination at the time of ionization and the transportation efficiency during the drift. The cosmic rays are triggered by two scintillators arranged one above the other (X and Y) and detection efficiencies of the anode wires are obtained. The neutrons pass through an entrance of the TPC and make it possible to evaluate the ^{3}He reaction.

A	^{55}Fe	Gain
B, C	^{55}Fe	Recombination and transportation efficiency
D	Cosmic ray	Detection efficiency
E	Neutron	^{3}He reaction

Table 6.9: Evaluated components, positions (Figure 6.21), and kind of sources to measure the detector performances.
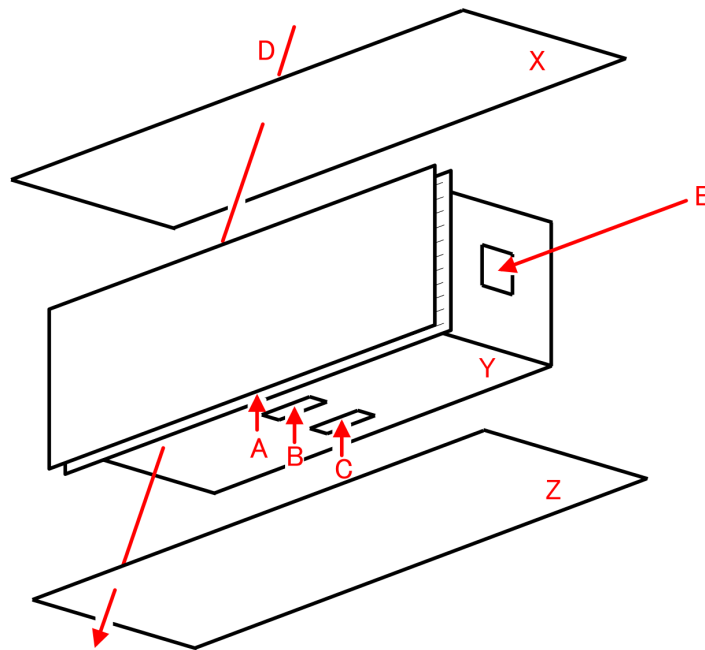
Figure 6.21: A schematic drawing of the positions of the sources for the evaluations of performances of the TPC.

6.4.2   Detection for the neutron decay

The pressure and voltage dependences of the gain of MWPC are shown in Figure 6.22. Although the gain at the discharge voltage decreases with decreasing pressure, the gain of 50000 can be performed under 50 kPa ∼ 100 kPa. Detection
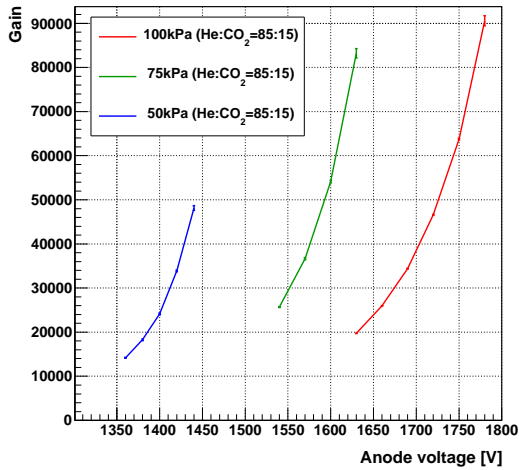
Figure 6.22: The measured gains with different anode voltages. The red, green and blue points show the gas pressure of 100, 75 and 50 kPa, respectively.
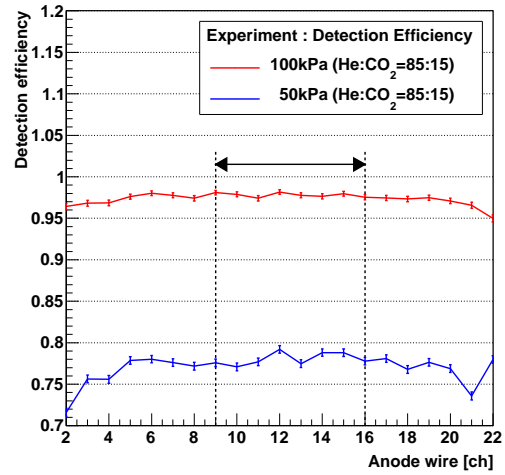
Figure 6.23: The detection efficiencies for each anode wire, measured with 1720 V for anode wires and 300 V/cm or the drift part.

efficiencies of the anode wires are evaluated by cosmic rays entering at an angle of less than 5° with respect to the cathodes. Figure 6.23 shows the detection efficiencies under 50 kPa and 100 kPa with the gain of 50000, which reflects the energy loss in the gas. Applying this detection efficiency to `Geant4` simulation, more than 99.9% detection efficiency is achieved even under 50 kPa as shown in Figure 5.14.

6.4.3 Separation between the neutron decay and the neutron capture in ^{3}He

As discussed in Section 4.4, the saturation effect becomes apparent in the case of the neutron capture in ^{3}He, since the energy loss of the reaction products, a proton and a triton, is sufficient to induce the space-charge effect. Figure 6.24 shows the saturation effect for the neutron capture in ^{3}He. It is found that an output decreases with increasing pressure and gain. Thus the energy spectrum of the electrons from the neutron decay overlaps that of the neutron capture in ^{3}He as shown in Figure 5.6. According to a `Geant4` simulation as shown in Figure 5.7, these two reactions are separated if the maximum energy deposit among the wires of the neutron capture in ^{3}He is more than 35 keV. Figure 6.25 shows the maximum energy deposit of the ^{3}He reaction candidates, which includes the on-axis and off-axis reaction (S_n, B_n^{gas}) as discussed in Section 5.3.2. It is found that 99.9% of the ^{3}He reaction candidates deposits more than 35 keV as the maximum
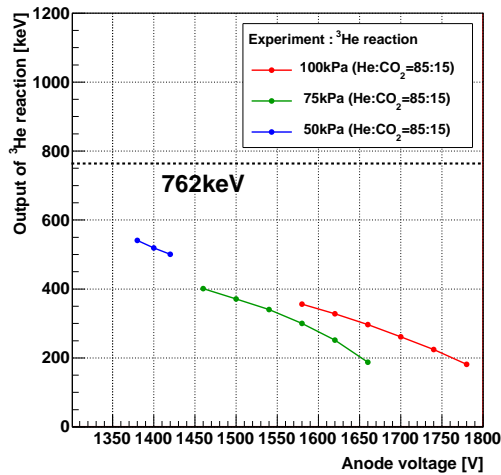
Figure 6.24: The measured pulse height with different anode voltage and gas pressures.
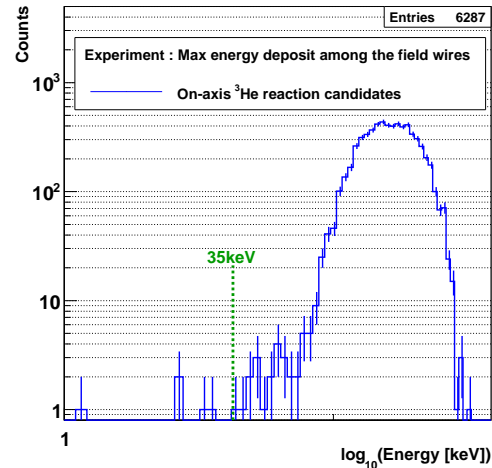
Figure 6.25: The spectrum of the maximum energy deposit among the field wires.

energy among the wires.

The separation is also confirmed by using ^{3}He-enriched measurement, since each spectrum can be independently extracted as discussed in Section 5.6. If the pressure decreases, the effect of saturation and the energy loss of the electron decreases, so that the separation remains even at reduced pressure.

6.4.4   Separation between the neutron decay and the neutron capture in CO_2

More than 99.9% of the neutron decay has to be separated from the recoiled nucleus due to the neutron capture in CO_2 as discussed in Section 5.4.2. However the separation is deteriorated by the recombination at the time of ionization, the attenuation efficiency during the drift and the position dependence of the gain as shown in Table 5.7.

Recombination effects and transportation efficiency can be evaluated by use of ^{55}Fe at positions A, B and C, which decrease with an increase of the electric field in the drift part as shown in Figure 6.26 and Figure 6.27. Under 300 V/cm, the measured values are 12% and 2%, respectively.

In this experiment, the gases do not flow during the experiment, so that H_2O contained in outgassing is emitted from the TPC itself, which causes electron attachment during the drift. Figure 6.28 shows the spectrum of a quadrupole mass spectrometer under 3.6×10^{-4} Pa after evacuation for two weeks. Figure
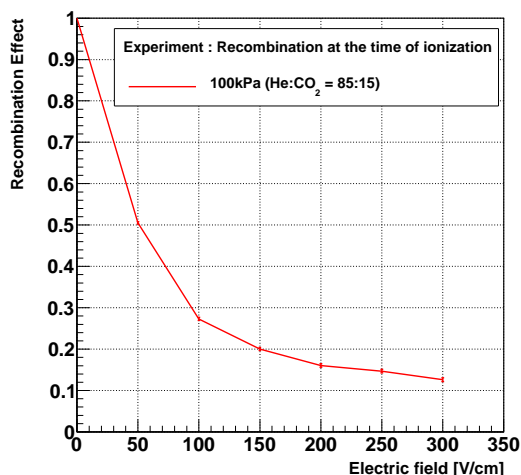
Figure 6.26: The recombination efficiency with drift filed.
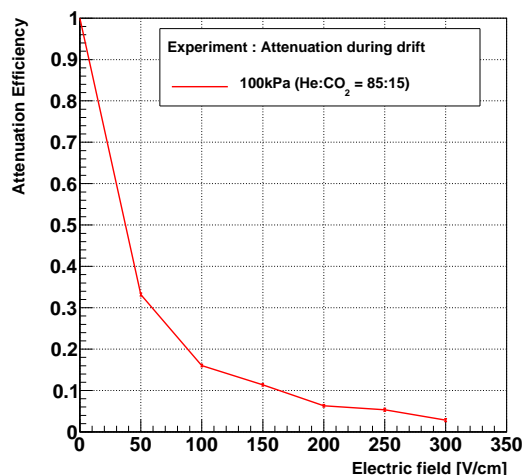
Figure 6.27: The transportation efficiency with drift filed.

6.29 shows the time variation of the attenuation effect. For the requirement, the attenuation efficiency less than 4%, a continuous operation for 4 days is possible.
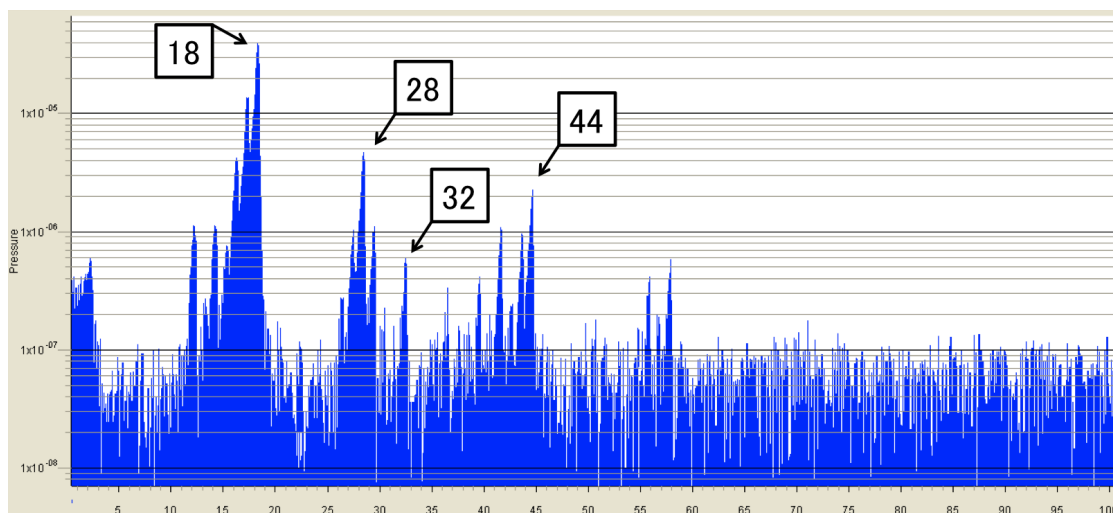
Figure 6.28: A spectrum of the quadrupole mass spectrometer in the vacuum chamber under 3.6×10^{-4}Pa.

Figure 6.30 shows a spectrum of the 5.9-keV X ray from [55]Fe after the correction of the time variation of the attenuation efficiency; the energy resolution is obtained as 9.9%. Eliminating contributions of the initial ionization, the recombination and the attenuation, the non-uniformity of the gain can be calculated as 5.1%, which also satisfies the requirement. Table 6.10 summarizes all the items.

In this condition, the ratios of the electrons with an energy of less than 1.4
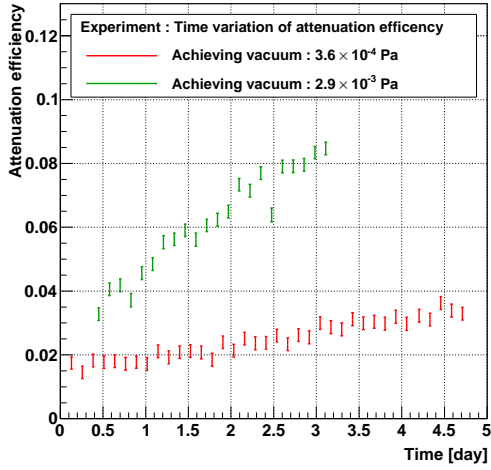
Figure 6.29: The time variation of the attenuation efficiency of the TPC with different achieving pressures.
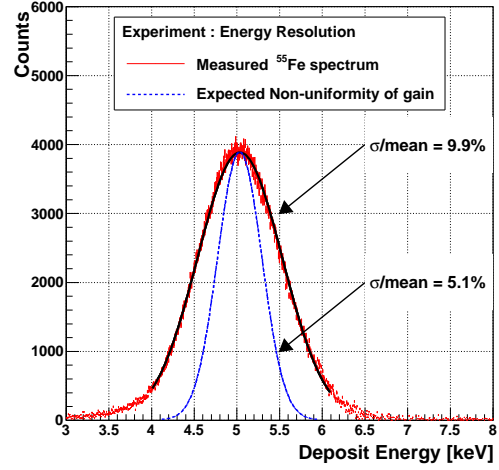
Figure 6.30: Energy resolution for the 5.9-keV X ray from ^{55}Fe (red) and an expected non-uniformity of the gain.

	requirement	measurement
Recombination at the time of ionization	13%	12%
Attenuation efficiency during the drift of 150mm	4%	4%
Non-uniformity of the gain	9%	5%

Table 6.10: Comparison between the requirement and the measurement for the items which determine the separation between the neutron decay and the neutron capture in CO_2.

keV under 50 kPa and 100 kPa are 0.06% and 0.03%, respectively. According to $S'_\beta = 2N'_{50kPa} - N'_{100kPa}$ as discussed in Section 5.8, an uncertainty arising from correction of the detection efficiency for the neutron decay becomes 0.1%.

Chapter 7

Discussion

An innovative TPC with no radioactive contamination and high detection efficiency has been developed. In this chapter, the expected sensitivity by use of the developed TPC is described.

7.1 Uncertainty arising from the particle detection

As discussed in Section 6.4, the developed TPC has a capability to detect more than 99.9% of the neutron decay and the neuron capture in ^{3}He, which are fully separated by the calorimetric approach. In addition, the various backgrounds are properly subtracted by the data-driven approach as described in Chapter 5. As a result, the systematic uncertainty arising from the particle detection is reduced to 0.1%. In addition, the statistical uncertainty can reach 0.8% in 150 days with a beam power of 220 kW.

For the further improvement, intense neutron beams are desired as shown in Figure 5.23. The conceivable approaches are as follows.

- Beam power of J-PARC
  In spite of the designed beam power, 1 MW, the current beam power is limited under 300 kW, since the mercury target in MLF is damaged by the impact of the proton pulse. The study to soften the impact is in progress, so that it would be possible to increase the beam power in the near future.

- Beam loss in the Polarization beam branch
  The intensity of the Polarization beam branch is about a third of that of simulation. The reason is not known exactly, however there is the potential for an increase in the neutron flux.

- Beam loss at the SFC
  In spite of the cross section of the Polarization beam branch, 100 mm $\times$ 40 mm, only 20 mm $\times$ 20 mm of the neutrons can be reflected due to the size of the magnetic supper mirror. Thus sizable magnetic supper mirrors are now developed.

If the neutron intensity becomes equivalent to that with a beam power of 1 MW, the statistical uncertainty can reach 0.2% in 150 days.

7.2 Additional uncertainty

Additional systematic uncertainty are shown in Table 7.1, which are the determination of the counting rate of the neutron capture in ^{3}He as follows.

- Partial pressure of ^{3}He
  By use of the mass spectrometer, the ratio of ^{3}He and ^{4}He can be obtained by comparing it with a standard gas whose mixture ratio is pre-determined at 0.5%. An air gauge currently in use has a 0.01% accuracy guarantee, so that an accurate standard gas can be produced.

- Cross section of the neutron capture in ^{3}He
  In the preceding measurement of the cross section, the monochromatic neutron by use of Bragg reflection in crystal is employed; however the result was limited by the accuracy of the wavelength of the neutron [54]. BL08 in MLF is designed to have the world best resolution of the wavelength, 0.03%, thus it is possible to improve the cross section by using BL08.

- Non-uniformity of the temperature of the gas
  According to $P = \rho R T(x)$, the temperature of the gas has influence on the density of ^{3}He, whose non-uniformity is measured to be 0.1%. In particular, the pre-amplifier on the MWPC part becomes a source of heat. Thus a micro-power pre-amplifier has been developed with a group of liquid xenon TPC mainly in KEK, which is expected to reduce the non-uniformity of the temperature.

- N_2 contamination
  N_2 causes the ^{14}N(n, p)^{14}C reaction as discussed in Section 5.3.2, which becomes the background to the ^{3}He(n, p)^{3}H. By using a gas chromatography, the nitrogen pressure of 0.6 Pa is measured 5 days after filling the gas. Assuming ^{3}He partial pressure of 0.1 Pa, the ^{14}N(n, p)^{14}C reaction arises an

uncertainty of 0.5%. Therefore sources of N_2 contamination, such as outgassing or air leak, have to be identified and removed.

Item	uncertainty
Determination of the partial pressure of ^{3}He	0.5%
Cross section of the neutron capture in ^{3}He	0.13%
Non-uniformity of the temperature of the gas	0.1%
N_2 outgassing	0.5%

Table 7.1: Additional uncertainty except for the particle detection.

7.3 Achievable sensitivity

In Table 7.2, an achievable sensitivity is summarized. Owing to the development of the TPC, the experiment is limited by uncertainties except for the particle detection. As a result, for the 150 days the experiment in this thesis will reach 1.0% and 0.8% under 220 kW and 1 MW of the beam power, respectively.

	This work	
Facility	J-PARC	
Repetition rate	40 Hz	
Pulse per repetition	6	
Length of pulse	400 mm	
Velocity	500 m/s $\sim$ 1200 m/s	
Duty factor	$\sim 7\%$	
Beam cross-section	20 mm $\times$ 20 mm	
Divergence	± 4.2 mrad	
TPC gas	He : CO_2 = 85 : 15	
Pressure	50 kPa $\sim$ 100 kPa	
Size of TPC	300 mm $\times$ 300 mm $\times$ 960 mm	
Beam Power	220 kW	1 MW
Neutron decay (S_β)	0.1cps	0.5 cps
Neutron capture rate in ^{3}He (S_n)	1$\sim$3 cps	1$\sim$3 cps
Environmental background(B_e)	8 cps	8 cps
Beam-induced background (B_b)	2 cps	20 cps
ϵ_β	$> 99.9\%$	$> 99.9\%$
ϵ_n	$> 99.9\%$	$> 99.9\%$
Beam time	150 days	150 days
Statistical uncertainty	0.8%	0.2%
Correction for ϵ_β	0.1%	0.1%
Correction for ϵ_n	$< 0.1\%$	$< 0.1\%$
Subtraction of B_e	$< 0.1\%$	$< 0.1\%$
Subtraction of B_b	$< 0.1\%$	$< 0.1\%$
Determination of partial pressure of ^{3}He	0.5%	0.5%
Cross section of the neutron capture in ^{3}He	0.13%	0.13%
Non-uniformity of temperature of gas	0.1%	0.1%
N_2 outgassing	0.5%	0.5%
Total uncertainty	1.0%	0.8%

Table 7.2: Expected accuracy of the experiment in this thesis. Parameters of the neutron bunch after the chopper, characteristics of the TPC, and systematic uncertainties are summarized.

Chapter 8

Conclusions

The neutron lifetime is of growing importance in Big Bang nucleosynthesis (BBN) after the observation of the baryon density of the universe by WMAP, since the detailed verification for the BBN may provide insight into new physics beyond the minimal BBN model. In that context a new experiment for the neutron lifetime is proposed in this thesis and employs the world's most intensive pulsed neutron source, J-PARC. This will be the first experiment for the neutron lifetime by means of the accelerator.

A key principle of the experiment due to Kossakowski *et al.* is the coincident measurement of the neutron decay and the neutron capture in ^{3}He in a time projection chamber. For the coincident measurement, the neutrons have to be shaped into a bunch whose length is shorter than the TPC. By analyzing the event while the whole the bunch is inside the TPC, 4π acceptance for each event is guaranteed.

The preceding study by Kossakowski background to was limited by the performance of the TPC which has a large amount of the background to the neutron decay. Thus an innovative time projection chamber has been developed, which is made from PEEK without radioactive contamination, installed ^{6}Li plate for the scattered neutron inside the TPC and surrounded by 4π shielding for the environmental radiation. Consequently, the background to the neutron decay can be reduced to 1/10 compared with the TPC developed by Kossakowski *et al.*

Meanwhile an analysis algorithm for the reduction of the systematic uncertainty has been developed. Due to the calorimetric approach, more than 99.9% detection efficiency for the neutron decay and neutron capture in ^{3}He is performed. Moreover the remained backgrounds can be subtracted properly by the data-driven approach.

As a result, all the systematic uncertainties arising from the particle detection are reduced to 0.1%. And then, for the 150 days the experiment in this thesis will

reach 1.0% and 0.8% under 220 kW and 1 MW of the beam power respectively. The dominant systematic uncertainty is due to the uncertainty of the ^{3}He density. If the precise measurement of the ^{3}He density and the high intensity of the neutron beam are realized, it is possible to achieve 0.1% accuracy in the neutron lifetime measurement.

Acknowledgments

Bibliography

[1] J. Chadwick. Possible existence of a neutron. Nature, 129(830):312, 1932.

[2] J. Chadwick. The existence of a neutron. Proceedings of the Royal Society of London. Series A, 136(830):692–708, 1932.

[3] R. A. Alpher, H. Bethe, and G. Gamow. The origin of chemical elements. Phys. Rev., 73:803–804, Apr 1948.

[4] G. Gamow. Expanding universe and the origin of elements. Phys. Rev., 70:572–573, Oct 1946.

[5] K Nakamura et al. Review of particle physics. J. Phys., G37:075021, 2010.

[6] H. Snell and L. C. Miller. On the radioactive decay of the neutron. Physical Review, 74(9):1217, 1948.

[7] Fred E. Wietfeldt and Geoffrey L. Greene. *Colloquium* : The neutron lifetime. Rev. Mod. Phys., 83:1173–1192, Nov 2011.

[8] J. S. Nico, M. S. Dewey, D. M. Gilliam, F. E. Wietfeldt, X. Fei, W. M. Snow, G. L. Greene, J. Pauwels, R. Eykens, A. Lamberty, J. Van Gestel, and R. D. Scott. Measurement of the neutron lifetime by counting trapped protons in a cold neutron beam. Phys. Rev. C, 71:055502, May 2005.

[9] A. Serebrov, V. Varlamov, A. Kharitonov, A. Fomin, Yu. Pokotilovski, P. Geltenbort, J. Butterworth, I. Krasnoschekova, M. Lasakov, R. Tal'daev, A. Vassiljev, and O. Zherebtsov. Measurement of the neutron lifetime using a gravitational trap and a low-temperature fomblin coating. Physics Letters B, 605(1-2):72 – 78, 2005.

[10] V. Ezhov. Seventh International Workshop on Cold and Ultracold Neutrons, St. Petersburg Russia, 2009.

[11] R. Kossakowski, P. Grivot, P. Liaud, K. Schreckenbach, and G. Azuelos. Neutron lifetime measurement with a helium-filled time projection chamber. Nuclear Physics A, 503(2):473 – 500, 1989.

[12] M Greiner. Gauge theory of weak interactions, 3rd edition , p272.

[13] E.L. and Wright. The WMAP data and results. New Astronomy Reviews, 47(11-12):877 – 881, 2003. Proceedings of the Workshop on The Cosmic Microwave Background Radiation and its Polarization.

[14] Richard H Cyburt, Brian D Fields, and Keith A Olive. An update on the big bang nucleosynthesis prediction for 7 li: the problem worsens. Journal of Cosmology and Astroparticle Physics, 2008(11):012, 2008.

[15] Y. I. Izotov and T. X. Thuan. The primordial abundance of 4He: evidence for non-standard big bang nucleosynthesis. Astrophys. J., 710:L67–L71, 2010.

[16] Robert A. Malaney and Grant J. Mathews. Probing the early universe: a review of primordial nucleosynthesis beyond the standard big bang. Physics Reports, 229(4):145 – 219, 1993.

[17] J. Chadwick and M. Goldhaber. A nuclear photo-effect: Disintegration of the diplon by -rays. Nature, 134:237–238, 1934.

[18] J. Chadwick and M. Goldhaber. The nuclear photoelectric effect. Proceedings of the Royal Society of London. Series A - Mathematical and Physical Sciences, 151(873):479–493, 1935.

[19] K. Nakamura et al. (Particle Data Group). Journal of Physics G37, 075021 (2010) and 2011 partial update for the 2012 edition.

[20] J. M. Robson. The radioactive decay of the neutron. Phys. Rev., 83(2):349–358, Jul 1951.

[21] N. D'Angelo. Cloud-chamber measurement of the half-life of the neutron. Phys. Rev., 114(1):285–292, Apr 1959.

[22] A.N. Sosnovsky, P.E. Spivak, Yu.A. Prokofiev, I.E. Kutikov, and Yu.P. Dobrinin. Measurement of the neutron life-time. Nuclear Physics, 10:395 – 404, 1959.

[23] C. J. Christensen, A. Nielsen, A. Bahnsen, W. K. Brown, and B. M. Rustad. Free-neutron beta-decay half-life. Phys. Rev. D, 5(7):1628–1640, Apr 1972.

[24] Yu.Yu. Kosvintsev, Yu.A. Kushnir, V.I. Morozov, and G.I. Terekhov. The use of ultracold neutrons for measurement of the neutron lifetime. JETP Letters, 31(4):236 – 240, 1980.

[25] Yu. Yu. Kosvintsev, V. I. Morozov, and G. I. Terekhov. Measurement of neutron lifetime through storage of ultracold neutrons. JETP Letters, 44(10):571 – 574, 1986.

[26] P. E. Spivak. Zh. Eksp. Teor. Fiz., 94(1), 2009.

[27] F. Anton, W. Paul, W. Mampe, L. Paul, and S. Paul. Measurement of the neutron lifetime by magnetic storage of free neutrons. Nucl.Instrum.Meth.A, 284(1):101 – 107, 1989.

[28] A.G. Kharitonov, V.V. Nesvizhevsky, A.P. Serebrov, R.R. Taldaev, V.E. Varlamov, A.V. Vasilyev, V.P. Alfimenkov, V.I. Lushchikov, V.N. Shvetsov, and A.V. Strelkov. Preliminary results of neutron lifetime measurements with gravitational ucn trap. Nucl.Instrum.Meth.A, 284(1):98 – 100, 1989.

[29] W. Mampe, P. Ageron, C. Bates, J. M. Pendlebury, and A. Steyerl. Neutron lifetime measured with stored ultracold neutrons. Phys. Rev. Lett., 63:593– 596, Aug 1989.

[30] R.R. Tal'daev et al. V.V. Nesvizhevskii, A.P. Serebrov. Zh. Eksp. Teor. Fiz., 102, 740, 1992.

[31] W.Mampe et al. JETP Lett. 57, 82., 1993.

[32] J. Byrne, P. G. Dawber, C. G. Habeck, S. J. Smidt, J. A. Spain, and A. P. Williams. A revised value for the neutron lifetime measured using a penning trap. EPL (Europhysics Letters), 33(3):187, 1996.

[33] S Arzumanov, L Bondarenko, S Chernyavsky, W Drexel, A Fomin, P Geltenbort, V Morozov, Yu Panin, J Pendlebury, and K Schreckenbach. Neutron life time value measured by storing ultracold neutrons with detection of inelastically scattered neutrons. Physics Letters B, 483(1-3):15 – 22, 2000.

[34] A. Pichlmaier, V. Varlamov, K. Schreckenbach, and P. Geltenbort. Neutron lifetime measurement with the UCN trap-in-trap MAMBO II. Phys.Lett., B693:221–226, 2010.

[35] Willis E. Lamb. Capture of neutrons by atoms in a crystal. Phys. Rev.,
55:190–197, Jan 1939.

[36] L. D. P. King and Louis Goldstein. The total cross section of the ^{3}He nucleus
for slow neutrons. Phys. Rev., 75:1366–1369, May 1949.

[37] C. D. Keith, Z. Chowdhuri, D. R. Rich, W. M. Snow, J. D. Bowman, S. L.
Penttilä, D. A. Smith, M. B. Leuschner, V. R. Pomeroy, G. L. Jones, and
E. I. Sharapov. Neutron cross sections for ^{3}He at epithermal energies. Phys.
Rev. C, 69:034005, Mar 2004.

[38] V. I. Lushchikov, Yu. N. Pokotilovskii, A. V. Strelkov, and F. L. Shapiro.
Observation of ultracold neutrons. JETP Letters, 9(1):23 – 26, 1969.

[39] Neutron News, 3:29–37, 1992.

[40] A. Bussiére, P. Grivot, R. Kossakowski, P. Liaud, P. de Saintignon, and
K. Schreckenbach. A monochromatized chopped beam of cold neutrons for
low background experiments. Nucl.Instrum.Meth.A, 332(1-2):220 – 223, 1993.

[41] P. Grivot, R. Kossakowski, P. Liaud, K. Schreckenbach, G. Azuelos,
A. Bussiere, and P. de Saintignon. A helium-filled time projection cham-
ber for a neutron lifetime measurement. Nucl.Instrum.Meth.A, 34(1):127 –
134, 1988.

[42] K. Taketani *et al.* A high S/N ratio spin flip chopper system for a pulsed
neutron source. Nucl.Instrum.Meth.A, 634(1, Supplement):S134 – S137, 2011.
Proceedings of the International Workshop on Neutron Optics NOP2010.

[43] The web site of J-PARC. "http://j-parc.jp/".

[44] F. Mezei. Commun. Phys., pages 81–85, 1976.

[45] E. Fermi and L. Marshall. Interference phenomena of slow neutrons. Phys.
Rev., 71:666–677, May 1947.

[46] Edward Melkonian. Slow neutron velocity spectrometer studies of O_2, N_2, A,
H_2, H_2o and seven hydrocarbons. Phys. Rev., 76:1750–1759, Dec 1949.

[47] E. Melkonian, L. J. Rainwater, W. W. Havens, and J. R. Dunning. Slow
neutron spectrometer studies of oxygen, nitrogen, and argon. Phys. Rev.,
73:1399–1400, Jun 1948.

[48] N. Z. Alcock and D. G. Hurst. Neutron diffraction by gases. Phys. Rev., 75:1609–1610, May 1949.

[49] A. Lechner, M.G. Pia, and M. Sudhakar. Validation of Geant4 low energy electromagnetic processes against precision measurements of electron energy deposition. Nuclear Science, IEEE Transactions on, 56(2):398 –416, april 2009.

[50] E. Waibel and B. Grosswendt. Degradation of low-energy electrons in carbon dioxide: energy loss and ionization. Nucl.Instrum.Meth.A, 53(3):239 – 250, 1991.

[51] B. Grosswendt and W.Y. Baek. The energy dependence of W values for protons of energies up to 10 Mev. Radiation Protection Dosimetry, 61(1-3):267–274, 1995.

[52] H. Oide. wire chamber を用いた電離損失 energy 測定における空間電荷効果の取り扱いについて. The Autumn Meeting of the Physical Society of Japan, 2011.

[53] G.A. and Erskine. Electrostatic problems in multiwire proportional chambers. Nucl.Instrum.Meth.A, 105(3):565 – 572, 1972.

[54] J. Als-Nielsen and O. Dietrich. Slow neutron cross sections for He^3, B, and Au. Phys. Rev., 133:B925–B929, Feb 1964.